1968-09

Further low speed wind tunnel tests on slender cambered wings with apex blowing.

Cole, Joseph D.

Cranfield, England: College of Aeronautics

The College of Aeronautics
Cranfield

THESIS

Thesis

by

Lt. Joseph D. Cole USN

under the supervision of

Mr. J. J. Spillman, D.C.Ae.,A.M.I.Mech.E.,A.F.R.Ae.S.

of the

Department of Aerodynamics

FURTHER LOW SPEED WIND TUNNEL TESTS ON SLENDER CAMBERED WINGS WITH APEX BLOWING

Academic Year 1967/68

20 September 1968

FURTHER LOW SPEED WIND TUNNEL TESTS ON SLENDER CAMBERED WINGS WITH APEX BLOWING

ABSTRACT

A family of five slender cambered wings with apex blowing has been compared by means of an experimental investigation carried out in the 8 ft. x 6 ft. low speed wind tunnel at the College of Aeronautics, Cranfield. The flow field was investigated with different blowing momentum coefficients, C_μ, at a Reynolds number, $R_c = 2.8 \times 10^6$, by the use of: Kiel tube traverses, measuring the total head variation at various chordwise stations; photography with a water vapor screen technique; and surface flow pattern visualization. The lift, drag, and pitching moment were measured at $C_\mu = 0$, 0.04, 0.08, and 0.12 on the various models through an incidence range from -10° to $+20^\circ$, at a Reynolds number, $R_c = 3.2 \times 10^6$.

It was found that the apex blowing air formed discrete jets which followed curved paths across the leading edges, over the shoulders, and then along the central portion of the model to the trailing edge. With apex blowing the leading edge vortices did not start to develop until aft of the positions where the blowing jets crossed the leading edges. The development of the leading edge vortices was inhibited when the shoulders of the model were close to the leading edges.

Apex blowing increased the aerodynamic lift at incidences above 4°. The greatest increment in lift due to blowing was obtained on the MGW model. The lift-dependent drag was decreased on all wings by an increased blowing coefficient. At $C_\mu = 0.12$ the maximum lift-drag ratio on all wings was higher than at $C_\mu = 0$, although at lower values of C_μ the maximum was less than in the unblown case. Apex blowing generally had a stabilizing effect and the useable range of C_L's was increased.

It was shown that apex blowing, applied to an all-wing airbus, can reduce the required landing distance by about 28%.

To Linda, Jenni, and Joey.

PREFACE

This thesis describes research work carried out in the 8 ft. x 6 ft. low-speed wind tunnel of the Aerodynamics Department, The College of Aeronautics, Cranfield, during the academic year 1967/68. The wind tunnel program was sponsored by the Ministry of Technology.

The author is indebted to his supervisor, Mr. J. J. Spillman, for his advice and criticism during the year, and to Mr. D. Kirby, of R.A.E. Farnborough, for his useful comments and suggestions. The author also wishes to express special thanks to: Mr. S. H. Lilley and Mr. D. Sibley for their practical assistance with the wind tunnel testing; Mr. D. Bruce and Mr. T. Atkins for constructing the model and extensions; Mr. B. Hunt and his photographic staff for their help in producing the flow visualization results; the library staff for their assistance; and his wife, Linda, for typing the thesis.

Joseph D. Cole

CONTENTS

LIST OF FIGURES

FURTHER LOW SPEED WIND TUNNEL TESTS ON SLENDER CAMBERED WINGS WITH APEX BLOWING

1. INTRODUCTION

The use of slender shapes for aircraft which operate at supersonic speeds has long been recognized as the solution to the compressibility problems encountered in this flight regime. The complexity of the natural separated flow which occurs on such wings has been exceedingly difficult to solve theoretically, however. Early theories for low aspect ratio wings, such as that due to R. T. Jones (Ref. 1), were based on attached flow solutions and were hardly adequate to describe the separated vortex flow. Legendre (Ref. 2) was the first to set forth a theory which stipulated leading edge separation and conical vortex flow over slender wings. Maskell and Weber (Ref. 3) were among the first to propose that aerodynamic shapes should be designed to control and to take advantage of the natural vortex flow instead of to suppress it.

It has been found that slender shapes, suitable for supersonic flight, have disadvantages at subsonic speeds. Among these are the reduced lift-curve slope, the increased lift-dependent drag, and the reduction of longitudinal stability.

Lee (Ref. 4) has shown that the lift-dependent drag can be reduced on slender wings with separated flow by as much as 30% by designing the thickness and camber such that forward facing surfaces lie behind the leading-edge vortices. Maskell and Kuchemann (Ref. 5) suggested, from theoretical considerations, that high energy air could be ejected from the swept leading edges of a slender wing to artificially strengthen the leading-edge vortices and thus increase the lift and the lift-drag ratio of the wing. Using this method in conjunction with Lee's forward facing surfaces, the lift-dependent drag could be further reduced.

Trebble (Ref. 6) and Alexander (Ref. 7) investigated edge blowing along the entire leading edge of slender delta wings. Trebble confirmed that a substantial gain in lift at a given incidence could be obtained by edge

blowing, especially in the region of the approach. Trebble also noted a large drag penalty with edge blowing because his experimental model was designed to blow the high energy jet sheet normal to the swept leading edge, thereby introducing a reverse-thrust component. Alexander tested various angles of blowing from the leading edge. He was able to eliminate the large drag penalty, experienced by Trebble, by directing the blowing nozzles aft, without appreciably affecting the gain in lift due to edge blowing. Alexander also noted a reduction in the lift-dependent drag with edge blowing due to the forward facing surfaces of his rhombic cross-section model being acted upon by the strengthened leading edge vortices. The effect of edge blowing was found by Alexander to be most pronounced near the apex of the model at incidence.

During the past decade, a great deal of interest has been shown in the subject of a short range subsonic airbus capable of carrying a large number of passengers at comparitively low cost. A possible solution to this design problem has been shown to be an all-wing layout. This would entail the application of the slender-wing concept in an entirely new flight regime. Kuchemann and Weber (Ref. 8) have pointed out that the all-wing design: (1) is more compact than the conventional layout; (2) allows a larger payload weight to total aircraft weight ratio because of a more efficient structure; and (3) could increase productivity over a relatively short range because a high cruise Mach No., $M = 0.8$, would be practical. Gates (Ref. 9) indicates that the all-wing airbus concept provides the most efficient "wrap" for passengers since the passenger compartment also acts as the lifting surface. The Avro Vulcan has shown that there is no excessive stability problem inherent in an all-wing design.

The addition of edge blowing to the all-wing concept could prove to be an important factor in deciding the airbus question. With the blowing air being supplied by the propulsion plant, the solution would be a complete integration of all the aircraft systems -- propulsion, structure, payload, and aerodynamics. This solution is complex but this is not necessarily a disadvantage since no single parameter would play a dominating role and many desirable properties could be included without incurring any excessive penalties.

Following the work in edge blowing and the recent interest in the all-wing airbus concept, Hyde (Ref. 10) began investigation into the feasibility of edge blowing only near the apex of a delta wing. His model also incorporated thickness and camber distributions similar to those envisaged for an all-wing airbus. Hyde obtained results similar to those previously reported for the case of blowing along the entire leading edge. In addition, he noted that apex blowing eliminated the problem of vortex

breakdown which occured on the aft portion of the model at high incidences without blowing. The highly sloped shoulders, very near the leading edges of the airbus model, appeared to inhibit the natural growth of the leading edge vortices, both with and without apex blowing.

This thesis concerns wind tunnel tests set up to investigate the flow field of the airbus model, used by Hyde, in order to gain an understanding of the nature of the flow over such a shape with apex blowing. A further investigation, prompted by the apparent inhibiting of the leading edge vortex development on the original model, is concerned with tests on four variations in the planform shape of the all-wing airbus model with apex blowing. The first of the planform variations considered has straight leading edges, the second and third have parabolic-gothic leading edges, and the fourth has quartic-gothic leading edges.

2. LIST OF SYMBOLS

α Geometric wing incidence measured relative to the flat base plate of the model.

α_o Geometric wing incidence at zero lift coefficient.

μ Momentum of the jet, or coefficient of viscosity.

ρ Fluid mass density.

σ_x Standard deviation of the independent variable, x.

σ_y Standard deviation of the dependent variable, y.

ϕ Mean thrust angle, the angle between the mean jet-thrust line at the blowing nozzle and the model centerline.

A An empirical constant.

AR Aspect ratio of the model, $=b^2/S_m$.

b Span of the model.

B An empirical constant.

BW The basic wing model.

c_o Centerline chord of the model.

c_o' Virtual centerline chord of model with flat plate extension.

C_μ Blowing momentum coefficient, see Appendix A.

C_D Drag coefficient, $=D/q_o S_m$.

$C_{D_{min}}$ Minimum value of drag coefficient.

C_H Total-head coefficient, $=(H - p_o)/q_o$.

C_L Lift coefficient, $=L/q_o S_m$.

$C_{L_{md}}$ Value of lift coefficient at minimum drag.

C_M Pitching moment coefficient, $=M/q_o S_m c_o$.

$C_{x'}$ Resultant force coefficient in x'-direction, $F_{x'}/q_o S_m$.

D Drag.

DDW The double-delta wing model.

H Total head measured in the flow field.

K Lift-dependent drag factor, $= \frac{(C_D - C_{D_{min}})\pi AR}{(C_L - C_{L_{md}})^2}$.

L Lift.

LGW The large gothic wing model.

M Pitching moment, or Mach number.

MGW The medium gothic wing model.

m_j Rate of mass flow in the jet.

N Number of sample measurements considered.

p Local static pressure.

p_a Atmospheric pressure.

p_p Planform parameter, $= S_m/bc_o$.

q Dynamic pressure.

r Pearson-r linear correlation coefficient.

R_c Reynolds number based on centerline chord of the model.

s Semi-span of the model at the trailing edge.

$S_{Y \cdot X}$ Standard error of an estimate of Y based on X.

S Projected area of the BW model.

S_m Projected area of model with flat plate extension.

SGW The small gothic wing model.

$t_{.975}$ Student's t-distribution ratio at 95% level for (N - 2) degrees of freedom.

T Thrust.

V_j Jet velocity at nozzle exit assuming isentropic expansion to freestream static pressure.

V Local velocity.

x,y,z Body axes.

x',y',z' Wind axes.

Subscripts:

A Indicates coefficient based upon aerodynamic forces only, e.g. C_{L_A}.

j Indicates conditions in the jet.

o Indicates freestream conditions.

R Indicates coefficient based upon resultant forces, including component of jet thrust, e.g. C_{L_R}.

T Indicates coefficient based upon force due to component of jet thrust, e.g. C_{L_T}.

x',y',z' Indicates direction corresponding to wind axes.

3. DESCRIPTION OF APPARATUS

3.1 Details of Models:

The basic wing (BW) model is shown mounted in the wind tunnel in Fig. 3•1. The details of the entire family of wings tested are shown in Fig. 3•2. A summary of the significant dimensions of all the models is given in Table I.

The BW model was the model with "type B" nozzles which was tested by Hyde (Ref. 10). This model was built to simulate a short range all-wing airbus incorporating apex blowing. The other wings in the family were made by means of flat plate extensions attached to the BW model to investigate alternative planforms, leading edge shapes, thickness distributions near the leading edges, and aspect ratios for such an airbus.

The BW shape was the result of empirical development of the integrated all-wing layout concept. The thickness and camber distributions were fabricated from mahogany which was then combined with a flat aluminum base plate with a beveled edge. The upper (lower in Fig. 3•1) surface profile formed parabolic sections in planes radiating from the apex. Each chordwise station was of constant thickness over the central 60% of the local span, as illustrated for two such sections in Fig. 3•2. The profile of each chordwise section, outboard of this central region, followed a cubic curve to the sharp leading edge formed by the beveled edges of the base plate. The maximum thickness-chord ratio occured at 50% centerline chord and equalled 8.02%.

The apex portion of the BW model, forward of 30% centerline chord, contained the blowing system plenum chamber. The blowing air entered the model through the hollow support strut and was ducted, inside the model, forward to the plenum chamber through a two-inch diameter flexible hose. The blowing air was ejected from the plenum chamber through two constant exit area cascades of turning vanes. The longitudinal centerlines of these cascades were alligned with the sharp leading edge of the model as shown in Fig. 3•3. The mean thrust line of these nozzles was at an angle, $\Phi=38^{\circ}$, with the model centerline (see Fig. 3•2).

The flat plate extensions which, combined with the BW model, formed the other models tested were fabricated from 0.125-inch sheet steel. This sheet steel was bent to conform to the shape of the bevel of the BW base

plate. A flat base was obtained on the "extension" models by filling the area outboard of the bend with wood as illustrated in Fig. 3•2. The edges of the extension plates were beveled to form sharp leading edges similar to those on the BW base plate.

The extensions were designed to intersect the BW leading edges at 30% centerline chord. The straight edged extension formed the double-delta wing (DDW). The small gothic wing (SGW) and medium gothic wing (MGW) were formed by parabolic-gothic extensions. The large gothic wing (LGW) was formed by a quartic-gothic extension. The BW trailing edge span was increased by 20% in the DDW, MGW, and LGW models. The SGW model had the same trailing edge span as the BW model.

3•2 Tunnel and Blowing System:

Tests were conducted in the 8 ft. x 6 ft. rectangular, closed working section, low-speed wind tunnel at the College of Aeronautics, Cranfield. The models were mounted in an inverted position and supported on the Warden type six-component balance system by a hollow support strut.

The high pressure blowing air was supplied from the settling chamber of a compressor to the system depicted in Fig. 3•4. Interference with the balance system was kept to a minimum by introducing the blowing air to the balance support system through flexible rubber hoses. An orifice plate in the main feed line was used to measure the mass flow rate of the blowing air. The static pressure in the system was measured in the manifold unit at the top of the support strut. The pressure drop across the orifice plate and the static pressure, and hence the mass flow, could be controlled by either a hand operated mechanical valve or a remote control Hale Hamilton L15 valve mounted in parallel. The best control of the flow was obtained by the combined use of both valves.

3.3 Flow Visualization Equipment:

A Lede smoke generator was used during preliminary investigation into the nature of the flow field. The smoke was generated by heating parafin. The resulting smoke was ejected by compressed CO_2 through a flexible rubber tube which could be conveniently placed in the vicinity of the model as desired.

The flow field, infused with smoke, was viewed at various chordwise stations by shining a plane of light across the working section. The plane of light was produced by an air-cooled mercury vapor lamp mounted in a focusing apparatus which formed a narrow slit of light. The mercury vapor lamp was fitted with an over-ride switch

which allowed increased brightness for a period of up to ten seconds. This over-ride function was utilized to obtain photographs using the water vapor screen technique described in Section 4.2.

A Kiel tube probe similar to that described by Kirkpatrick and Field (Ref. 11) was used to investigate the total head variations through the flow field at various chordwise stations. The Kiel tube used had an outside diameter of 0.063 in. and was 4 in. long. It was insensitive to pitch and yaw angles up to 20° and gave accurate indications of total head within 2-3% at angles of pitch and yaw up to 30°. The Kiel tube was mounted on a traverse gear on which the probe position could be monitored and controlled from outside the tunnel. Full movement of the probe in the y-z plane as well as in pitch and yaw was available. Unfortunately, the Kiel tube tip did not coincide with the pitch and yaw pivot point of the traverse gear. Therefore, the position of the Kiel tube tip was not known without making a direct measurement when any changes in the pitch or yaw were made during a traverse run.

The traverse gear was limited to a maximum tunnel speed of 100 ft./sec. because of the design of the structural components.

4. DESCRIPTION OF PROCEDURES

4.1 Measurement of Blowing Momentum Coefficient, C_μ:

From dimensional analysis (see Appendix A), an additional parameter is required when considering the aerodynamics of a wing with apex blowing. This parameter is called the blowing momentum coefficient, C_μ, and is defined as:

$$C_\mu = \frac{m_j v_j}{q_\infty S} = \frac{T_j}{q_\infty S}$$

It should be noted, the C_μ was based on the BW area, S, for the tests on all wings.

The most direct means of experimentally measuring and controlling the values of C_μ was found to be via the pressure drop across the orifice plate which was a function of the mass flow rate of the blowing air. This was done by first measuring the wind-off thrust, $T_{x'}$, on the model at zero incidence and various values of orifice plate pressure drop. Then, knowing the mean thrust angle at the nozzles, $\Phi = 38^\circ$, the blowing momentum coefficient could be written:

$$C_\mu = \frac{T_{x'}}{q_\infty S \cos \Phi} = \frac{T_j}{q_\infty S}$$

for any tunnel speed. For operation during the tests, the C_μ values at a given tunnel speed were calibrated against the orifice plate pressure difference. Thus, by setting the appropriate orifice plate pressure difference, a given value of blowing momentum coefficient, C_μ, could be obtained for testing. Since the blowing system was not near the choked condition and the tunnel speed was low throughout the tests, this method was considered to be accurate.

4.2 Flow Visualization Techniques:

The flow visualization tests were conducted at large incidences (e.g. $\alpha = 15.6^\circ$) in order to obtain a well developed flow field of reasonable size. In this way, the relative size of disturbances introduced by the measuring and visualization apparatus was kept as small as possible.

Except for the smoke tests, all of the flow visualization tests were run at a tunnel speed, V_o=100 ft./sec., which corresponded to a Reynolds number, $R_c = 2.6 \times 10^6$.

The first attempt to visualize the flow field around the BW model was by the use of a smoke filament at very low tunnel speeds. The end of the tube from the smoke generator was placed at various positions around the model, particularly near the apex. The paths of the smoke filament were traced visually along the model and cross sections of the flow were viewed using the mercury vapor slit light. Attempts to photograph the flow field proved unsuccessful because the density of the smoke was insufficient even at extremely low tunnel speeds. This problem was further complicated by the requirement of a very small mass flow rate in the blowing system to obtain a given value of C_μ at the low tunnel speeds. The orifice plate pressure difference was virtually impossible to maintain constant at very low values.

As a solution to the problems related to the use of the smoke generator for visualizing the flow field, a system was devised for adapting a smoke technique described by Pankhurst and Holder (Ref. 12). It was found that water, introduced into the model plenum chamber under pressure, would be atomized by the blowing air and carried along as water vapor after it emerged from the nozzles. The intensity of the water vapor was sufficient to allow viewing of the flow field at any chordwise station using the mercury vapor slit light.

In order to photograph the flow field cross section illuminated by this technique, the entire wind tunnel area had to be darkened except for the mercury vapor lamp. The best photographs were obtained using an exposure time of 10 sec. at $f4.0$ while operating the over-ride switch on the mercury vapor lamp. Photographs were taken for all the models at $x/c_o = 0.50$, 0.70, and 0.90, $C_\mu = 0.08$ and 0.12, and $\alpha = 15.6^\circ$.

This technique could be used at a normal tunnel operating speed, V_o=100 ft./sec., and did not interfere with the natural flow field. It had the disadvantage that it could not be used for the unblown case, $C_\mu = 0$, since the atomization of the water depended upon the blowing air.

Kiel tube traverses to measure the total head variation across the entire flow field cross section were made on the BW model at $\alpha = 15.6^\circ$ and V_o=100 ft./sec. for the following cases:

C_μ=0:	$x/c_o = 0.50$, 0.70, 0.90
=0.04:	$x/c_o = 0.50$, 0.70, 0.90
=0.08:	$x/c_o = 0.30$, 0.35, 0.40, 0.45, 0.50, 0.70, 0.90
=0.12:	$x/c_o = 0.335$, 0.45, 0.50, 0.70, 0.90

It should be noted that each of these individual cases required approximately six to eight hours of running time to complete.

Prior to each run the traverse gear was positioned so that the tip of the Kiel tube was located at the desired chordwise station. The traverse gear was adjusted so that the probe tip would move in the y-z plane (body axes). The probe attitude was fixed parallel to the leading edge for the traverse of the region between the sharp leading edge and the shoulder of the model. The area outside this and over the central portion of the model was traversed with the probe parallel to the model base plate but at zero yaw angle. The Kiel tube was kept at a constant attitude through each section of the traverse because the change in the probe tip position could not be monitored remotely if either the pitch or yaw angle was altered as noted in Section 3.3. The position of the probe tip was measured before each run and after each section of the traverse was completed in order to check the remote position-monitoring system.

The total head measurements of the Kiel tube were recorded at a spacing of 0.125 in., near the center of the vortices and jets, and 0.25 in. elsewhere in the flow field. The readings were made with reference to atmospheric pressure on an inclined manometer filled with metholated spirits. These readings were corrected for a pressure difference of +0.2 in. H_2O between atmospheric pressure, p_a, and tunnel freestream static pressure, p_o, (i.e. $p_a - p_o = 0.2$ in. H_2O).

A graphical method described by Kirkpatrick and Field (Ref. 11) for locating the approximate center of a vortex was applied to the results of these traverses to locate the approximate center of the blowing air jet at each chordwise station. From these positions the path of the blowing air jet was traced over the model as described in Section 5.1.

Surface flow visualization was accomplished by painting the model with yellow "dayglo" paint prior to operating the wind tunnel at a given flow condition. Tests were made at $\alpha = 15.6^\circ$ and $C_\mu = 0$ and 0.08 on both the BW and MGW models. Photography of the resulting patterns, which were illuminated with ultra violet light, was only partially successful because of the difficulty in getting the proper combination of exposure time and illumination. Therefore, line drawings of the flow patterns were made as a substitute for the rather poor quality photographs.

4.3 Forces and Moments:

Lift, drag, and pitching moment measurements were made on the DDW, SGW, MGW, and LGW models. The tests were made at a tunnel speed, $V_o = 125$ ft./sec., corresponding

to a Reynolds number, $R_c = 3.2 \times 10^6$. Each wing was tested at values of blowing momentum coefficient, C_μ=0, 0.04, 0.08, and 0.12, through a range of incidence from -10° to $+20^\circ$. The incidence was measured with reference to the flat base plate of the model.

The force and moment coefficients were based upon the plan area of the model, S_m, and referred to the wind axes. The pitching moment coefficients were based on the centerline chord and referred to the mid-centerline chord position on all models.

The force and moment results quoted for the BW model were taken from the report on Hyde's work (Ref. 10).

4.4 Estimation of Accuracy:

The position-monitoring console of the traversing equipment on which the Kiel tube was mounted enabled the probe to be positioned within ±0.020 in. in both the y-direction and the z-direction. The probe was subject to some buffeting in the flow field, especially near the vortex and jet centers. The sensitivity of the probe to pitch and yaw angles greater than $\pm 20\text{-}30^\circ$ was not considered to affect adversely the measurements except in the regions directly adjacent to the shoulder of the model and at the extreme limits of the flow field near the free stream conditions. The vortex and blowing jet total head contour positions are therefore estimated to be within ±0.125 in. except near the freestream condition, C_H=1.0, where the accuracy can not be fairly estimated. When the trailing edge semi-span of the BW, s=18 in., is considered, the accuracy of these results can be seen to be quite acceptable. The total head coefficient can only be considered as an indication of the nature of the flow field in the absence of local static pressure measurements throughout the flow field.

The results of the smoke, water vapor screen, and surface flow visualization tests can not be considered quantitatively. The qualitative value of these results is good, however, and the flow field picturization resulting from them is factual.

The corrections applied to the force and moment data are outlined in Appendix B. The overall accuracy of the coefficients quoted is estimated to be:

C_L: ±0.0021

C_D: ±0.0018

C_M: ±0.0010

5. DISCUSSION OF RESULTS

5.1 Nature of the Flow Field:

The major portion of the flow visualization test program was conducted on the BW model. For obvious reasons then, the discussion of the flow field is primarily concerned with this model. Photographs indicate that the general nature of the flow regime is similar for all the wings tested. The specific results discussed, therefore, can be generalized to give a reasonable understanding of the nature of the flow field on each of the wings of the family.

Initial flow visualization tests were conducted using a smoke generator at low tunnel speeds. These tests gave an indication of the general nature of the flow field. The most significant fact revealed by these tests was that the flow with apex blowing was not as anticipated from the results of earlier work on edge blowing. The tests made by Trebble (Ref. 6) and Alexander (Ref. 7), with blowing along the entire leading edge, indicated that the air from the nozzles formed leading edge vortices of a greater strength than were present without blowing. The smoke tests with apex blowing show no leading edge vortices except near the wing tips. The blowing air on each side of the wing forms a large conical tube which initially moves away from the leading edge and then bends inwards toward the leading edge, crossing it at about 40% centerline chord. It subsequently follows a path across the shoulder of the model at about midchord and down the central portion of the model to the trailing edge. No such flow over the center of the model was present in tests without apex blowing.

In order to take pictures of the flow field, a method of employing the water vapor screen technique was devised as described in Section 4.2. Photographs were then obtained such as those shown in Fig. 5•1 for the BW at $\alpha = 15.6^{\circ}$ and $C_{\mu} = 0.08$ and Fig. 5•2 for the MGW at the same flow conditions.

The cross section of the flow field at mid-centerline chord is shown in Fig. 5•1a. The leading edge vortex can be seen as a small circular shape (dotted for clarity) just below the leading edge of the model as shown in the inverted position. The remainder of the bright vapor pattern is attributed to the apex blowing air. At this position it can be seen that the center of this air is located near the shoulder of the model.

The fainter vapor pattern, outboard of the leading

edge vortex and the blowing air, shows the path of the blowing air forward of midchord. This path is visible in all the pictures of Figs. 5•1 and 5•2, and is caused by the reflection of the light outside the cross-sectional plane under consideration. The large circular shape that appears in all the pictures in Figs. 5•1 and 5•2 is caused by entrained water droplets. It is felt that this is unique to the flow with water vapor and is caused by the coalescing of atomized water particles to form water droplets. These droplets have relatively large size and weight and therefore their position in the swirling flow is outside the actual flow regime of interest.

Figs. 5•1b and 5•1c depict the flow field on the BW at 70% and 90% centerline chord, respectively. The leading edge vortices are positioned below the leading edges. These pictures along with Fig. 5•1a show the progress of the blowing air over the model shoulder and then, in a more or less streamwise direction, along the central portion of the model toward the trailing edge.

For comparison the flow field of the MGW is shown in Fig. 5•2 at the same flow conditions as the BW in Fig. 5•1. It can be seen that the flow patterns are essentially the same for the two wings. The pictures of the MGW are representative of those for all the wings with extensions.

Although the flow is similar it should be noted that the leading edge vortex on the MGW is significantly larger than that on the BW at the corresponding chordwise stations. This indicates that the development of the leading edge vortex is impeded on the BW by the thickness distribution near the leading edge. Additionally, the size of the leading edge vortex appears to increase with the size of the extension on the wing. That is, increasing the distance of the leading edge from the thickness shape allows the vortex to grow larger. Squire (Ref. 13) obtained results which also indicate that the vortex development on the suction surface is inhibited by a body which lies near the leading edge of a delta wing.

Another difference in the flow fields which is worthy of note is that secondary separation and a secondary vortex is visible at all stations on the MGW in Fig. 5•2. This too has been dotted for clarity.

The results of a traverse of the flow field at various chordwise stations made by a Kiel tube give further indications of the character of the flow. Figs. 5•3a, 3b, 3c, 3d, and 3e depict the flow on the BW at $x/c_o = 0.30$, 0.40, 0.50, 0.70, and 0.90, respectively, at $\alpha = 15.6^\circ$ and $C_\mu = 0.08$. The contour lines in Figs. 5•3 trace positions of constant values of the total-head coefficient defined as:

$$C_H = \frac{H - p_o}{q_o}$$

The freestream condition is indicated by the total-head coefficient, $C_H = 1.0$.

Figs. 5•3 can be used to consider each station separately or, by viewing them jointly, a three dimensional trace of the flow field can be envisaged. The contours of constant C_H in Figs. 5•3 depict shapes very similar to those observed in the water vapor screen pictures of Figs. 5•1 at the corresponding stations. The peak negative values of C_H found in the leading edge vortex region, as in Fig. 5•3d, correspond to the high axial velocities at the vortex center as found by Earnshaw (Ref. 14) and Lambourne and Bryer (Ref. 15). The peak positive value of C_H found in the blowing air region correspond to a high velocity region with very little rotational component. The structure in the blowing air region closely resembles the structure of a jet as reported by Zijnen (Ref. 16). The apparent discrepancy in the two indications of high axial velocity can be explained by considering the static pressures at the respective positions. Refs. 14 and 15 indicate a large negative static pressure in the center of a vortex while Ref. 16 states that the static pressure everywhere in a jet, except very near the orifice, is essentially the same as the ambient pressure. While static pressure was not measured through the flow field, reference to the surface static pressure measurements, carried out by Hyde (Ref. 10) on the BW model, shows that there is a large nagative static pressure coefficient on the surface adjacent to the vortex, both with and without blowing. The surface pressure is only slightly more negative with blowing than without blowing in the central region affected by the blowing air jet.

The contours of $C_H = 1.0$ in Figs. 5•3 are dotted because the exact position of the freestream conditions was difficult to obtain due to the large variation of flow direction and the inaccuracy of the probe in a flow field at an angle of yaw greater than $\pm 20\text{-}30^\circ$. The contours toward the center of the vortex and jet structures are considered to be more accurate however, because of the success of Kirkpatrick and Field (Ref. 11) in finding the vortex center positions with a similar probe.

Fig. 5•3a shows the cross section of the flow field at 30% centerline chord, or 0.4 in. aft of the rearmost nozzle. There is evidence of a slight rolling of the jet sheet due to the pressure difference across it, but the most obvious effect of the low pressure on the upper surface of the jet sheet is the expansion of the jet sheet into a jet of nearly circular cross section. Fig. 5•3b shows the blowing jet to be just outboard of the leading edge at 40% chord ($\alpha = 15.6^\circ$, and $C_\mu = 0.08$). The circular shape is distorted by the forces of the air stream and the shape of the model. The midchord section depicted in

Fig. 5•3c shows the center of the jet near the crest of the model shoulder. The outer regions of the jet are spread across the central region of the model. Some of the jet air is entrained by the vortex which is just beginning to develop along the leading edge. At 70% chord, shown in Fig. 5•3d, the jet is positioned inboard of the shoulder and the leading edge vortex is quite well developed. Any connection between the two structures at this station is not distinct because the flow direction over the shoulder is outside the insensitive range of the Kiel tube, thus making accurate measurements impossible with the allignment of the tube used in the traverse. Fig. 5•3e shows only the jet structure at 90% chord. The vortex was not investigated at this position but its structure is expected to be similar to that at 70% chord only larger and with a higher negative total-head coefficient at the center. The decrease in the peak value of C_H at the center of the jet, along the chord, is caused by viscous mixing. The order of the decay is somewhat greater than that stated by Zijnen (Ref. 16) for plane jets in still air because of the freestream velocity and the curvature of the blown jet path.

The approximate path of the center of the blowing air jet over the BW at $\alpha = 15.6°$ and $C_\mu = 0.08$ is plotted in Fig. 5•4 in plan view and side elevation from the results of the Kiel tube traverse. A similar series of traverses was made at the same incidence but at $C_\mu = 0.12$. These results are also shown in Fig. 5•4 for comparison. It can be seen that the center of the jet at the higher value of blowing coefficient lies farther outboard and higher above the model. This is caused by the larger momentum of the jet at the higher blowing coefficient. The shape of the jet path is attributed to the thickness of the model and the resulting high suction on the shoulder at the midchord position as shown in Ref. 10. The emerging jet is attracted toward this suction region, crossing the leading edge at approximately 40% centerline chord, and then continues across the shoulder onto the central region of the model to the trailing edge. The side elevation shows that the jet travels virtually in the freestream direction until, near the trailing edge of the model, the aerodynamic forces bend it to the horizontal.

Fig. 5•5 shows the leading edge vortex structure on the BW at 70% chord, $\alpha = 15.6°$ and $C_\mu = 0$. This can be compared with the vortex at the same chordwise station shown in Fig. 5•3d at $C_\mu = 0.08$. The minimum value of C_H recorded without blowing was -3.25 while with blowing it was -2.50. This indicates that the axial velocities are of the same order. Considering that the vortex in the blown case did not commence its development until approximately the midchord position of the model, the development of the vortex with blowing appears to occur at a faster rate than without blowing.

Surface flow patterns on the BW and MGW at $\alpha=15.6^{\circ}$ are shown in Figs. 5•6 and 5•7, respectively. The flow patterns on both wings are shown with $C_{\mu}=0$ and $C_{\mu}=0.08$.

As can be seen in Fig. 5•6a for $C_{\mu}=0$, $\alpha=15.6^{\circ}$, the leading edge vortex lies in the region between the leading edge and the shoulder on the BW. The primary attachment line is on the near vertical surface of the model until, at about 80% chord, the local surface slope decreases sufficiently to allow the attachment line to move inward away from the leading edge. The surface flow above the attachment line flows over the shoulder. The local curvature of the surface induces a suction peak followed by a marked bubble of separation which occurs along the shoulder of the model. As would be expected, there appears to be a weak vortex along this shoulder separation bubble. Inboard of the shoulder the flow is virtually streamwise. A secondary separation line is visible along the leading edge aft of 70% chord which corresponds to the region of the wing where the cross-sectional shape is not hindering the lateral spread of the vortex field.

Fig. 5•6b shows the surface flow pattern on the BW for $\alpha=15.6^{\circ}$, $C_{\mu}=0.08$. What appears to be a vortex attachment line very high on the vertical surface forward of 30% chord is actually a line dividing the flow entrained, due to viscous mixing, by the blowing air emerging from the nozzles and the flow proceeding over the shoulder of the model. A normal vortex is not formed in this region since the leading edge is masked by the blown air jet. The path of the blown air jet is evident by a highly scrubbed area over the shoulder crest near midchord where the jet is close to the surface. The flow pattern over the central area of the model indicates that the jet has some swirl velocity attributable to the slight rolling of the jet sheet noted as it emerged from the nozzles. The leading edge vortex attachment line is visible on the vertical surface aft of the jet path. The secondary separation line is similar to that of the unblown case. The size of the shoulder separation bubble was greatly reduced with blowing.

The surface flow patterns on the MGW are shown in Figs. 5•7a and 5•7b for the unblown and blown case, respectively. The flow patterns again show a great similarity to the corresponding case on the BW. The main differences are: (1) the separation bubble in the unblown case is farther inboard, relative to the shoulder, on the MGW and (2) a secondary separation line commences immediately aft of the leading edge "kink" on the MGW and runs the entire length on the wing extension both with and without blowing. With blowing the jet crosses the leading edge extension in the vicinity of the "kink". This allows the natural leading edge vortex to begin its development sooner since the leading edge is not masked by the jet.

It appears from the vapor screen pictures that more of the blowing air enters the vortex system on the MGW. This is the result of the positioning of the blowing jet in relation to the leading edge vortex on this wing.

It should be noted that the relatively large areas along the trailing edge of the model which appear to be areas of separation in the surface flow pictures (especially in the unblown cases) are considered to be products of the experimental technique. These are attributed to a combination of the viscosity of the "dayglo" paint and the gravitational force along the surface of the inverted model (i.e. the paint encumbered in flowing "uphill" on the aft portion of the model). The flow near the centerline at the trailing edge was also disturbed by the wake from the supporting strut. These regions were therefore disregarded in the consideration of the flow field.

From all the flow visualization test results, an overall picture of the flow field was formulated for both the BW and MGW. These pictures are presented in Figs. 5•8 and 5•9, respectively.

The fundamental difference between the flow field discussed here and those previously discussed in the field of leading edge blowing is the existence of the high total head jet. In order to investigate the phenomenon further, a short series of Kiel tube traverses was made on the symmetrical model with rhombic cross section, described by Alexander (Ref. 7), with and without apex blowing. The blown air emerged from the leading edge in a direction normal to it (i.e. at an angle of 70° to the upstream direction). These tests show that there is no high total head jet region in the flow field on such a model with apex blowing. The center of the vortex structure also indicated higher negative values of total head coefficient with blowing. These results imply that the entire blown air sheet enters and strengthens the leading edge vortex on this model. The indications of the tests on Alexander's model lead to the possibility that the flow field discussed here for the present family of wings is unique. This is most probably due to the severe thickness distribution of the model. Another possibility for the difference, however, is the rearward direction of the blown air emerging from the nozzles of the present models since the jet sheet emerged perpendicular to the leading edge in the tests on Alexander's model. With the blown air directed aft, there is less tendency for the jet sheet to roll up and enter the leading edge vortex. Instead it tends to remain a discrete jet and to follow the separate path previously described.

5.2 Balance Measurements:

5.2.1 Lift:

The aerodynamic lift, C_{L_A}, is defined as the total lift measured, C_{L_R}, minus the component of lift due to the jet thrust, C_{L_T}. The aerodynamic lift at various values of C_μ is plotted versus incidence, α, in Figs. 5•10a, 10b, 10c, and 10d for the DDW, SGW, MGW, and LGW, respectively. It can be seen in Figs. 5•10 that the aerodynamic lift is increased by apex blowing at incidences above 4°, approximately, on all the wings. It is decreased at negative incidences when the vortices and blowing jets lie below the wing. The improvement in aerodynamic lift with an increased blowing coefficient indicates a true rise in lift rather than a lift increment due to an increased thrust component.

The shape of the C_{L_A}-α curves at incidences near zero degrees is very irregular. This is caused by the peculiar vortex formation and jet sheet interaction at low incidences as discussed by Alexander (Ref. 7) and Hyde (Ref. 10). A detailed investigation of this region was not included in this test program.

The effect of vortex breakdown, a sudden decrease in the lift curve slope with no blowing at high incidence, α=16°-18° approximately, can be seen in Figs. 5•10a, 10b, and 10c for the DDW, SGW, and MGW, respectively. There is only a slight decrease in the slope of the lift curve of the LGW in Fig. 5•10d at the highest incidence tested, indicating that vortex breakdown on this model occurs at a higher incidence. As an example of the varying incidences where vortex breakdown occurs on different wings, Ref. 17 states that an uncambered delta wing with 70°-sweep normally experiences vortex breakdown at about 30° incidence. Vortex breakdown is completely eliminated on the DDW with $C_\mu = 0.04$ as it was on the BW (Ref. 10). The gothic wings (SGW and MGW) are not affected as severely by vortex breakdown at $C_\mu = 0$ as the DDW, but require higher values of C_μ to completely eliminate the effects of it.

Refs. 18 and 19 state that vortex breakdown is caused by an adverse pressure gradient along the vortex path which, in turn, causes a free stagnation point to exist along the vortex center filament. Vortex breakdown occurs immediately downstream of this free stagnation point. It appears from the vortex breakdown evidence that a gothic wing generally does not have an adverse chordwise pressure gradient as strong as that on a straight-edged wing at the same incidence. This is probably due to the "quasi-streamwise" tips of the gothic wings. Apex blowing reduces the pressure gradient in the vicinity of the leading edge vortices on the BW as indicated by the

surface pressure surveys by Hyde (Ref. 20). Its effect appears to be the same on the DDW but not as strong on the gothic wings.

The highest values of C_{L_A} at a given incidence and blowing coefficient are obtained on the MGW model, e.g. at $\alpha = 10^\circ$, values of C_{L_A} are:

	BW	DDW	SGW	MGW	LGW
$C_\mu = 0$:	0.470	0.520	0.490	0.520	0.510
$C_\mu = 0.04$:	0.495	0.565	0.535	0.585	0.565
$C_\mu = 0.08$:	0.505	0.580	0.550	0.610	0.585
$C_\mu = 0.12$:	0.520	0.590	0.555	0.615	0.605

The increment in aerodynamic lift due to apex blowing at constant incidence is illustrated at $\alpha = 5^\circ$, 10°, and 15° in Fig. 5•11 for each model. It can be seen that the increments in lift are approximately the same on all wings at $\alpha = 5^\circ$. The additional lift due to apex blowing at constant C_μ increases for a given wing with a rise in incidence. Increasing the incidence causes a higher shoulder suction, thus the blowing jet travels farther onto the central portion and covers a larger area of the model. Surface pressure plots by Hyde (Ref. 20) indicate that the suction in this center area of the model is increased with apex blowing. It follows that the greater the area affected by the jet, the greater the increment in lift due to blowing. These surface pressure plots also indicate that on the BW with blowing the suction is increased near the apex blowing nozzles and reduced slightly near the leading edge vortex aft of the jet path. The effect of the combined suction changes on the model due to blowing is an increase in lift at each chord-station and therefore in the overall lift. At higher incidences the MGW and the LGW show the greatest increments in lift due to blowing. This is caused by the fact that the vortices on these models are larger and stronger in the blown case and therefore supplement the lifting effect of the blowing jet on the central portion of the models. These wings also have a larger flat-plate area on which the suction created by the vortices can act.

The general shape of the curves in Fig. 5•11 shows a relatively steep rise in lift increment with initial blowing coefficient followed by a more gradual increase. The initial rise is due to the complete change in the fundamental flow field caused by the blowing jet. The more gradual rise, as the blowing coefficient is increased, is due to the less radical changes in the flow field.

The lift-incidence relations of the family of wings

are generally linear above $\alpha = 4^\circ$ as opposed to the non-linear lift curves normally associated with slender wings. The lift-curve slopes in the linear region improve with increased blowing coefficient. The lift-curve slopes (per degree) were found to be:

	BW	DDW	SGW	MGW	LGW
$C_\mu = 0$:	0.0381	0.0445	0.0435	0.0445	0.0455
$C_\mu = 0.12$:	0.0416	0.0475	0.0490	0.0550	0.0540

These values can be compared with theoretical values of: 0.02/deg. due to R. T. Jones (Ref. 1) for potential flow, and 0.05/deg., at $\alpha = 10^\circ$, due to Brown and Michael (Ref. 22) for separated flow.

The values of incidence at zero lift, α_o, for the various wings at varying blowing coefficients were found to be:

	BW	DDW	SGW	MGW	LGW
$C_\mu = 0$:	-4.15°	-3.75°	-3.50°	-2.75°	-2.50°
$C_\mu = 0.04$:	-3.50°	-3.30°	-3.00°	-2.50°	-2.00°
$C_\mu = 0.08$:	-3.10°	-2.85°	-2.60°	-2.25°	-1.75°
$C_\mu = 0.12$:	-2.50°	-2.40°	-2.25°	-2.00°	-1.50°

It can be seen that the negative angle of incidence at zero lift, α_o, decreases on each wing with increased blowing coefficient. As anticipated, the value of α_o, at a given blowing coefficient, also becomes less negative with an increase in the flat plate area of the model. The variation in α_o as blowing is increased is generally smaller on the models with large flat plate areas.

In order to correlate the aerodynamic lift coefficients of the various wings in the family, the square root of the slenderness ratio, $\sqrt{s/c_o'}$, was applied as suggested by Peckham (Ref. 23). The value of the virtual centerline chord, c_o', was used to form the slenderness ratio for the wings with extensions (see Fig. 3•2). This correction caused the values of the lift coefficients for the different wings at a given blowing coefficient to collapse onto curves but, as expected, there was a separate curve for each value of C_μ. The relationship between these curves and the values of the blowing coefficient was investigated as described in Appendix C. The result of this analysis is the empirical relationship between the values of aerodynamic lift with apex blowing and without apex blowing for all the wings tested. This

relationship was derived as:

$$\left[\frac{C_{L_A}}{\sqrt{s/c_o'}}\right]_{C_\mu=0} = \left[\frac{C_{L_A}}{\sqrt{s/c_o'}}\right]_{C_\mu} \left(1 - 0.84 C_\mu^{0.621}\right)$$

The application of this empirical relationship to the test results made possible the collapse of the lift data, for all the wings, versus $(\alpha-\alpha_o)$ onto a single curve as shown in Fig. 5.12.

By means of the statistical analysis in Appendix C it was determined that the relationship between the corrected values of aerodynamic lift and $(\alpha-\alpha_o)$ is linear in the range:

$$2^\circ < (\alpha-\alpha_o) < 20^\circ$$

This linearity is depicted in Fig. 5•12 by the "least-square" line. The 95% confidence limits are also shown in Fig. 5•12 as discussed in Appendix C. The scatter for this series of results is quite normal since 96.5% of the data points lie within the 95% confidence region. The greatest amount of scatter occurs at the extremes of the $(\alpha-\alpha_o)$ range. This is caused at the low end by the irregular behavior of the flow at small incidences and at the high end by the approach of vortex breakdown.

Peckham's flat plate results (Ref. 23) are plotted in Fig. 5•12 for comparison. The fact that all of the present results lie well below the Peckham curve is due to the thickness of the present wings. The results of Peckham's tests on a thick wing with a rhombic cross section, which are presented by Earnshaw and Lawford (Ref. 24), agree very well with the present results.

It must be pointed out that there is no known theoretical basis for the collapse of the lift data shown in Fig. 5•12. It is not intended that the empirical relationship derived from the analysis in Appendix C be regarded as universal for all apex blowing shapes. In fact, it is highly probable that it is unique to the present family of wings due to their extreme thickness distribution and the associated flow field, described in Section 5.1.

The landing performance of an all-wing airbus configured with apex blowing is considered in Appendix D. As an extreme example, the total efflux from apex mounted engines was assumed to be exhausted through the blowing nozzles. The approach speed is reduced by 32 knots for this configuration with apex blowing which causes a corresponding reduction in landing distance of 28%. These reductions were the result of the "no stall" characteristic of the aircraft due to the elimination of vortex

breakdown with apex blowing. The landing distances calculated are only approximate since they were based on a rather simple analysis of the complex problem but they do serve to suggest the relative benefits that can be achieved with apex blowing.

As a result of calculations involving the same all-wing airbus, there does not appear to be a similar improvement in the take-off performance with apex blowing. This is primarily attributed to the reduction in axial thrust and the resulting decrease in acceleration for the configuration considered. The use of other aerodynamic lift augmentation devices such as directed thrust or leading edge and/or trailing edge flaps could possibly be used to improve the take-off performance of such an aircraft.

5.2.2 Drag:

The aerodynamic drag with apex blowing can not be measured directly on the balance system because of the component of thrust in the x′-direction. The value actually measured by the balance system is the force component in the x′-direction, $F_{X'}$. The aerodynamic drag is found from the relationship:

$$C_{D_A} = -C_{X'} + C_\mu \frac{S}{S_m} \cos\phi \cos\alpha$$

where $C_\mu \frac{S}{S_m} \cos\phi \cos\alpha$ is the coefficient of thrust in the x′-direction related to the particular model area.

The aerodynamic drag, C_{D_A}, is plotted against the aerodynamic lift, C_{L_A}, in Figs. 5•13a, 13b, 13c, and 13d for the DDW, SGW, MGW, and LGW, respectively. In all cases the drag at a given lift coefficient above $C_{L_A} \simeq 0.3$ was reduced with increased blowing coefficient. Below this value of C_{L_A}, in the region of minimum drag, the aerodynamic drag increased slightly with greater blowing coefficient. A large increase in drag can be seen in Figs. 5•13a, 13b, and 13c at the onset of vortex breakdown in the unblown case on the DDW, SGW, and MGW. The LGW results again point out that vortex breakdown does not occur on that model over the incidence range tested. The drag rise due to vortex breakdown is markedly reduced by the application of apex blowing, signifying that vortex breakdown has been eliminated (DDW) or reduced (SGW and MGW).

With $C_\mu = 0$, the minimum drag coefficient for all the wings tested is essentially the same as that of the BW, i.e. $C_{D_{min}} = 0.016$ as opposed to 0.015 for the BW. The minimum drag occurs at $C_{L_A} = 0.05$, approximately, on all the wings and increases slightly with apex blowing.

With $C_\mu = 0$, values of C_{D_A}, at constant C_{L_A}, grow as the model leading edges get farther away from the forward facing surfaces. As apex blowing is increased, the lift-dependent drag is diminished in all cases. There is a greater reduction in drag due to blowing as the leading edge distance from the forward facing surfaces increases for the DDW, SGW, and MGW. This suggests that the leading-edge vortices on the MGW are stronger than those on the DDW and SGW since their capacity to reduce the lift-dependent drag is greater even though their distances from the forward facing surfaces are larger. There is a slight regression in this trend on the LGW. For example, at $C_{L_A} = 0.7$ the reduction in drag coefficient between $C_\mu = 0$ and $C_\mu = 0.12$ on the MGW is 0.033 while on the SGW and DDW, for the same conditions, the reductions

are 0.027 and 0.015, respectively. The corresponding reduction on the LGW is 0.028.

The drag results are presented as lift-drag ratios in Figs. 5•14a, 14b, 14c, and 14d for the DDW, SGW, MGW, and LGW, respectively. It can be seen that the maximum value of the lift-drag ratio for all of the wings with $C_\mu = 0$ is approximately 8.5 at $C_{L_A} \simeq 0.2$. All wings show a lessening in the maximum lift-drag ratio with low values of blowing coefficient due to the higher $C_{D_{min}}$ values with apex blowing. However, at a blowing coefficient, $C_\mu = 0.12$, this initial trend is reversed and all wings have a higher value of L/D_{max} than at $C_\mu = 0$. The DDW, SGW, and MGW attain a maximum lift-drag ratio of approximately 9.4 at $C_{L_A} \simeq 0.3$ with $C_\mu = 0.12$. The LGW reached $L/D_{max} = 10.0$ at $C_{L_A} \simeq 0.3$ with $C_\mu = 0.12$. The slight shift in the position and ultimate gain in the maximum lift-drag ratio with apex blowing occurs because of the greater effectiveness of apex blowing at incidences above $\alpha \simeq 4^\circ$ in both reducing drag and increasing lift. The lift-drag ratio is augmented above $C_{L_A} \simeq 0.4$ on all wings with a higher blowing coefficient. This result follows from the variation of the lift and drag curves with increased blowing coefficient.

Trebble (Ref. 6) and Alexander (Ref. 7) found that the maximum lift-drag ratio decreased with increased blowing coefficient in their experiments with blowing along the entire leading edge. In fact, Alexander stated that as a result of his tests "it does not seem feasible to use this device [edge blowing] to improve lift-to-drag ratios for the cruise case". On the other hand, Hyde (Ref. 10) reported a gain in the maximum lift-drag ratio with all values of apex blowing coefficient on the BW. By considering the data points plotted in Hyde's Fig. 31, it appears that curves very similar to those presented in Figs. 5•14 can be plotted to more accurately describe the behavior of the lift-drag ratio -- thus, giving results for the BW similar to those of the present tests.

Figs. 5•15a, 15b, 15c, and 15d show the lift-dependent drag factor, K, plotted against aerodynamic lift coefficient, C_{L_A}, for the DDW, SGW, MGW, and LGW, respectively. The lift-dependent drag factor is defined as:

$$K = \frac{(C_D - C_{D_{min}})\,\pi AR}{(C_L - C_{L_{md}})^2}$$

It can be seen in Figs. 5•15 that on all wings, K at $C_\mu = 0.12$ is much smaller at low values of C_{L_A} than for the other values of C_μ. This partially explains why the maximum lift-drag ratio increases for the case of $C_\mu = 0.12$.

At higher values of C_{L_A}, K is relatively constant, although it mounts slightly as C_{L_A} is boosted. The lift-

dependent drag factor normally varies with C_L on slender wings as a consequence of the non-linear lift. In all cases, the value of K at constant lift coefficient grew less with higher blowing coefficient. Vortex breakdown on the DDW, SGW, and MGW with $C_\mu = 0$ is symbolized in Figs. 5•15a, 15b, and 15c, respectively, by the sharp rise in the lift-dependent drag factor, K. Some evidence of the vortex breakdown is still apparent on the MGW at blowing coefficients, $C_\mu = 0.04$ and 0.08.

The values of K at $C_\mu = 0$ are all less than values calculated from the empirical relationship due to Kirby for flat-plate delta wings, denoted by (see Ref. 8):

$$K = \sqrt{2\,AR}$$

This result is as expected since the large forward facing surfaces present on the models reduce the lift-dependent drag. At $C_\mu = 0.12$ the values of K agree quite well with the theoretical values calculated by J. H. B. Smith for flat plates at $C_L = 0.5$ in conical flow. These values can be roughly represented by (see Ref. 8):

$$K = \left[\frac{5}{4}\,AR\right]^{1/3}$$

The variation of K with aspect ratio for the family of wings tested is shown in Fig. 5•16 for the case of $C_\mu = 0.08$. Similar pictures can be drawn for other values of blowing coefficient showing the same variation. Values of K were also determined by measuring the slopes of C_{D_A} versus $C_{L_A}^2$ curves. These values for the case of $C_\mu = 0.08$ are plotted in Fig. 5•16 and, as can be seen, they agree reasonably well with the near constant values calculated from the definition of K.

The lift-dependent drag factor could be further reduced by designing a wing shape with suitable camber, thickness, warp, and leading edge droop to be used in conjunction with apex blowing.

The family of wings tested can be compared to indicate the relative benefits of each in the configuration of an all-wing airbus similar to that described in Appendix D. Considering the force coefficient in the x′-direction, $C_{X'}$, the condition for longitudinal equilibrium is $C_{X'} = 0$. Ignoring the additional drag which will occur on any operational aircraft due to surface roughness, intakes, controls, etc., the $C_{X'}$ carpets are plotted in Figs. 5•17a, 17b, 17c, and 17d for the DDW, SGW, MGW, and LGW, respectively. In these curves it is shown that C_μ must be greater than 0.027 - 0.030 before longitudinal equilibrium can be achieved. This is of the same order as the minimum value of C_μ required for longi-

tudinal equilibrium for a similar layout with the BW (Ref. 10). The value of C_μ required to maintain longitudinal equilibrium at $C_{L_R} = 0.5$ varies from 0.091 for the BW to 0.126 for the LGW. This increase in C_μ required, and hence the blowing thrust, for the different planforms is associated with the enlarged areas of the models and not a simple function of their shapes. It is therefore not considered a realistic indication of the relative merits of the different planform shapes.

Fig. 5·18 shows the resultant-lift to gross thrust ratio curves for the various planforms at the longitudinal equilibrium condition, $C_{X'} = 0$. These curves are derived from the $C_{X'}$ carpets of Figs. 5·17 but are corrected to compensate for the differences in the model areas and depict more clearly the relative merits of the various planform shapes. The BW is shown to be superior in the cruise region, reaching a maximum lift-thrust ratio of 6.85 at $C_{L_R} \simeq 0.2$, while the trends imply that the MGW is superior in the approach region.

5.2.3 Pitching Moment:

The pitching moment measured on the balance system was corrected to compensate for the small moment caused by the blowing thrust to give the aerodynamic pitching moment. The aerodynamic pitching moment coefficient is based on the centerline chord, c_o, and the model area, S_m. The aerodynamic pitching moment coefficients, referred to the mid-centerline chord position of the model, are plotted against the aerodynamic lift coefficients at different C_μ values in Figs. 5·19a, 19b. 19c, and 19d for the DDW, SGW, MGW, and LGW, respectively.

Figs. 5·19 indicate that the general effect of apex blowing is a stabilizing one. The greatest improvement in the stability is gained by the initial application of blowing, i.e. $C_\mu = 0.04$. This is most evident in the range of $C_{L_A} = 0.3$ to 0.7. The useable range of C_{L_A} is extended with apex blowing because of the elimination (DDW), or reduction (SGW and MGW), of the nose-up pitch caused by vortex breakdown. The extension in the range of useable lift coefficients is one of the main advantages of apex blowing.

The instability that occurs, especially in the gothic wings, at low values of C_{L_A} corresponds to the low incidence range, noted previously, where the flow is irregular. Kirby (Ref. 25) said that similar instabilities were noted in tests at R.A.E. Farnborough and were attributed to separation of the flow in the aft-central portion of the model at low incidences. This was corrected by adding surface roughness to the model in order to force boundary layer transition.

The DDW has the most linear pitching moment curve

in the unblown case up to the onset of vortex breakdown where a sharp nose-up pitch occurs. This supports the findings of Spence and Lean (Ref. 26) which specify that delta wings pitch up more sharply as the incidence increases than do corresponding wings with streamwise tips. The LGW demonstrates an intensified nose-down pitching moment at high incidence which, according to Spence and Lean, is the behavior typical of a gothic wing with a high value of p_p. The MGW and SGW pitch-up at vortex breakdown is not as sharp as the DDW indicating that the vortex breakdown is less severe. This suggests that, in general, gothic wings or other slender shapes with "quasi-streamwise" tips are not as subject to vortex breakdown as are delta wings.

The gothic wings of the family are generally less stable than the DDW as anticipated because of the respective area distribution. The gothic wings have more lifting area toward the apex which tends to be destabilizing. The SGW and the MGW possess similar pitching moment slopes since their area distributions are both parabolic. The LGW, with its quartic area distribution and relatively large lifting surface well forward on the model, is the least stable of the family.

All the wings exhibit a negative pitching moment coefficient at zero lift coefficient owing to the positive camber of the models. Modification of the model camber would have to be made to obtain a positive pitching moment at zero lift. This could possibly be achieved by introducing negative camber near the trailing edge.

The aerodynamic center positions are plotted in Figs. 5•20a, 20b, 20c, and 20d for the DDW, SGW, MGW, and LGW, respectively. The aerodynamic center moves aft quite rapidly on all the wings with apex blowing as the wing incidence moves away from the low range where the flow field is unsettled. This is caused by the augmentation in lift on the rear portion of the model with apex blowing. With further increase in incidence at a given value of C_μ, the aerodynamic center position moves slowly forward which is normal for slender wings at low speeds. Spence and Smith (Ref. 17) point out that slight instability at higher incidences due to the gradual forward movement of the aerodynamic center, such as occurs with apex blowing, can be tolerated on slender-winged aircraft. Because of the gradual forward movement of the aerodynamic center position with incidence on these wings, the aft position of the center of gravity for positive longitudinal stability is defined by the approach attitude. Without apex blowing the aerodynamic center position is generally more stationary with incidence change until vortex breakdown occurs causing a rapid forward movement. This reaction to vortex breakdown is obviously unacceptable from longitudinal stability considerations. The LGW

displays a gradual movement aft of the aerodynamic center position at high incidence and no blowing which is normal for a gothic wing with a high value of p_p.

On all the wings tested the aerodynamic center position, at a given value of C_{L_A}, moves aft with initial apex blowing, $C_\mu = 0.04$, and then, with further increase in the blowing coefficient, moves forward. The DDW is the only wing on which this forward movement results in the aerodynamic center at $C_\mu = 0.12$ being forward of its position without blowing.

At $C_{L_A} = 0.7$, the aerodynamic center positions vary on the wings tested over the range of blowing coefficients as follows:

DDW: 0.589 to 0.598 c_o

SGW: 0.536 to 0.548 c_o

MGW: 0.534 to 0.555 c_o

LGW: 0.510 to 0.533 c_o

The center of gravity of an aircraft with a shape similar to the models tested would fall in the vicinity of 0.6 c_o without engines. From the above table it is apparent that longitudinal stability would be a problem since the center of gravity must be forward of the aerodynamic center. Installation of the engines in the nose would move the center of gravity forward an appreciable amount. This engine location has the added advantage of reducing the ducting difficulties associated with apex blowing. Even with the engines installed in the nose, the longitudinal stability of the LGW planform still appears marginal. The addition of a short fuselage-type extension on the nose of the basic planforms to house the engines and crew compartment, thus creating an ogee-type planform, would be a possible method of positioning the engines far enough forward to solve the longitudinal balance problem in an all-wing aircraft based on these models.

6. CONCLUSIONS

The flow field around a slender cambered model with apex blowing and the effect of planform variations on such a model have been investigated. The main conclusions reached as a result of this study are:

1. The blowing air formed discrete jets which followed curved paths over the model shoulders and along the central portion of the model to the trailing edge. The shape of the jet paths was the consequence of the model thickness and the resulting high suction on the shoulders at mid-centerline chord.
2. With apex blowing the leading edge vortices did not begin to develop on the BW model until aft of 40% centerline chord where the blowing air jet crossed the leading edge.
3. The natural growth of the leading edge vortices was less restricted by the model shoulders as the distance between the leading edges and the shoulders became larger.
4. Apex blowing increased the aerodynamic lift on all the models at incidences above 4°, approximately, and decreased it at negative incidences. The flow produced irregular results at incidences between 0° and $+4^{\circ}$.
5. Vortex breakdown affected the straight-edged models more than it did the gothic models at $C_{\mu} = 0$. The gothic wings required higher values of C_{μ} than the straight-edged wings to completely eliminate the effects of vortex breakdown. The LGW was free of vortex breakdown throughout the incidence range tested.
6. The highest values of C_{L_A}, at a given incidence and blowing coefficient, and the greatest increment in lift due to apex blowing were obtained on the MGW. On all the wings, the largest lift increment attributable to apex blowing occured with $C_{\mu} = 0.04$.
7. The empirical relationship between the aerodynamic lift with and without apex blowing for this family of wings was ascertained to be:

$$\left[\frac{C_{L_A}}{\sqrt{s/c'}}\right]_{C_{\mu}=0} = \left[\frac{C_{L_A}}{\sqrt{s/c'}}\right]_{C_{\mu}} \left(1 - 0.84\, C_{\mu}^{0.621}\right)$$

8. The lift-dependent drag was lessened on all the wings with mounting values of the blowing coefficient, C_{μ}. The largest decrement in lift-dependent drag over the range of blowing coefficients tested occured on the MGW.

9. The maximum lift-drag ratio was less at low values of C_μ than at $C_\mu = 0$ but exhibited a net gain at $C_\mu = 0.12$ on all wings. At $C_{L_A} > 0.4$ the lift-drag ratio was boosted on all the models as the blowing coefficient was increased.

10. In the unblown cases, the lift-dependent drag factors, K, were less than the corresponding empirical values due to Kirby for flat-plate delta wings. The values of K were reduced by increasing the blowing coefficient and, at $C_\mu = 0.12$, they approached the theoretical values due to J. H. B. Smith for flat plates in conical flow.

11. Apex blowing had a stabilizing effect at moderate values of C_{L_A}. The range of useable lift coefficients was extended by apex blowing. The pitching moment coefficient was negative at zero lift on all wings.

12. The aerodynamic center positions at a given blowing coefficient moved gradually forward with rising values of C_{L_A} except on the LGW. There was a rapid forward movement of the aerodynamic center position with the occurance of vortex breakdown.

13. A comparison between an all-wing airbus with apex blowing and one without suggested that apex blowing could reduce the required landing distance by about 28%. With apex blowing the resultant lift to gross thrust ratio was the highest in the cruise condition on the BW and in the approach condition on the MGW. Mounting the engines in the nose of an all-wing aircraft can reduce the longitudinal stability problems and aid in the implementation of an apex blowing system.

14. Further experimentation in the field of apex blowing is recommended although a more versatile model than the present one is required. This model should allow one to investigate the effects contingent upon variations in thickness, camber, apex blowing angles, and planform shape -- both independently and jointly.

REFERENCES

1. Jones, R. T.: Properties of Low-aspect-ratio Pointed Wings at Speeds below and above the Speed of Sound, N.A.C.A., Rep. 835, 1946.

2. Legendre, R.: Flow in the Neighborhood of the Apex of a Highly Swept Wing at Moderate Incidences, A.R.C. 16,796. Translated from La Recherche Aéronautique No. 30, 1952.

3. Maskell, E. C., and J. Weber: On the Aerodynamic Design of Slender Wings, Journal of the Royal Aeronautical Society, 1959, Vol. 63, pp. 709 - 721.

4. Lee, G. H.: Reduction of Lift-dependent Drag with Separated Flow, A.R.C., C.P. 593, 1962.

5. Maskell, E. C., and D. Kuchemann: Controlled Separation in Aerodynamic Design, R.A.E., T.M. Aero. 463, March 1956.

6. Trebble, W. J. G.: Exploratory Investigation of the Effects of Blowing from the Leading Edge of a Delta Wing, R.A.E., T.R. 66,125, April 1966.

7. Alexander, A. J.: The Aerodynamic Characteristics of the Jet Wing and its Application to High Speed Aircraft, Unpublished University of London PhD Thesis, 1961.

8. Kuchemann, D., and J. Weber: An Analysis of Some Performance Aspects of Various Types of Aircraft Designed to Fly over Different Ranges at Different Speeds, R.A.E., T.R. 66,188, June 1966.

9. Gates, S. B.: The All-wing Aircraft, New Scientist, 27 May 1965, Vol. 26, pp. 592 - 594.

10. Hyde, L. L.: Low Speed Wind Tunnel Tests on a Slender Delta Wing with Blowing from the Apex, Unpublished College of Aeronautics, Cranfield Thesis, 1967.

11. Kirkpatrick, D. L. I., and J. D. Field: Experimental Investigation of the Positions of the Leading Edge Vortices above Slender Delta Wings with Various Rhombic Cross Sections in Subsonic Conical Flow, R.A.E., T.R. 66,068, March 1966. (also A.R.C., C.P. 925, 1967).

12. Pankhurst, R. C., and D. W. Holder: Wind-Tunnel Techniques, pp. 146 - 147, Sir Isaac Pitman and Sons, Ltd., London, 1952.

13. Squire, L. C.: Some Effects of Thickness on the Longitudinal Characteristics of Sharp Edged Delta Wings at Low Speeds, Journal of the Royal Aeronautical Society, February 1968, Vol. 72, pp. 151 - 155.

14. Earnshaw, P. B.: An Experimental Investigation of the Structure of a Leading Edge Vortex, A.R.C., R. & M. 3,281, 1962.

15. Lambourne, N. C., and D. W. Bryer: Some Measurements in the Vortex Flow Generated by a Sharp Leading Edge Having 65-degrees Sweep, A.R.C., C.P. 477, 1960.

16. Zijnen, B. G. Von Der Hegge: Measurements of the Velocity Distribution in a Plane Turbulent Jet of Air, Applied Scientific Research, 1958, Vol. 7, pp. 256 - 276.

17. Spence, A., and J. H. B. Smith: Some Aspects of the Low Speed and Supersonic Aerodynamics of Lifting Slender Wings, Proceedings 3rd I.C.A.S., Stockholm, 1962, Spartan Books, 1964, p. 553.

18. Lambourne, N. C.: Breakdown of Certain Types of Vortex, A.R.C., C.P. 915, 1967.

19. Hall, M. G.: The Structure of Concentrated Vortex Cores, Progress in Aeronautical Science, Vol. 7, pp. 53 - 110, Pergamon Press, Oxford, 1966.

20. Hyde, L. L.: Wind Tunnel Tests on Slender Delta Wings with Leading Edge Blowing, Unpublished Laboratory Notebook Containing Results of Tests in 8 ft. x 6 ft. Low Speed Wind Tunnel at College of Aeronautics, Cranfield, 1967.

21. Squire, L. C.: Some Applications of 'Not-So-Slender' Wing Theory to Wings with Curved Leading Edges, A.R.C., R. & M. 3,278, July 1960.

22. Brown, C. E., and W. H. Michael: Effect of Leading-edge Separation on the Lift of a Delta Wing, Journal of Aeronautical Sciences, 1954, Vol. 21, pp. 690 - 694. (also N.A.C.A., T.N. 3,430).

23. Peckham, D. H.: Low-Speed Wind Tunnel Tests on a Series of Uncambered Slender Pointed Wings with Sharp Edges, A.R.C., R. & M. 3,186, December 1958.

24. Earnshaw, P. B., and J. A. Lawford: Low-Speed Wind Tunnel Experiments on a Series of Sharp-Edged Delta Wings, A.R.C., R. & M. 3,424, 1966.

25. Kirby, D.: Personal interview on 12 June 1968 concerning unpublished results of tests on slender wing models at R.A.E. Farnborough.

26. Spence, A., and D. Lean: Some Low Speed Problems of High Speed Aircraft, Journal of the Royal Aeronautical Society, 1962, Vol. 66, p. 211. (also A.G.A.R.D., Rep. 357).

27. Department of Aerodynamics Lecture Supplements and Data Sheets, Vol. 1, College of Aeronautics, Cranfield.

28. Note on the Calibration of 8 ft. x 6 ft. Wind Tunnel Balance, College of Aeronautics, Cranfield, September 1962.

29. Spiegel, M. R.: Theory and Problems of Statistics, Schaum Publishing Co., New York, 1961.

30. Downie, N. M., and R. W. Heath: Basic Statistical Methods, Harper and Row, Publishers, New York, 1959.

31. Pinsker, W. J. G.: "Zero Rate of Climb Speed" as a Low Speed Limitation for the Stall Free Aircraft, A.R.C., C.P. 931, 1967.

TABLE I
SPECIFICATIONS OF THE MODELS

	BW	DDW	SGW	MGW	LGW
AR	1.50	1.90	1.30	1.60	1.50
b (in.)	36.0	43.2	36.0	43.2	43.2
c_o (in.)	48.0	48.0	48.0	48.0	48.0
c_o' (in.)	48.0	44.7	40.1	38.8	36.4
p_p	0.500	0.475	0.582	0.563	0.605
S, S_m (sq.ft.)	6.00	6.84	6.98	8.10	8.72
s (in.)	18.0	21.6	18.0	21.6	21.6
$\sqrt{s/c_o'}$	0.613	0.695	0.670	0.746	0.770

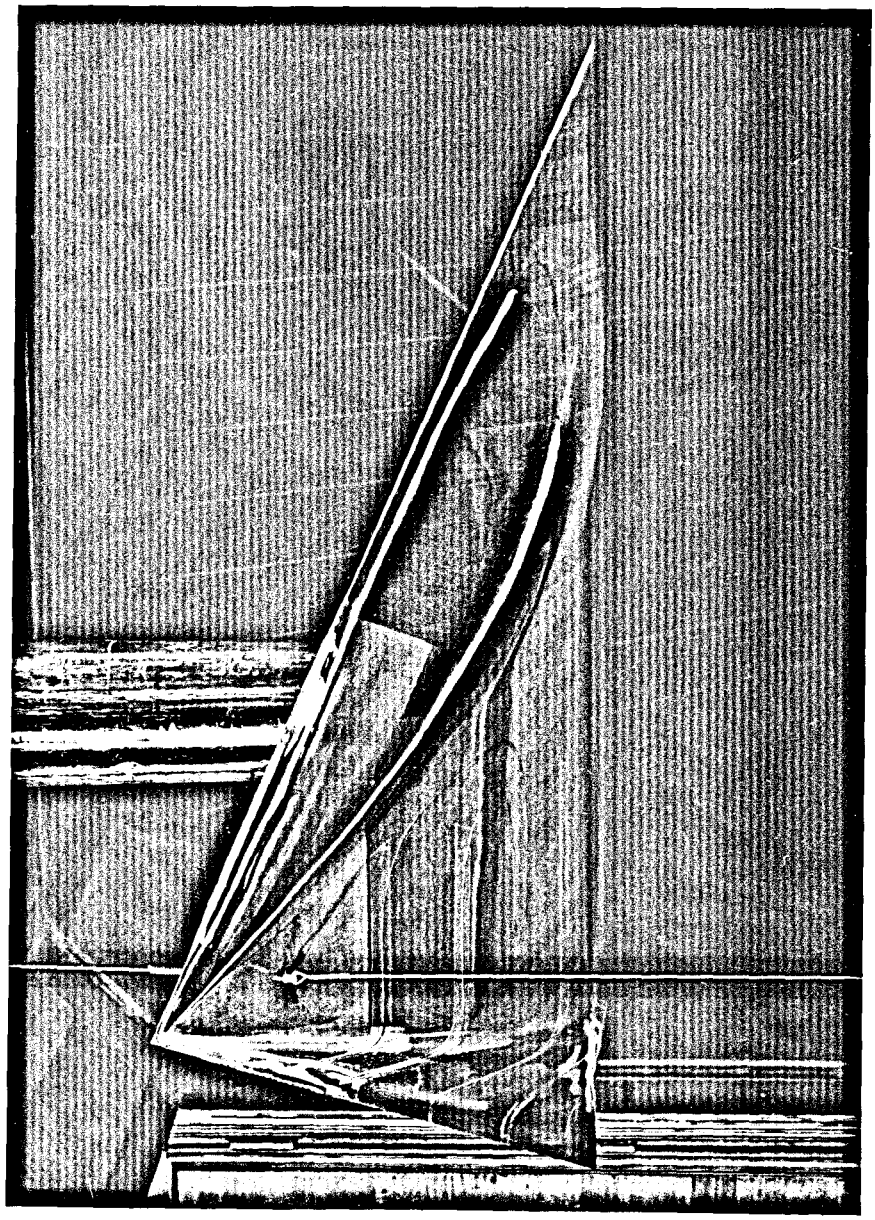

FIG. 3.1. BW MODEL MOUNTED IN WIND TUNNEL.

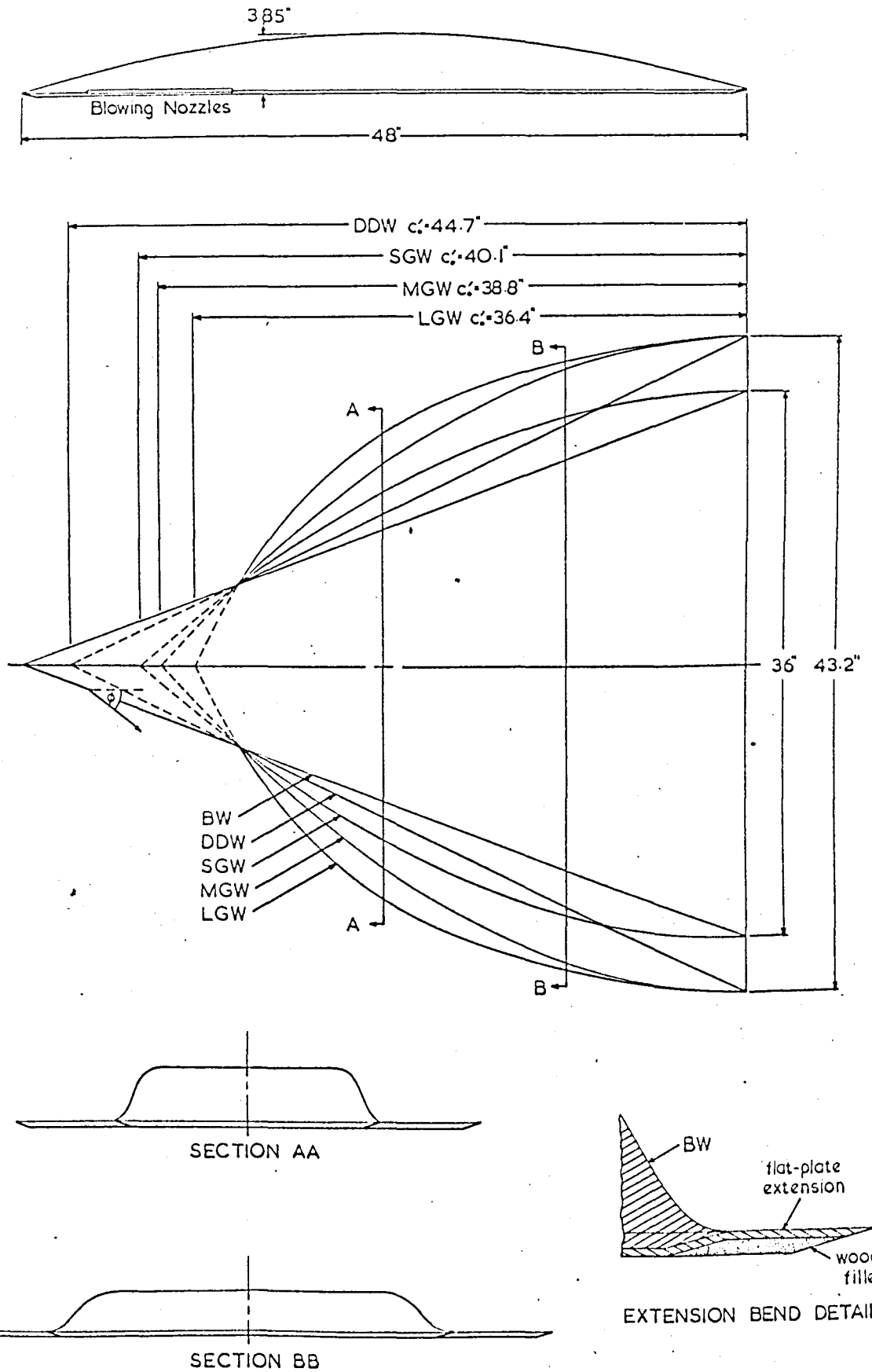

FIG. 3.2. GENERAL LAYOUT OF THE MODELS.

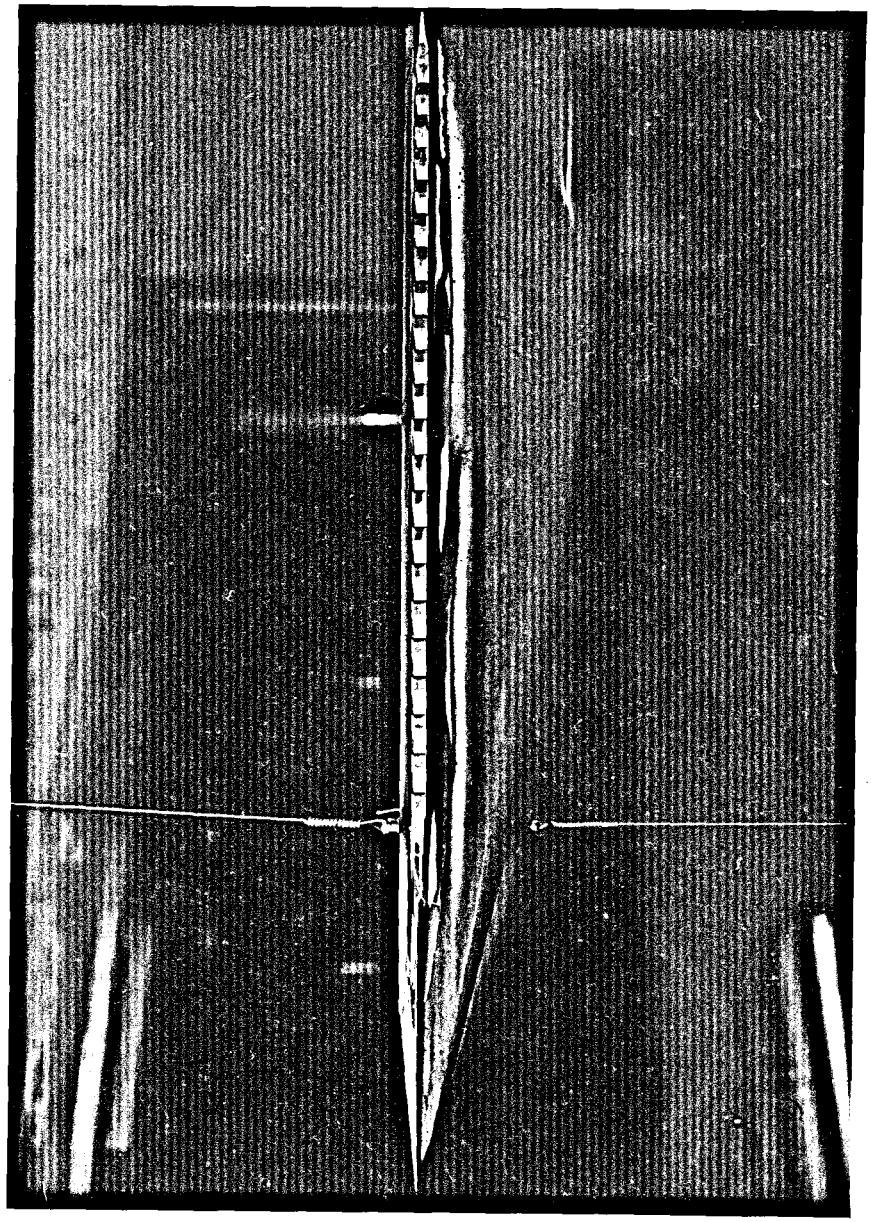

FIG. 3.3. APEX BLOWING NOZZLES.

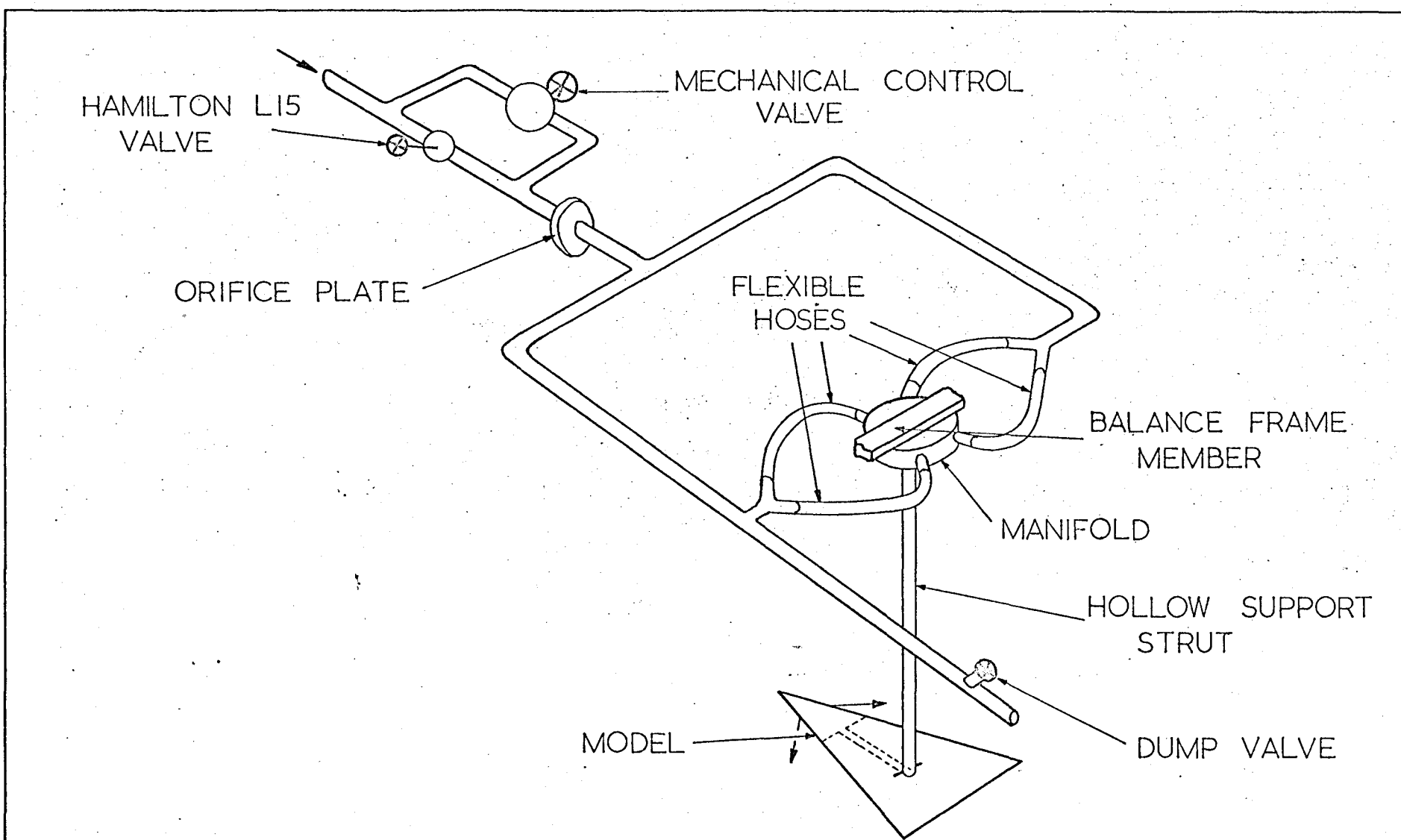

FIG. 3.4. BLOWING SYSTEM.

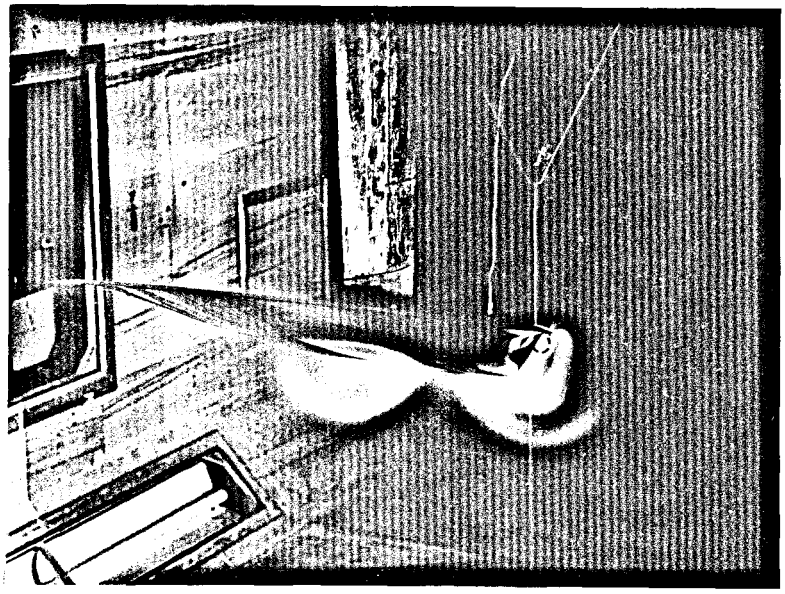

a. $x/c_o = 0.50$

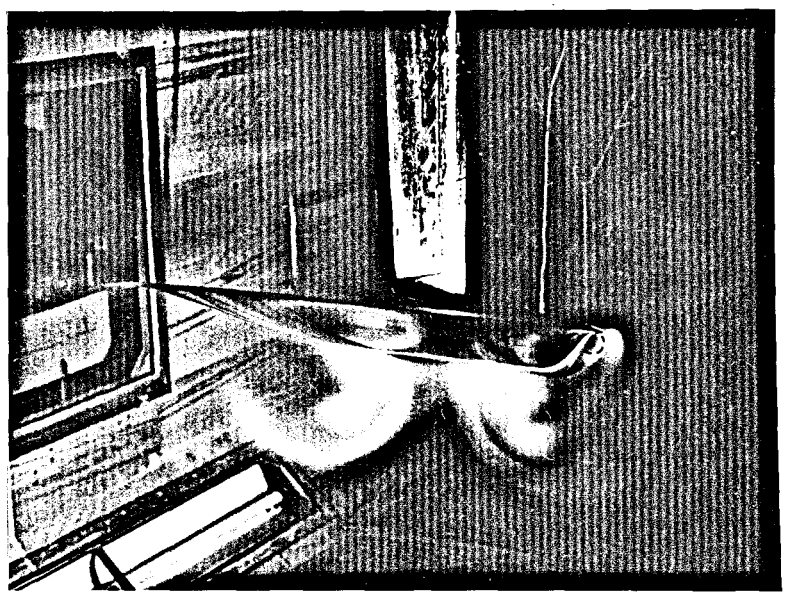

b. $x/c_o = 0.70$

c. $x/c_o = 0.90$

FIG. 5.1. FLOW FIELD ON BW, $\alpha = 15.6°$, $C_\mu = 0.08$.

a. $x/c_o = 0.50$

b. $x/c_o = 0.70$

c. $x/c_o = 0.90$

FIG. 5.2. FLOW FIELD ON MGW, α 15.6°, C_μ 0.08.

FIG. 5.28. x/c=0.50 VARIATION OF TOTAL HEAD COEFFICIENT THROUGH FLOW FIELD ON BW. C_μ=0.08, α = 15.6°. (backing plate)

FIG. 5.28. x/c=0.80. VARIATION OF TOTAL HEAD COEFFICIENT THROUGH FLOW FIELD ON BW, C_L=0.08, α = 15.6°. (backing plate)

FIG. 5.2b. x/c=0.80. VARIATION OF TOTAL HEAD COEFFICIENT THROUGH FLOW FIELD ON BW, C_μ=0.08, α = 15.6°. (backing plate)

FIG. 5.3b. x/c = 0.40. VARIATION OF TOTAL HEAD COEFFICIENT THROUGH FLOW FIELD ON BW, $C_\mu = 0.08$, $\alpha = 15.6^\circ$. (backing plate)

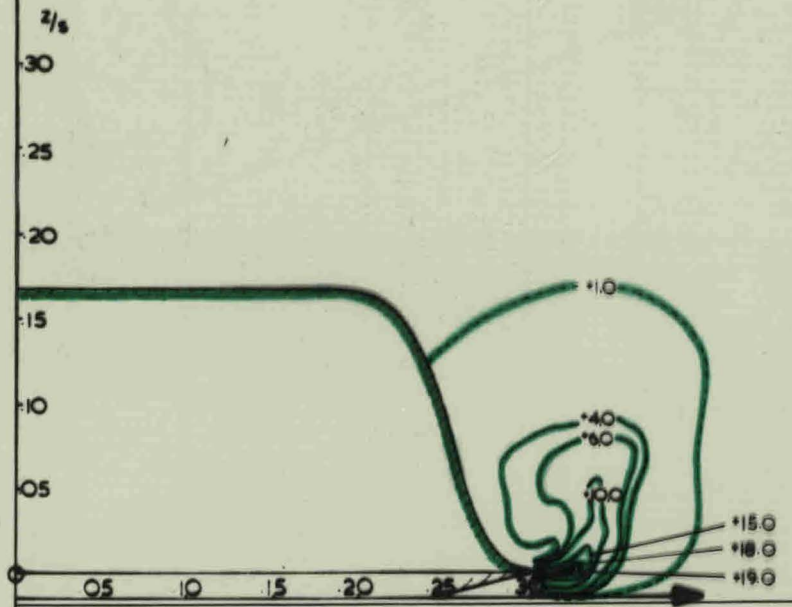

FIG. 5.30. x/c = 0.30. VARIATION OF TOTAL HEAD COEFFICIENT THROUGH FLOW FIELD ON BW, $C_\mu = 0.08$, $\alpha = 15.6^\circ$. (backing plate)

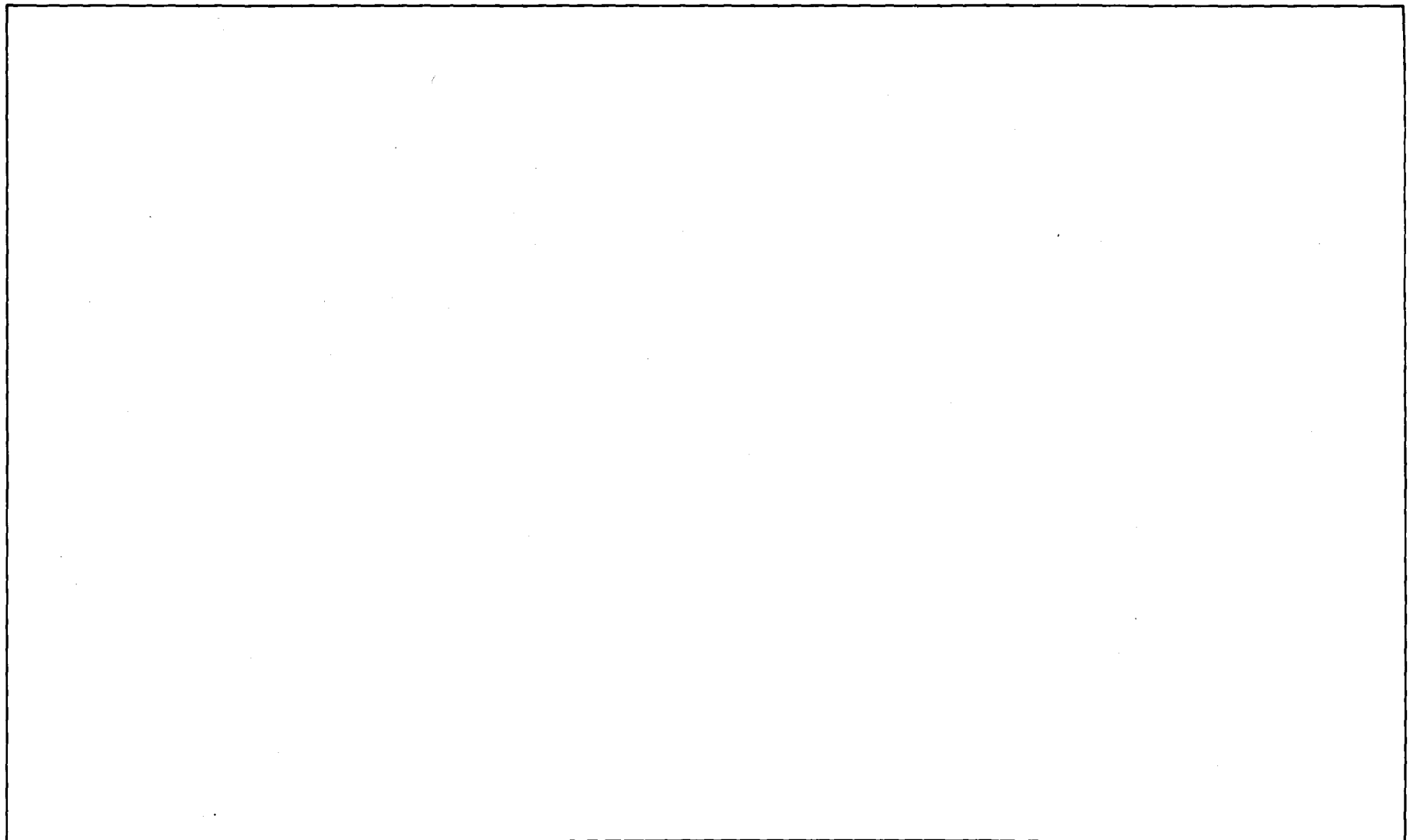

FIG. 5.3 . VARIATION OF TOTAL HEAD COEFFICIENT THROUGH FLOW FIELD ON BW, $C_\mu = 0.08$, $\alpha = 15.6^\circ$. (backing plate)

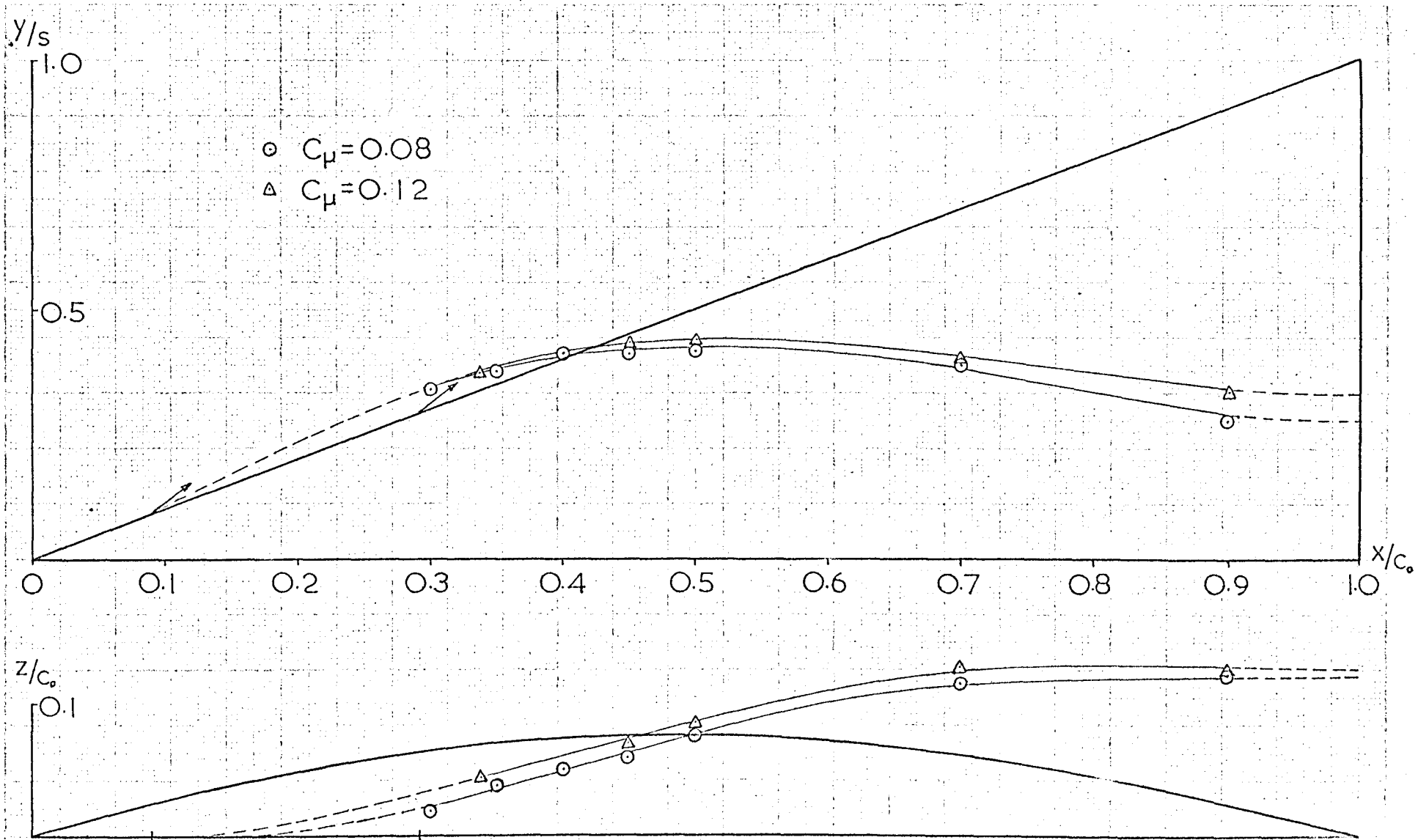

FIG. 5.4. BLOWING JET PATHS OVER BW, α=15.6°.

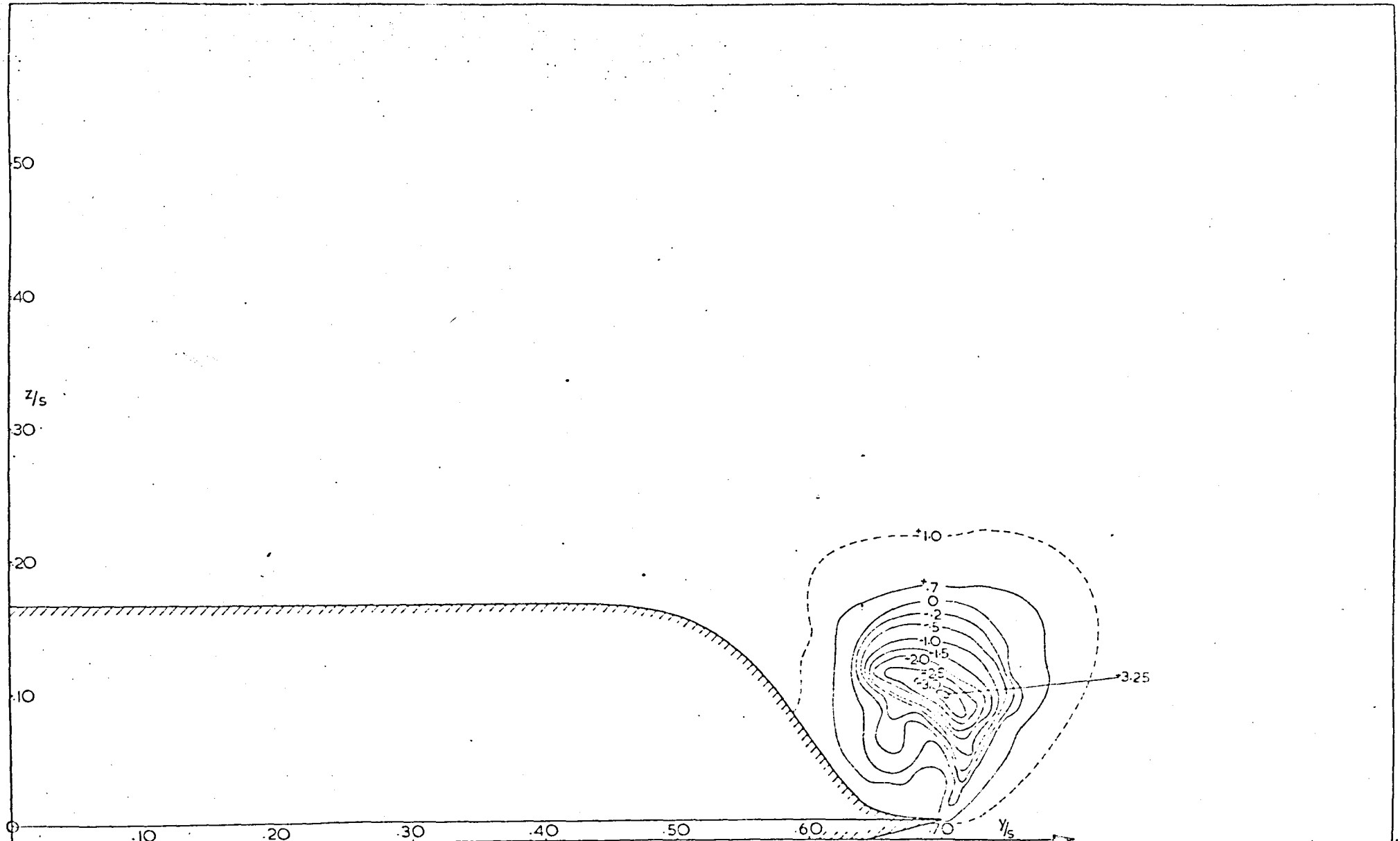

FIG. 5-5. VARIATION OF TOTAL HEAD COEFFICIENT THROUGH VORTEX ON BW. x/c.= 0·70. C_ν = 0. α = 15·6°.

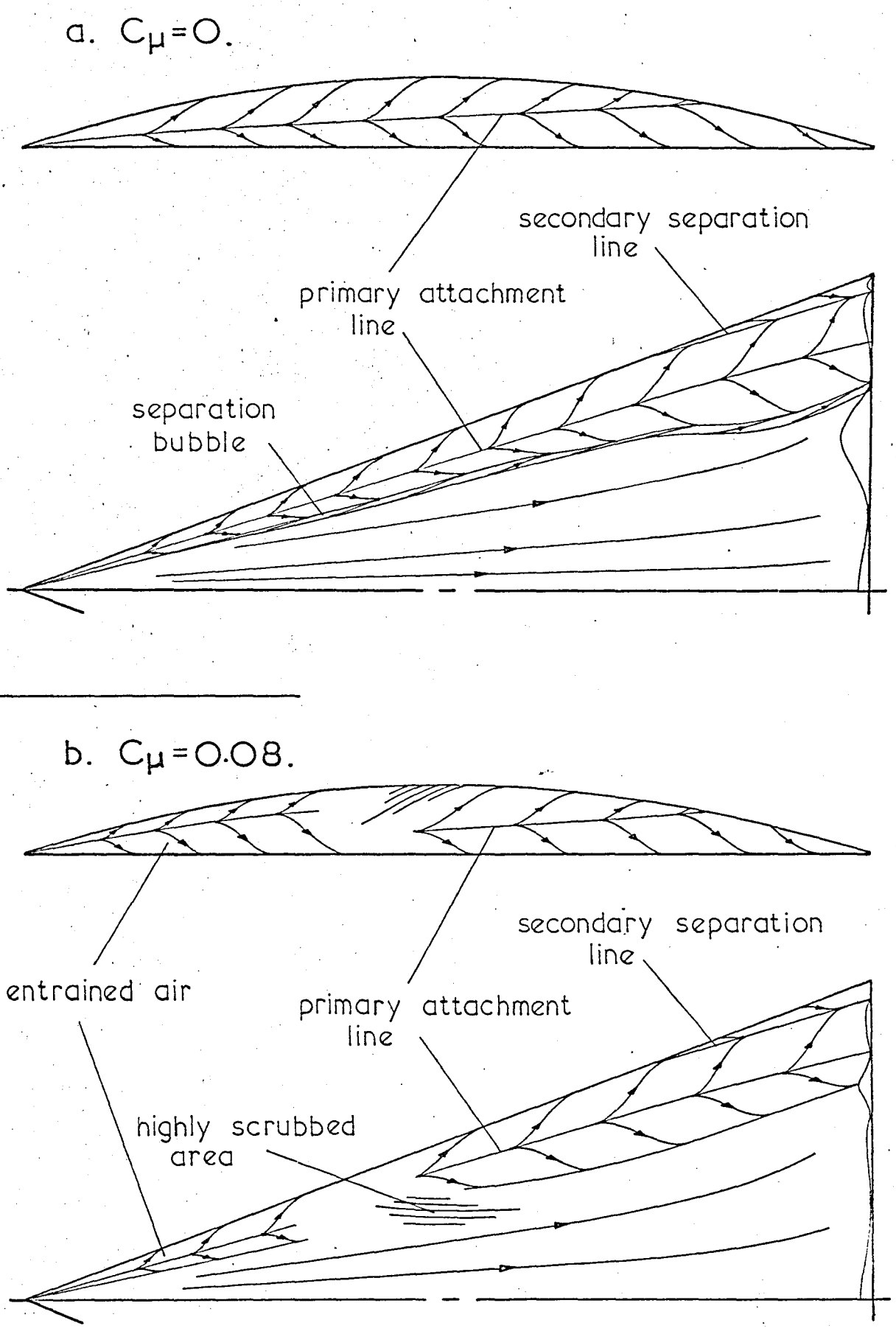

FIG. 5.6. SURFACE FLOW PATTERNS ON BW AT $\alpha = 15.6°$.

a. $C_\mu = 0$.

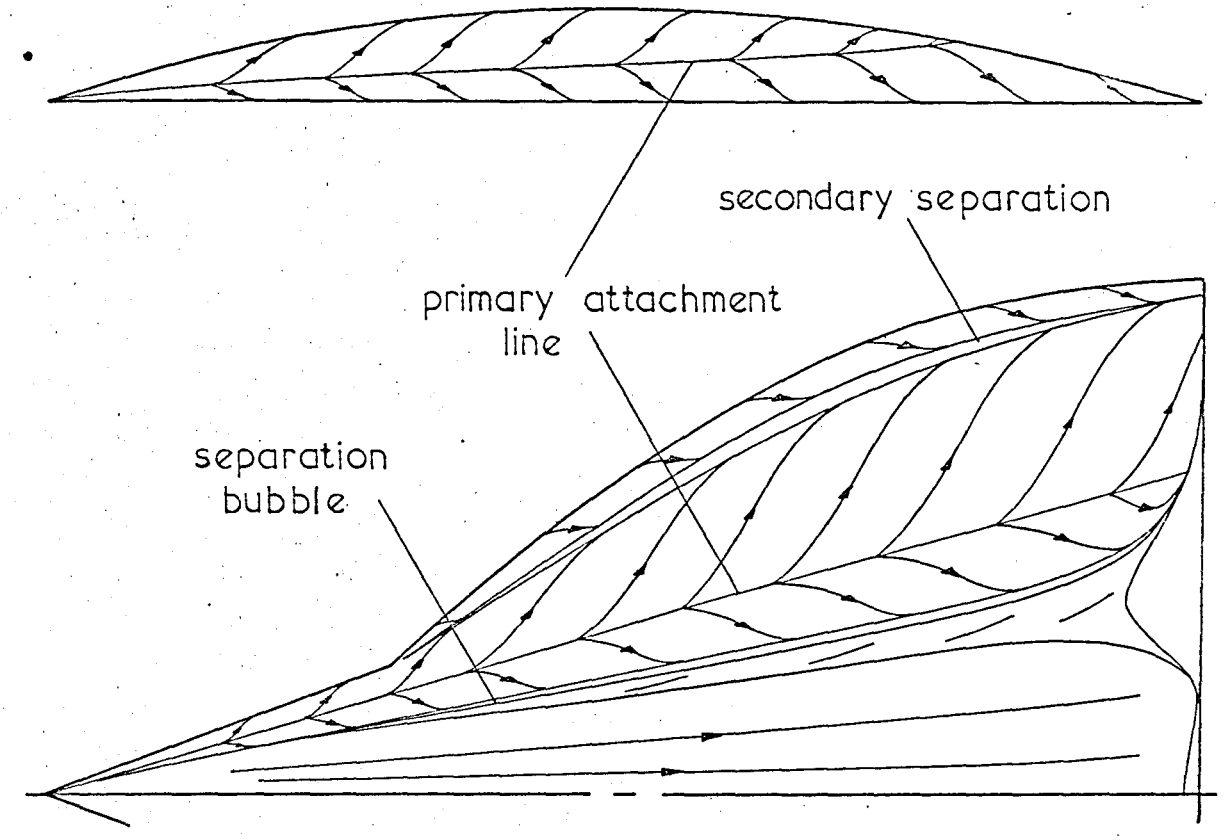

b. $C_\mu = 0.08$.

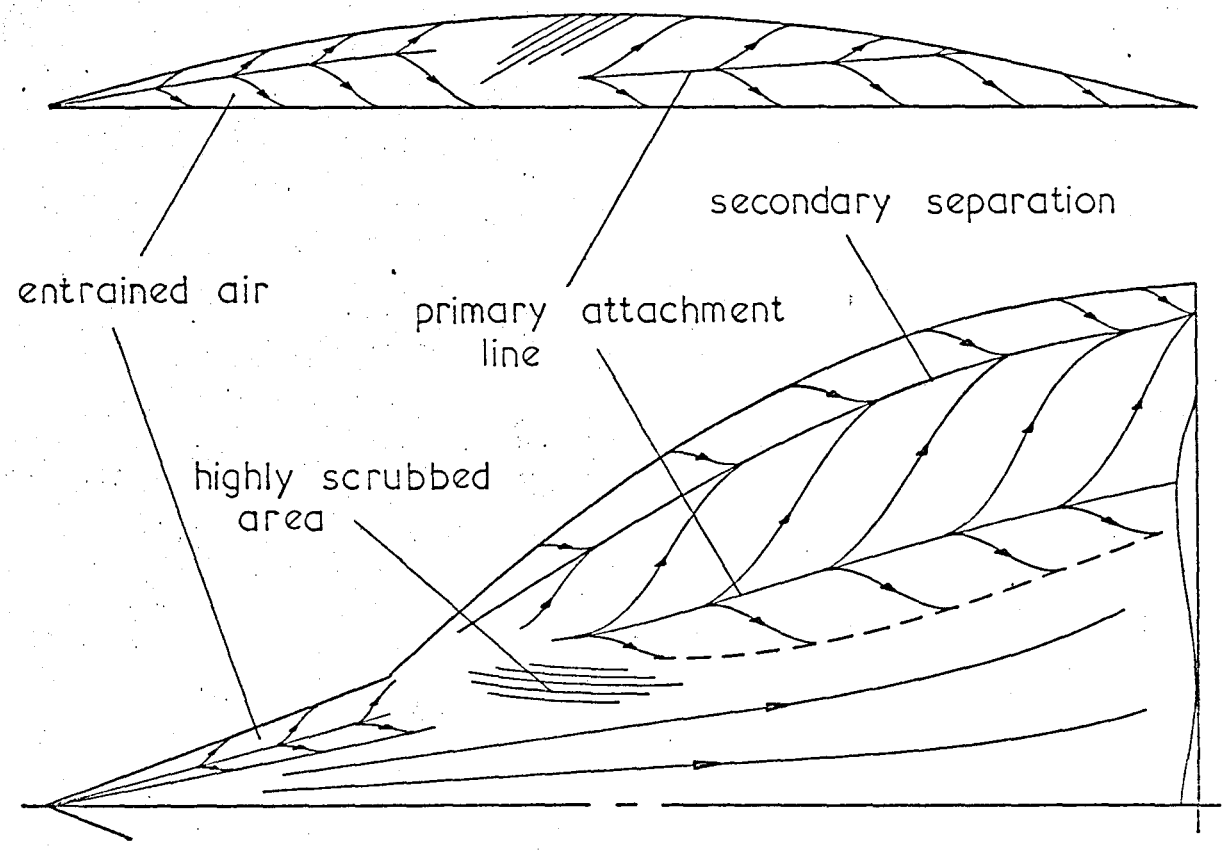

FIG. 5.7. SURFACE FLOW PATTERNS ON MGW AT $\alpha = 15.6°$.

a. $C_\mu = 0$.

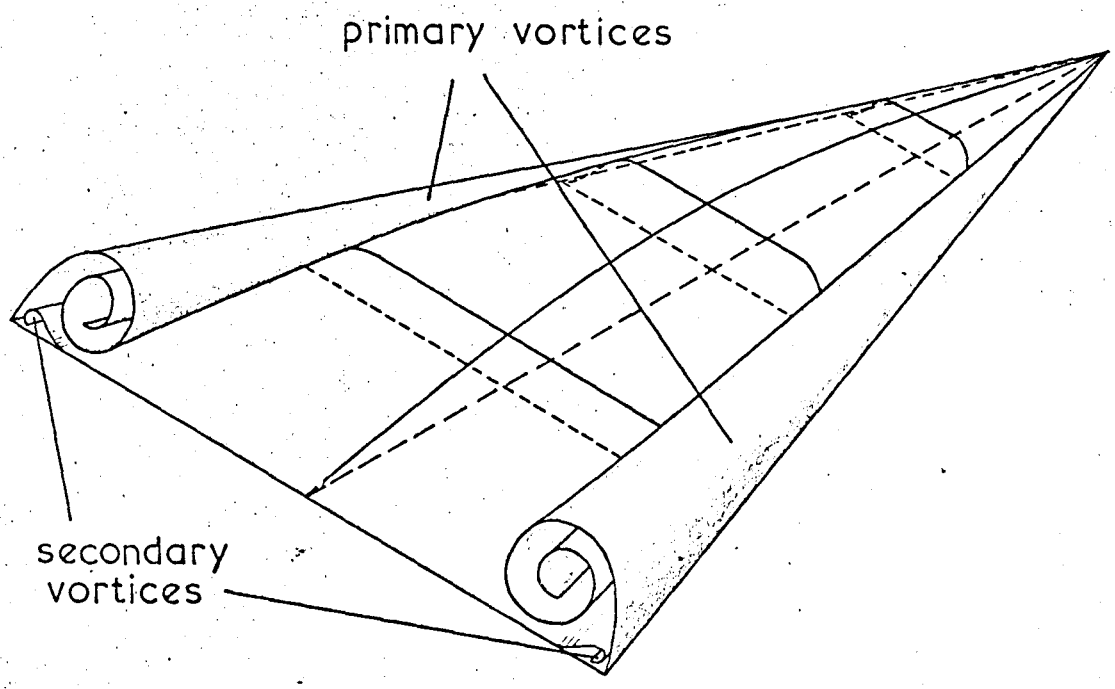

b. $C_\mu = 0.08$.

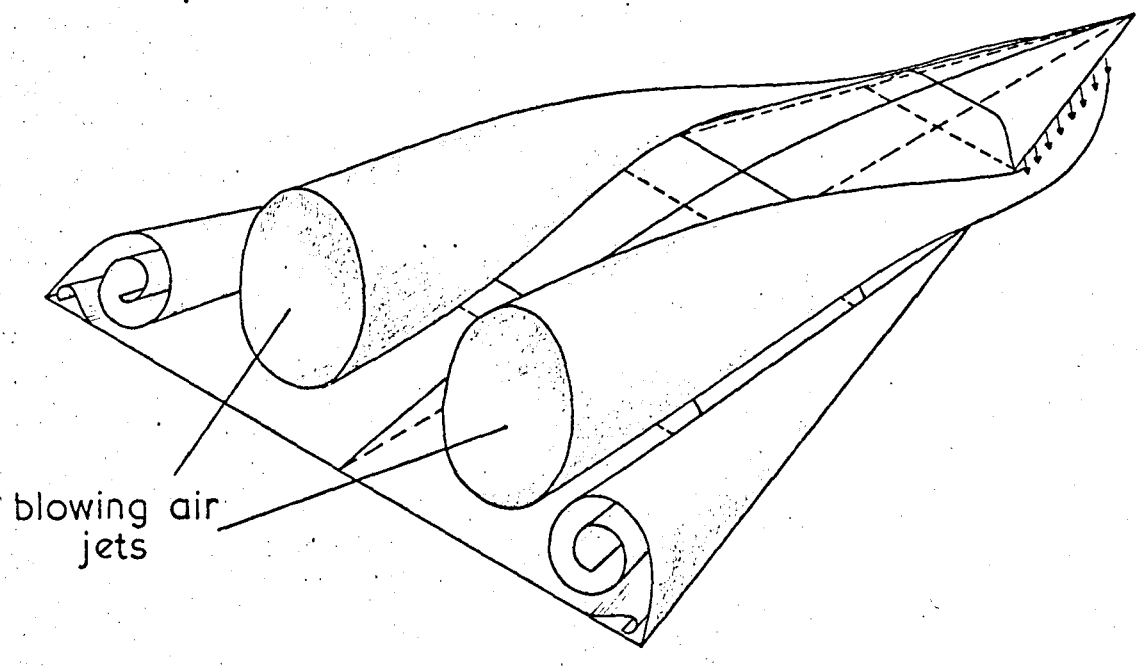

FIG. 5.8. PICTURIZATION OF FLOW FIELD ON BW.

a. $C_\mu = 0$.

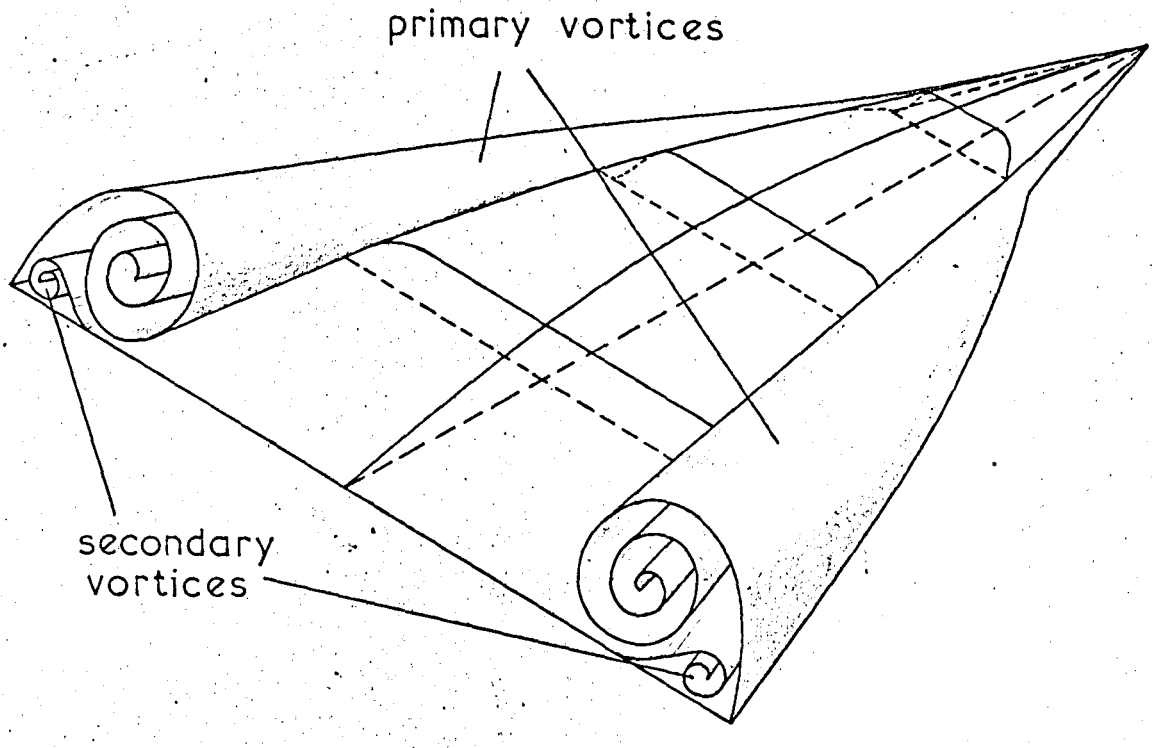

b. $C_\mu = 0.08$.

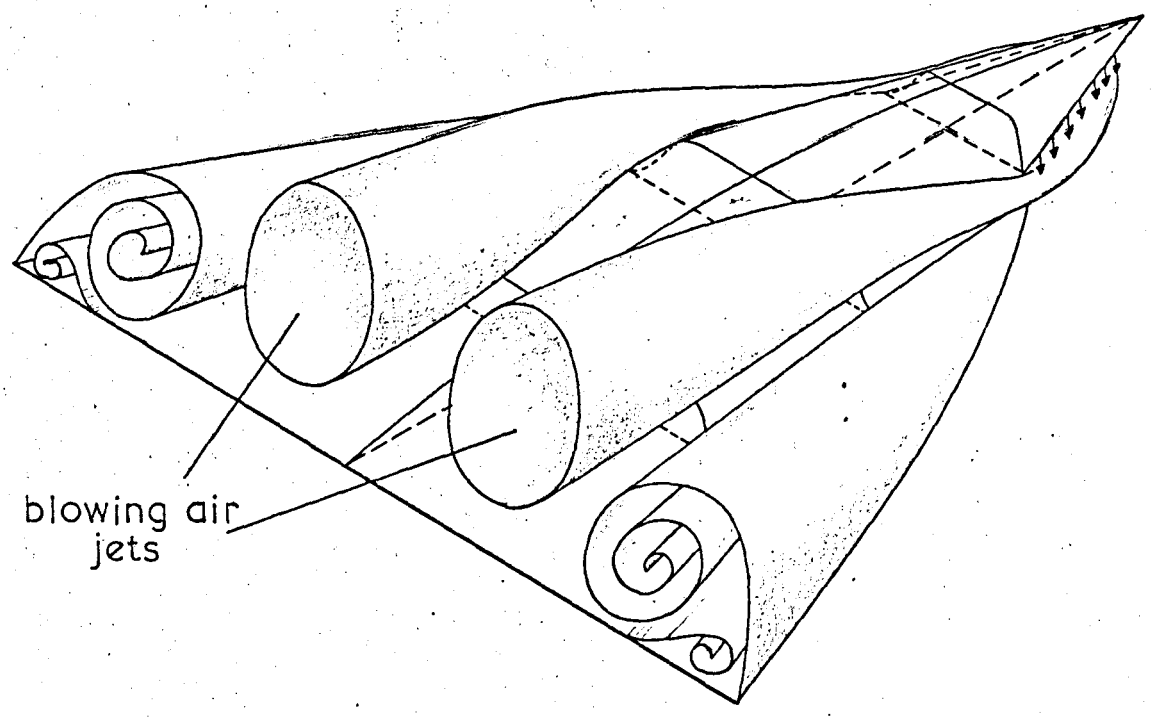

FIG. 5.9. PICTURIZATION OF FLOW FIELD ON MGW.

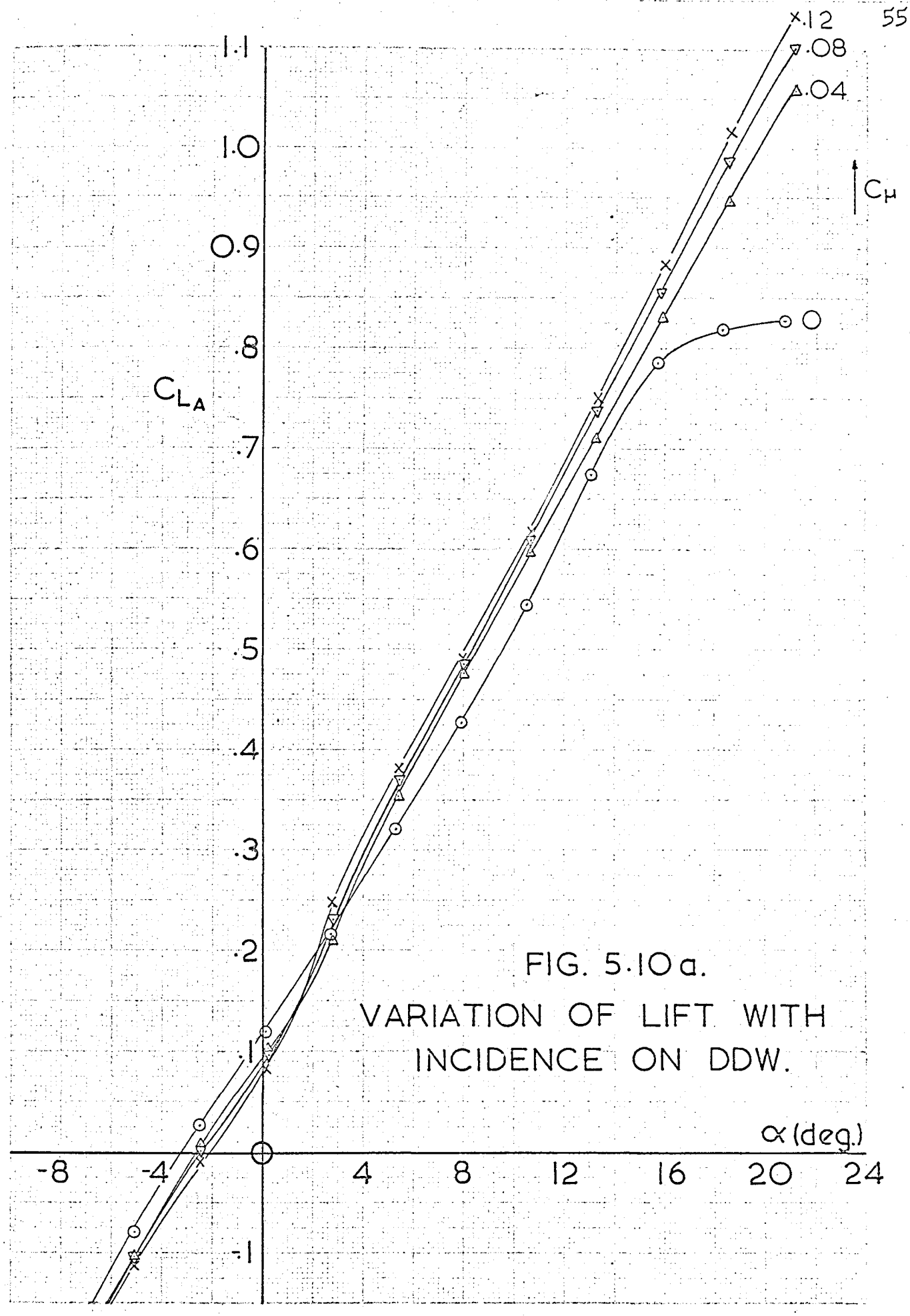

FIG. 5.10 a.
VARIATION OF LIFT WITH INCIDENCE ON DDW.

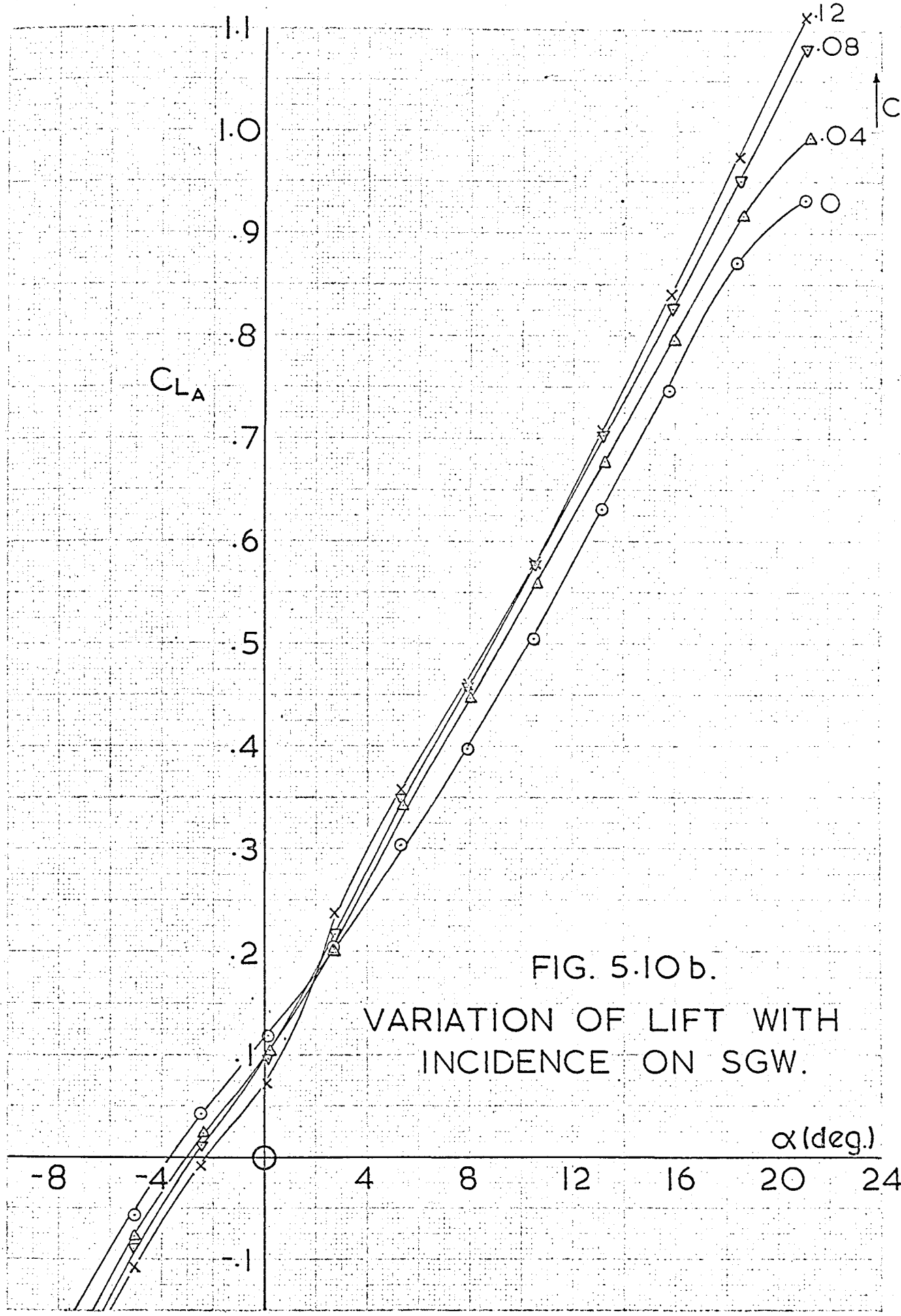

FIG. 5.10 b.

VARIATION OF LIFT WITH INCIDENCE ON SGW.

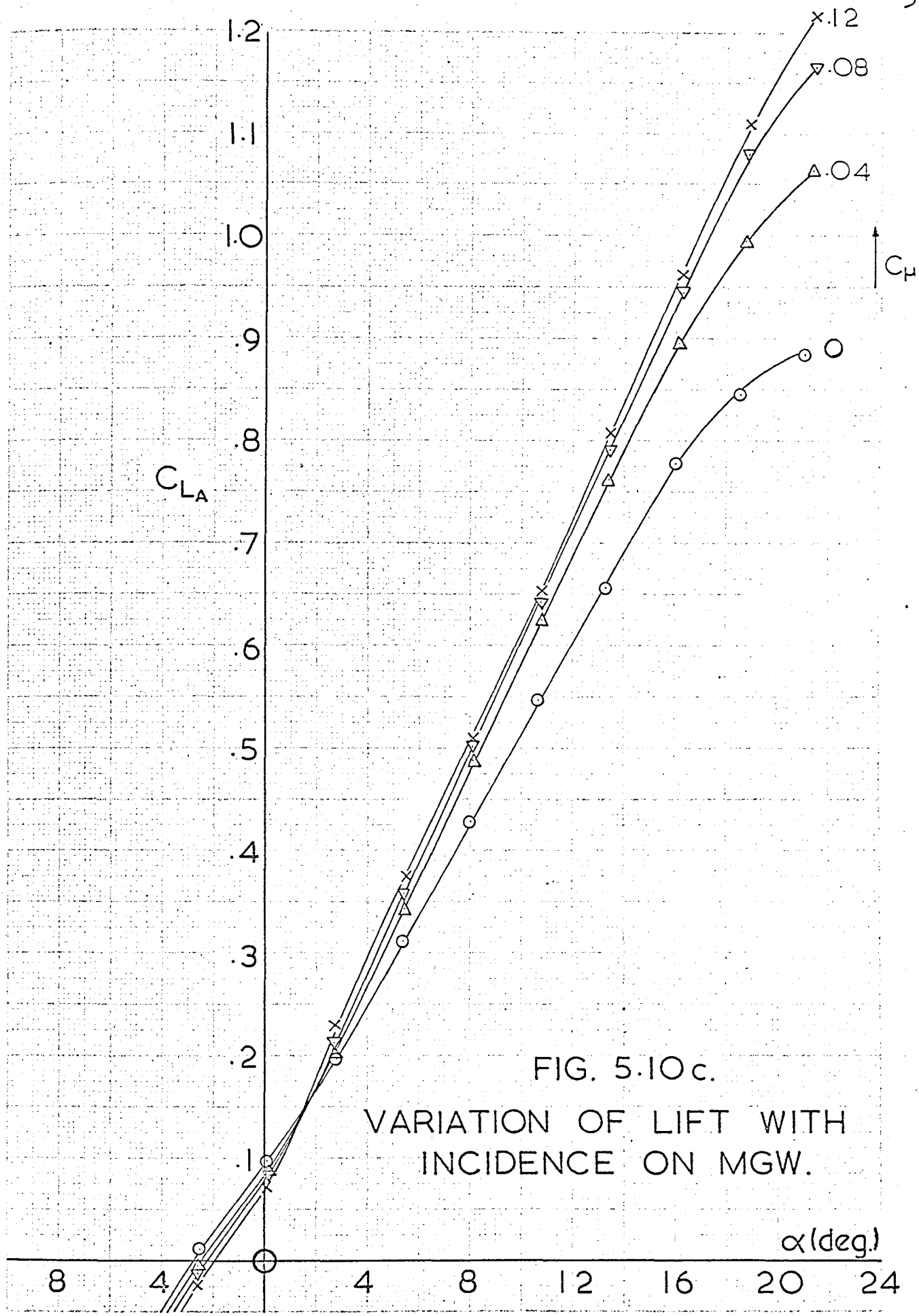

FIG. 5.10c.

VARIATION OF LIFT WITH INCIDENCE ON MGW.

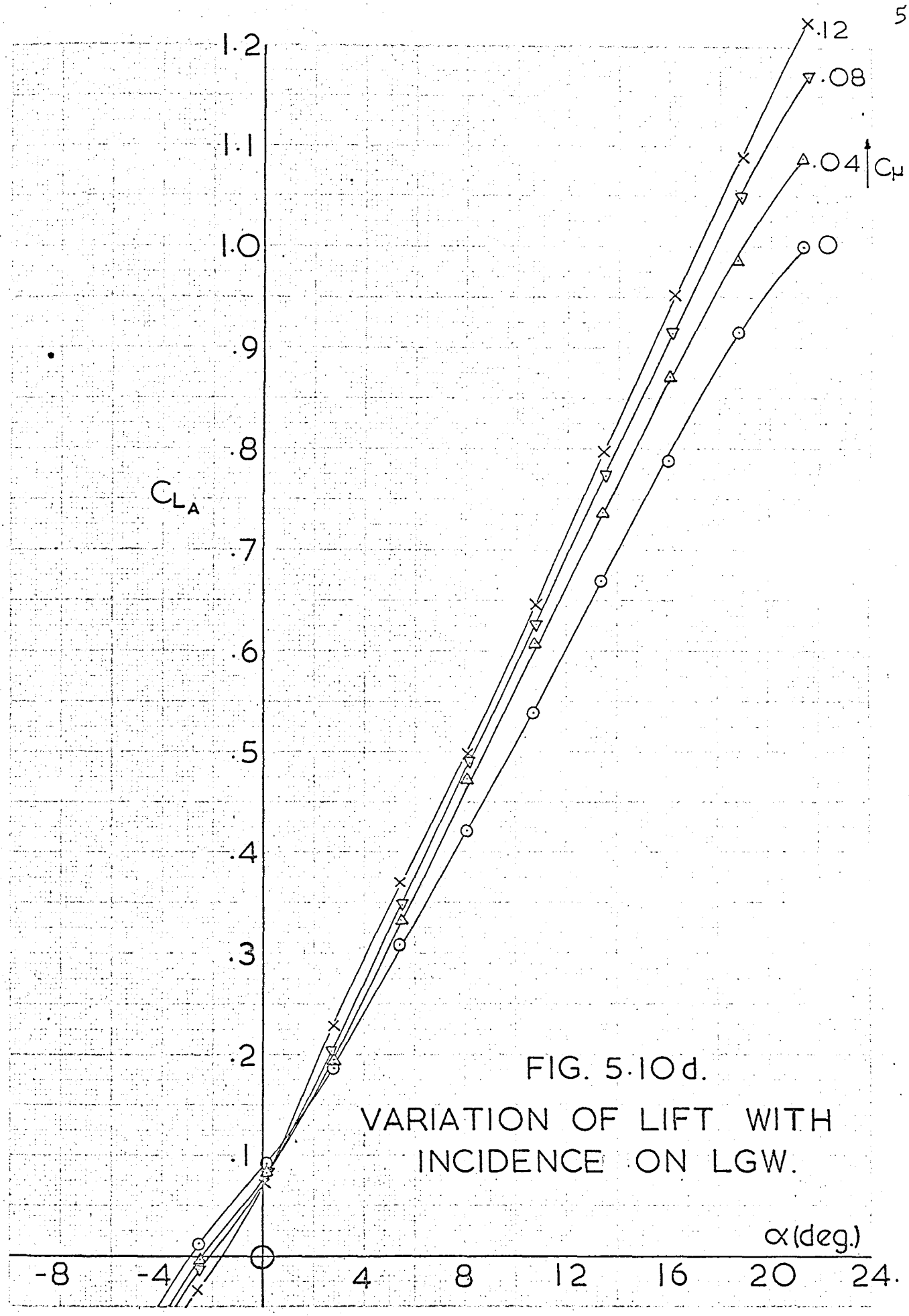

FIG. 5·10d.

VARIATION OF LIFT WITH INCIDENCE ON LGW.

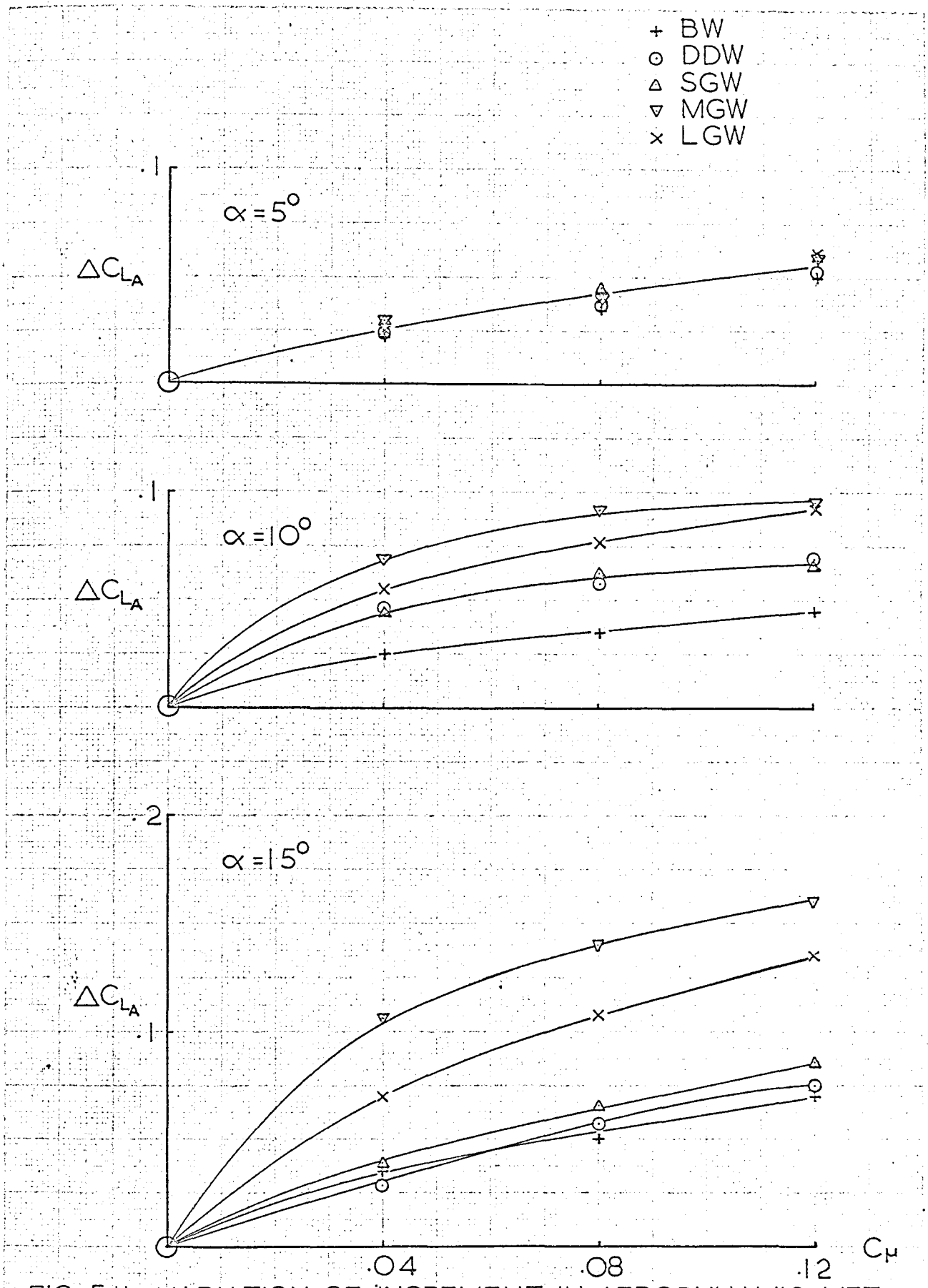

FIG. 5.11. VARIATION OF INCREMENT IN AERODYNAMIC LIFT DUE TO APEX BLOWING WITH MOMENTUM COEFFICIENT.

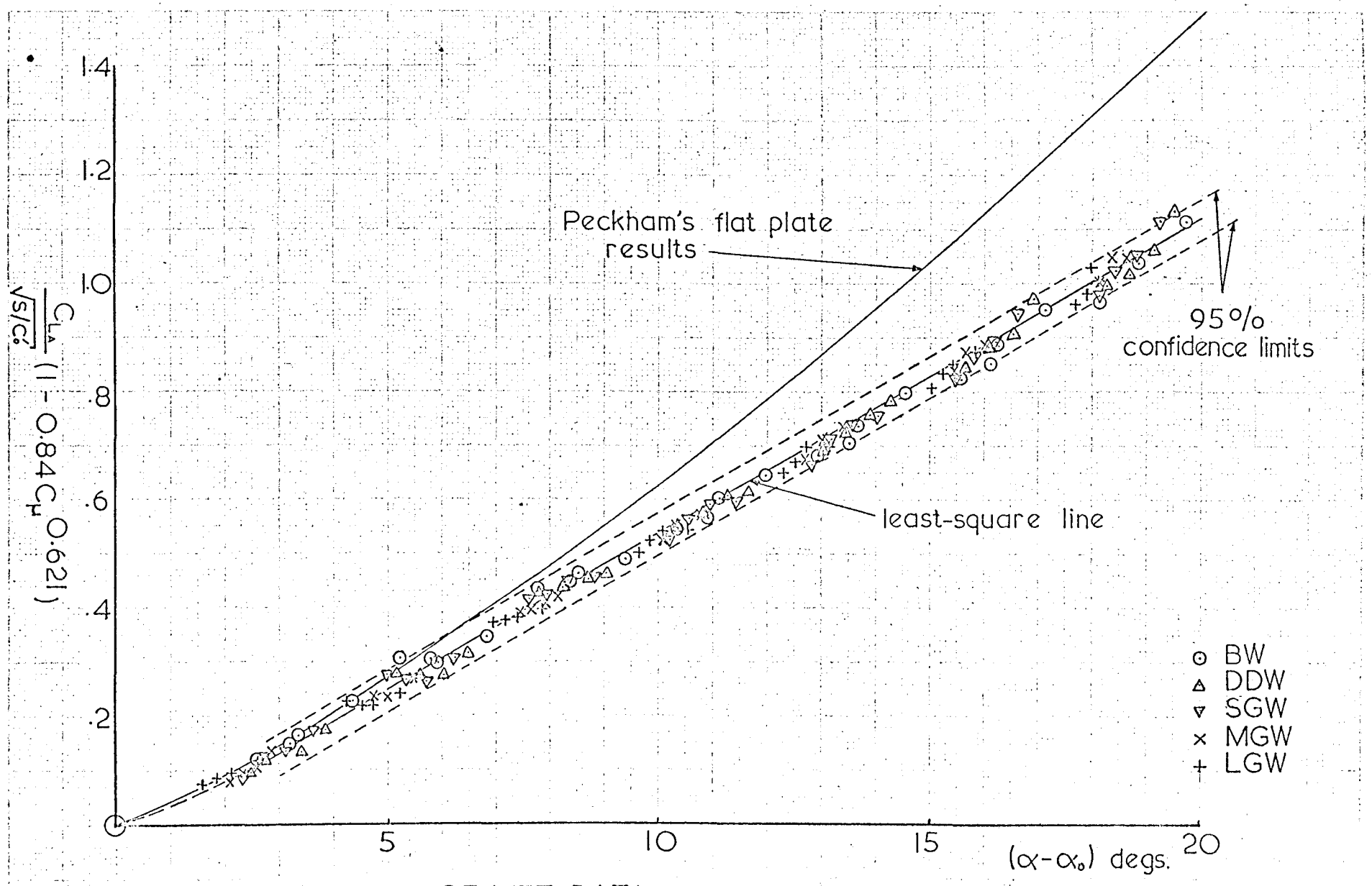

FIG. 5.12 COLLAPSE OF LIFT DATA.

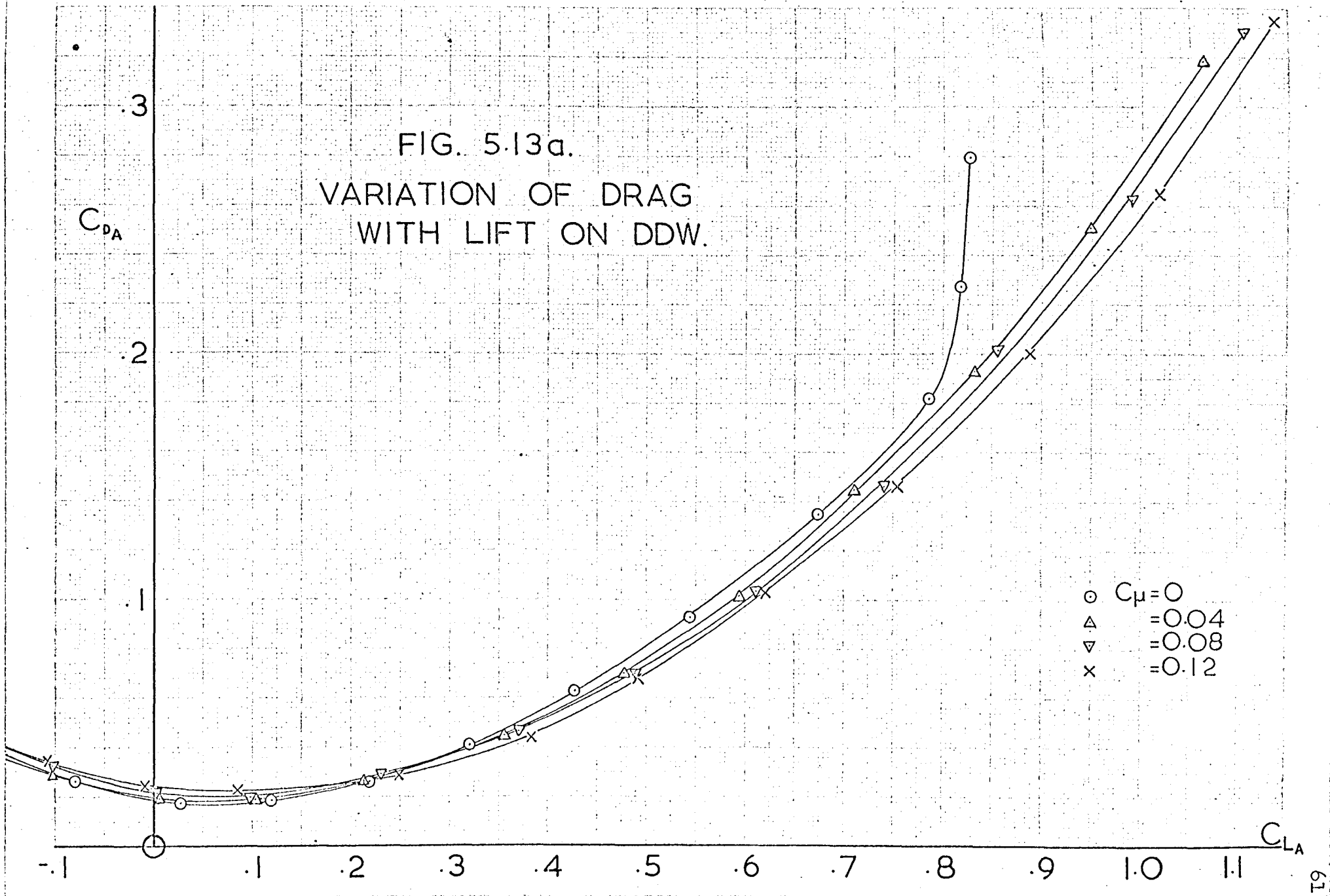
FIG. 5.13a.
VARIATION OF DRAG
WITH LIFT ON DDW.
C_{D_A}
.3
.2
.1
C_{L_A}
-.1
.1
.2
.3
.4
.5
.6
.7
.8
.9
1.0
1.1
$C_\mu = 0$
$= 0.04$
$= 0.08$
$= 0.12$

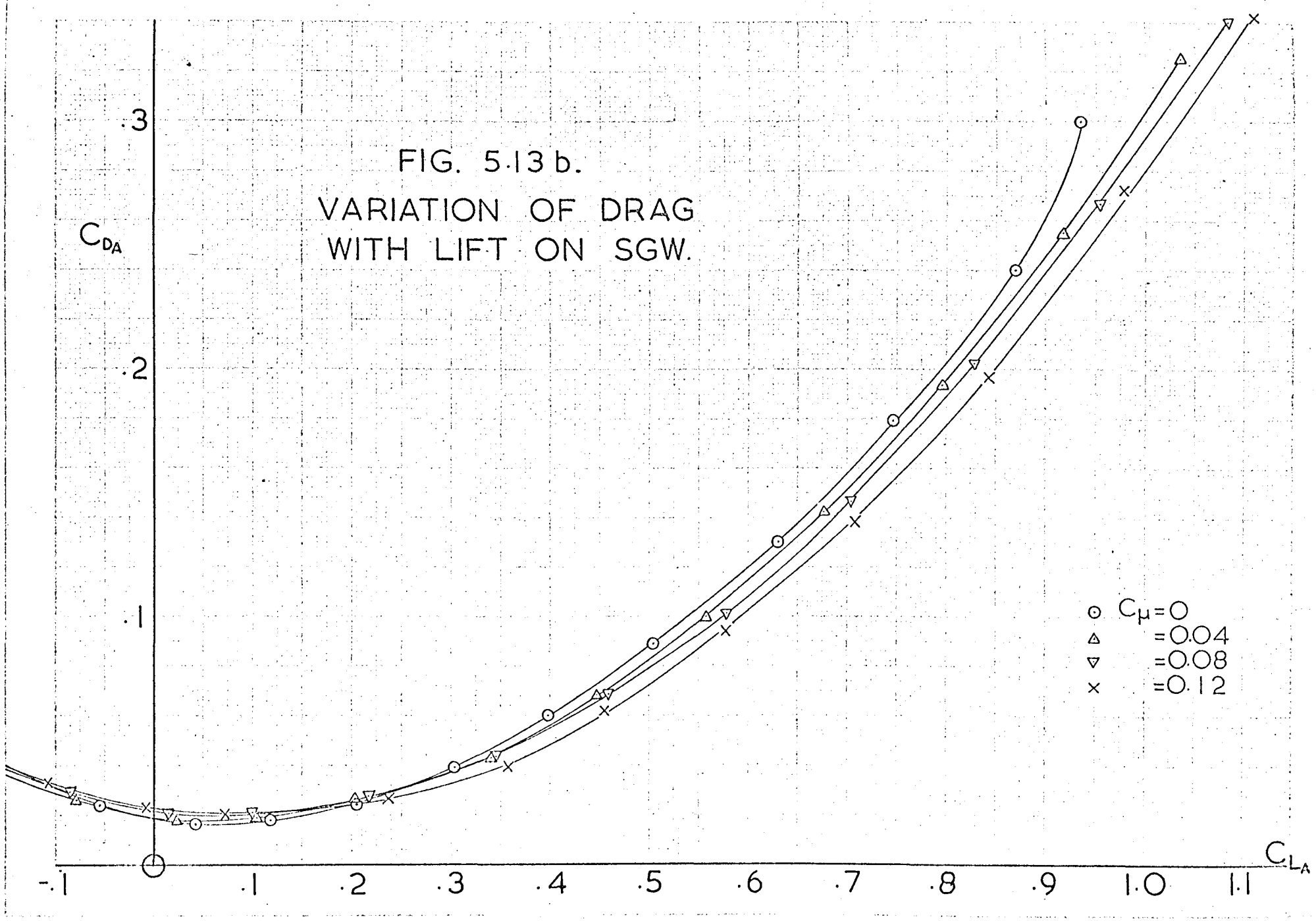
FIG. 5.13 b.
VARIATION OF DRAG
WITH LIFT ON SGW.
C_{D_A}
.3
.2
.1
C_{L_A}
-.1
.1
.2
.3
.4
.5
.6
.7
.8
.9
1.0
1.1
$C_\mu = 0$
$= 0.04$
$= 0.08$
$= 0.12$

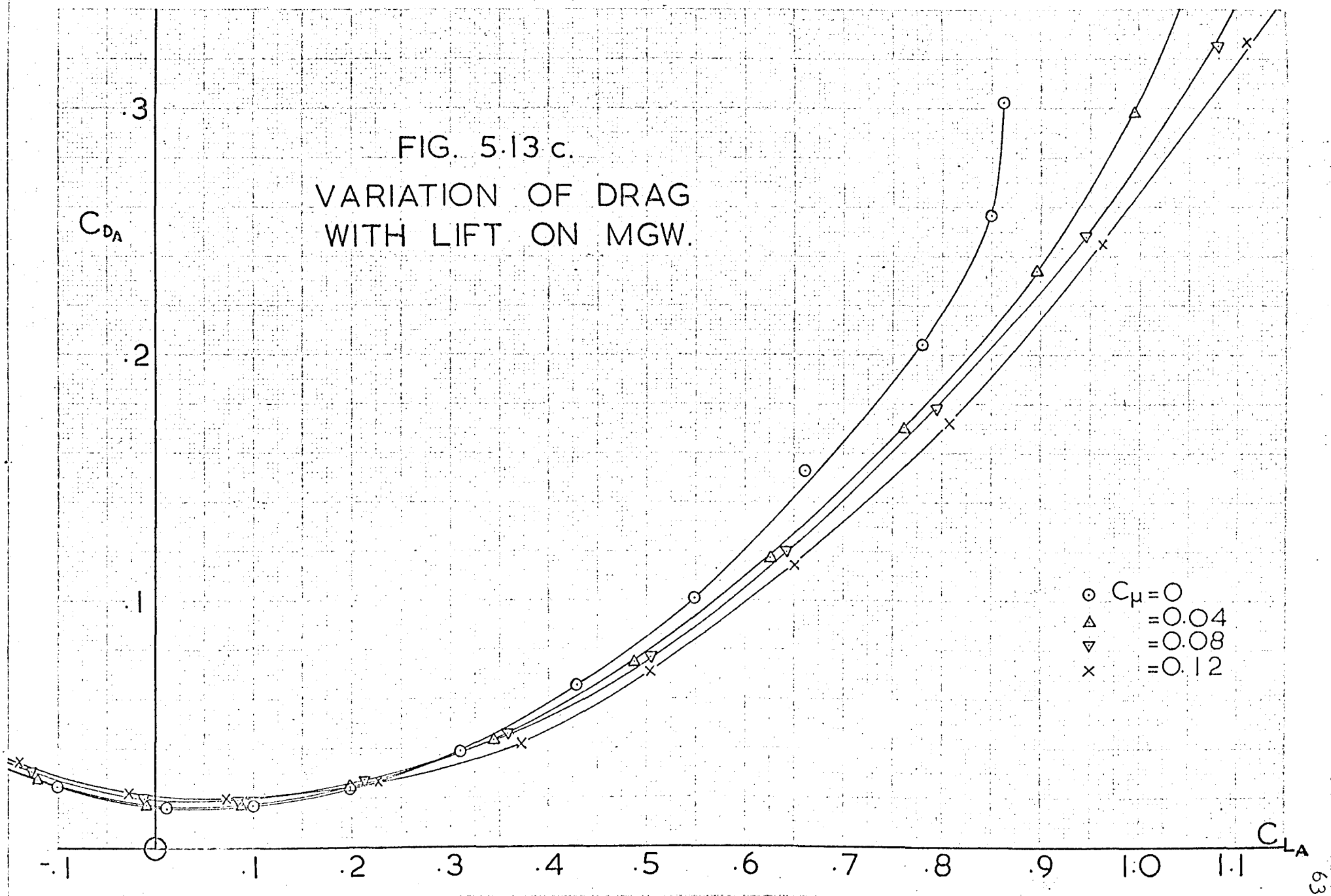
FIG. 5.13 c.
VARIATION OF DRAG WITH LIFT ON MGW.
C_{D_A}
.3
.2
.1
C_{L_A}
-.1
.1
.2
.3
.4
.5
.6
.7
.8
.9
1.0
1.1
$C_\mu = 0$
$= 0.04$
$= 0.08$
$= 0.12$

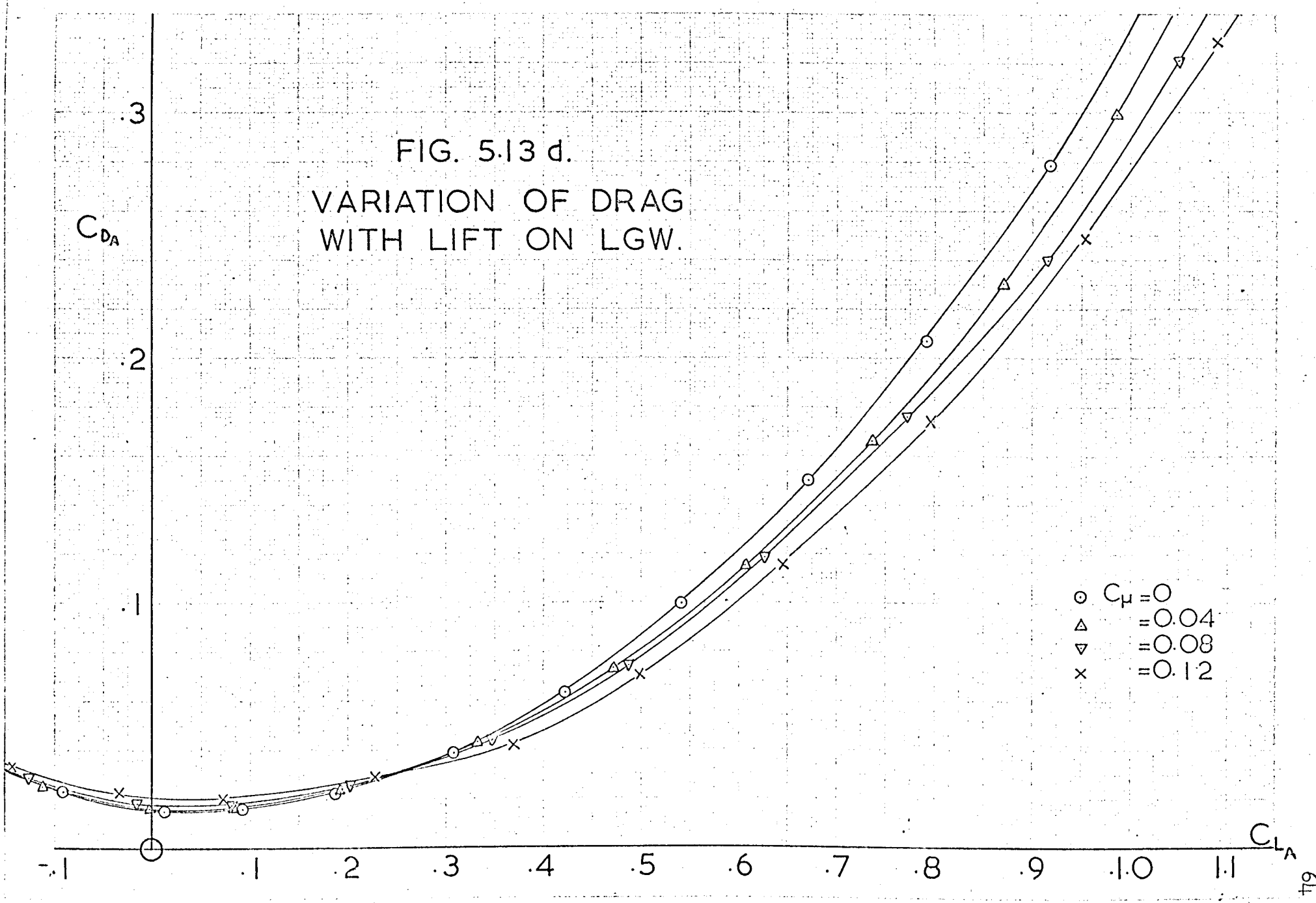
FIG. 5.13 d.
VARIATION OF DRAG WITH LIFT ON LGW.
C_{D_A}
.3
.2
.1
C_{L_A}
-.1
.1
.2
.3
.4
.5
.6
.7
.8
.9
1.0
1.1
C_μ = 0
= 0.04
= 0.08
= 0.12

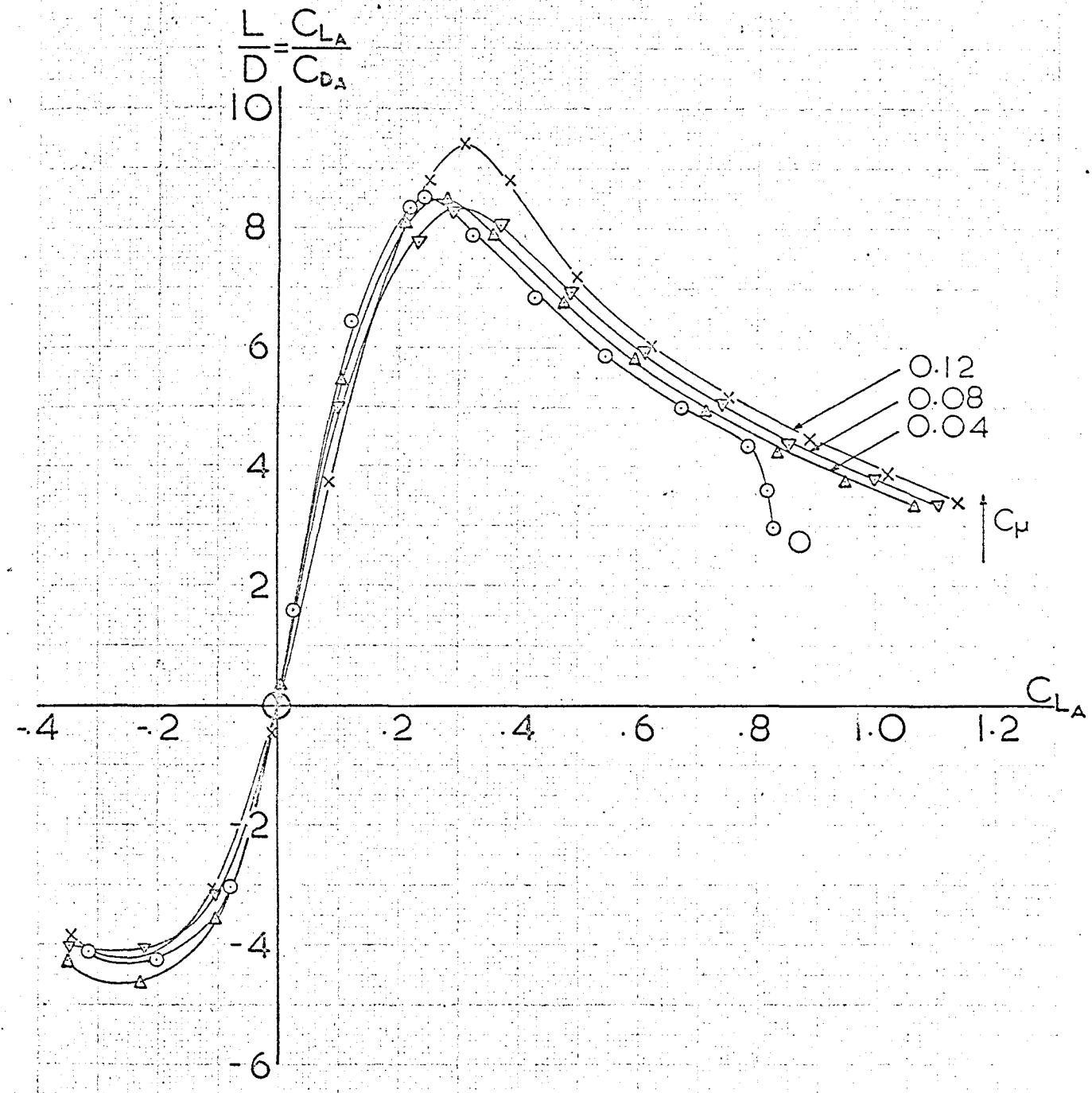

FIG. 5.14a. LIFT-DRAG RATIOS ON DDW.

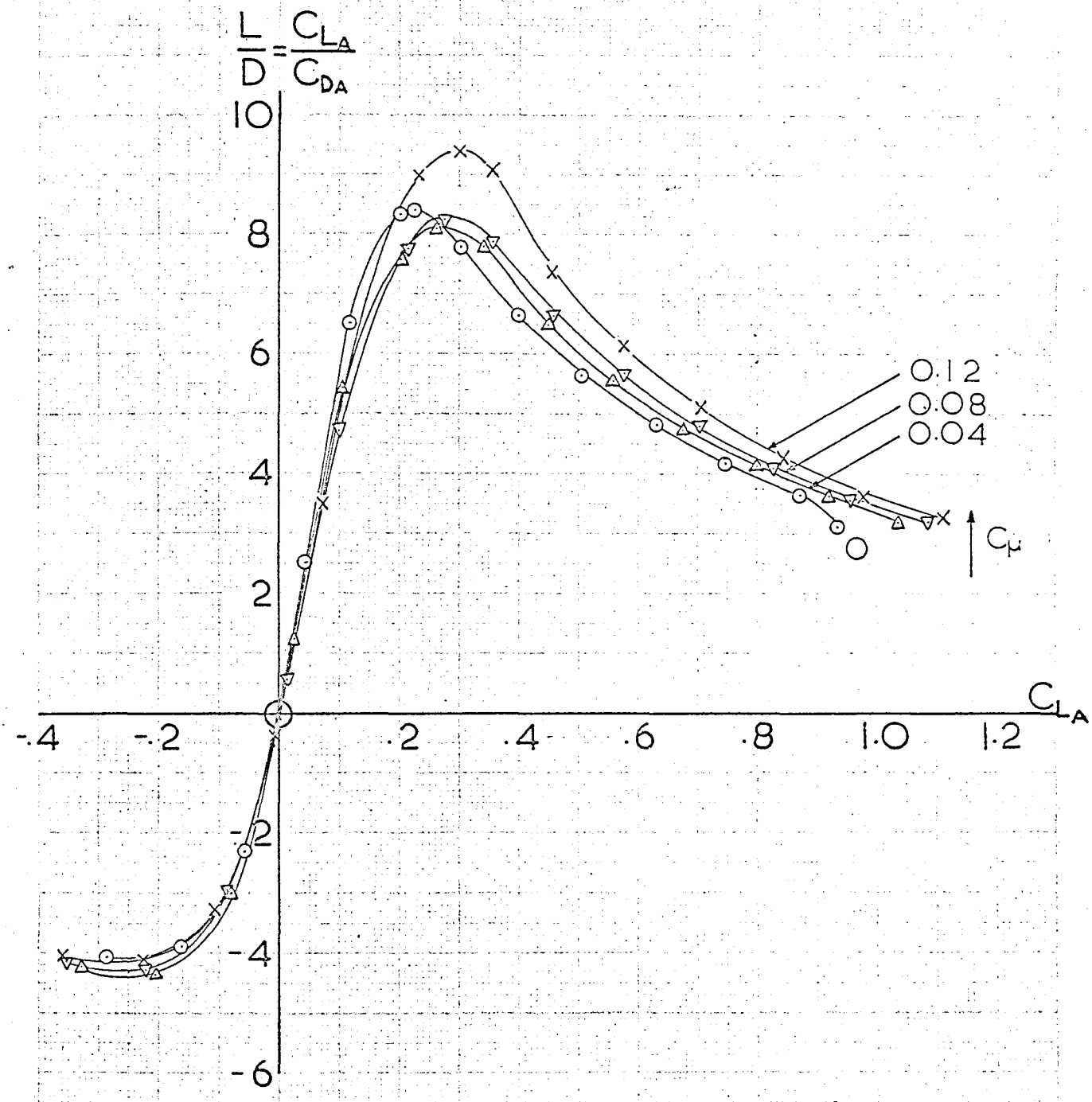

FIG. 5.14b. LIFT-DRAG RATIOS ON SGW.

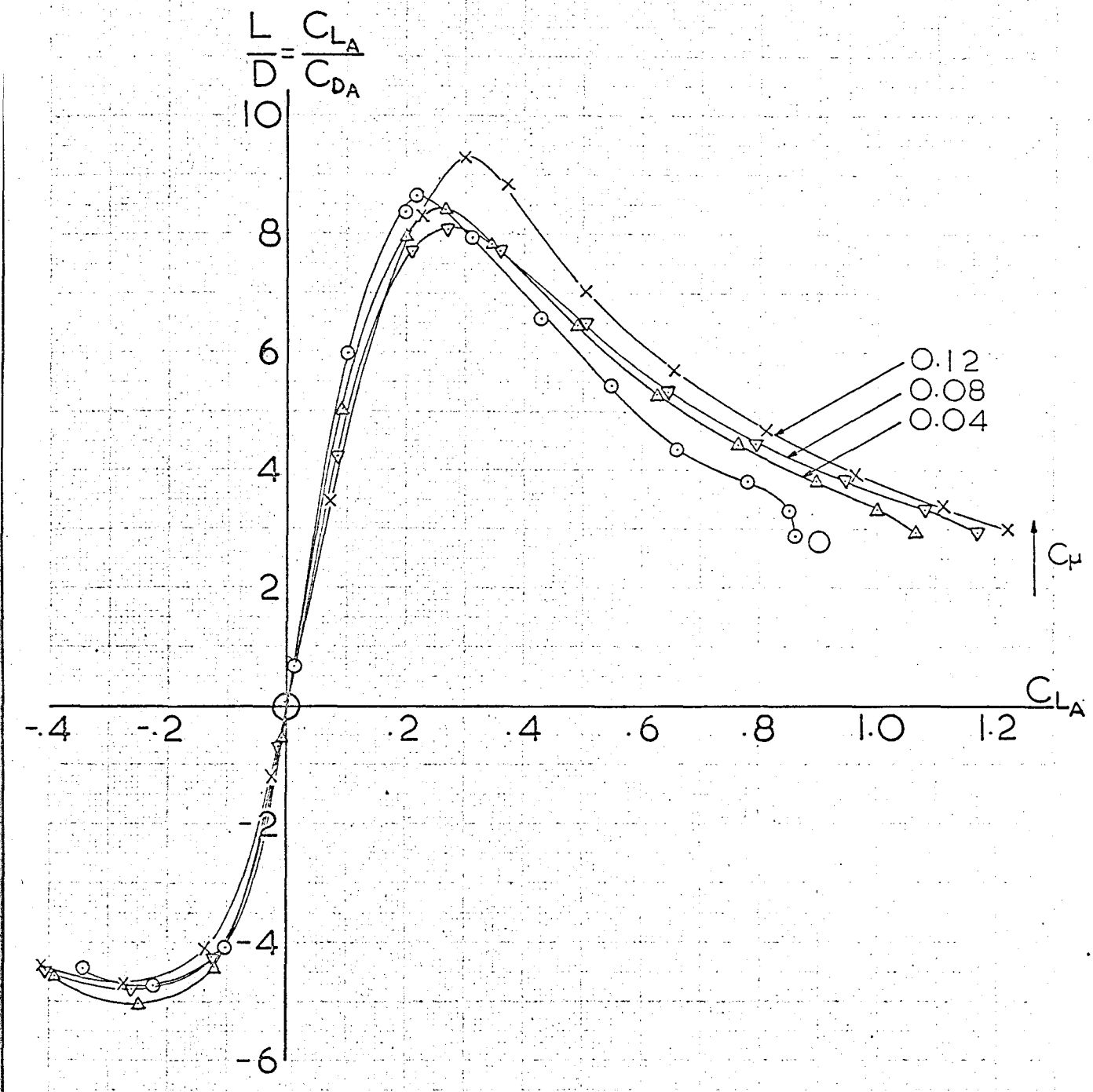

FIG. 5.14c. LIFT-DRAG RATIOS ON MGW.

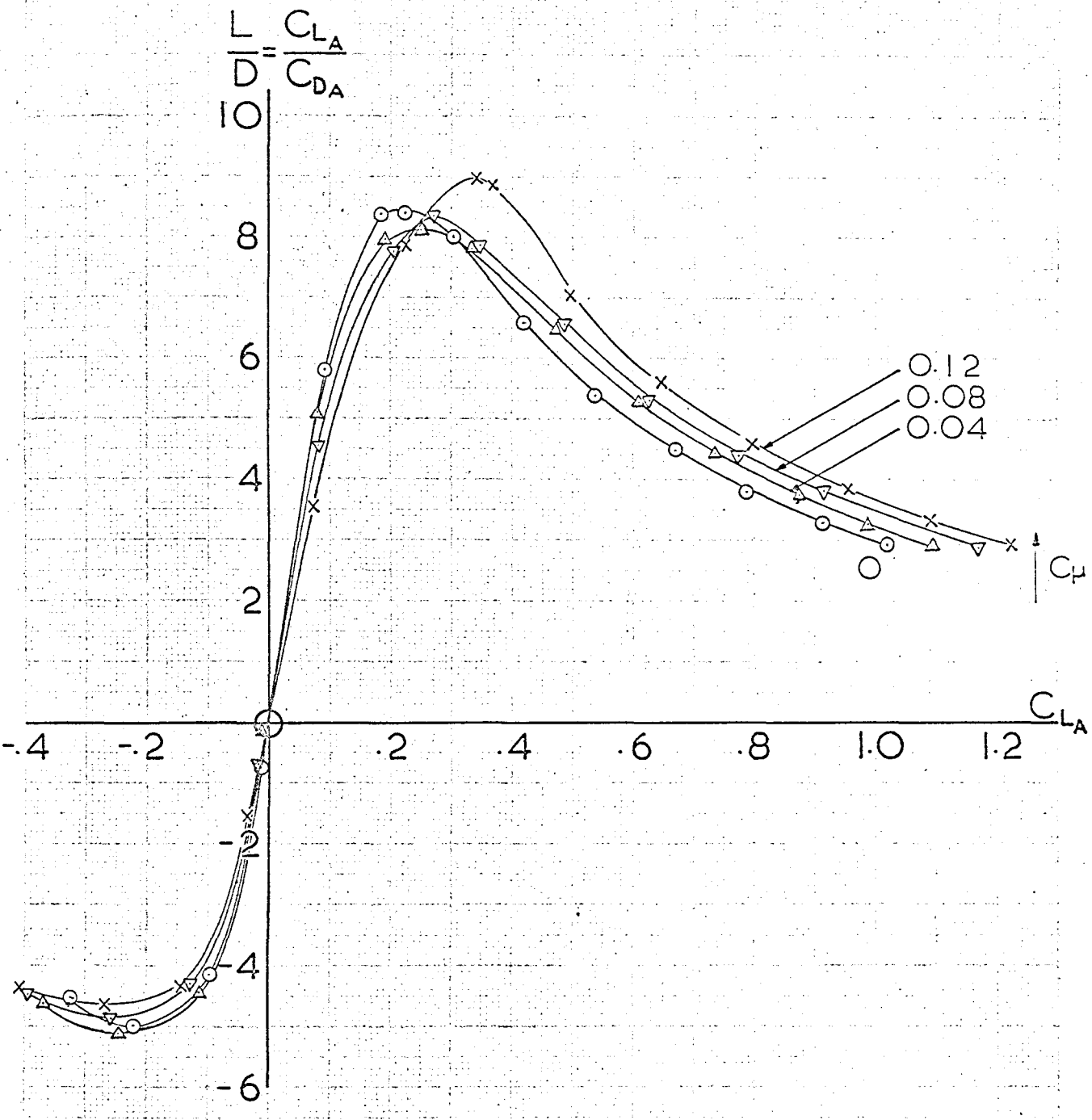

FIG. 5.14d. LIFT-DRAG RATIOS ON LGW.

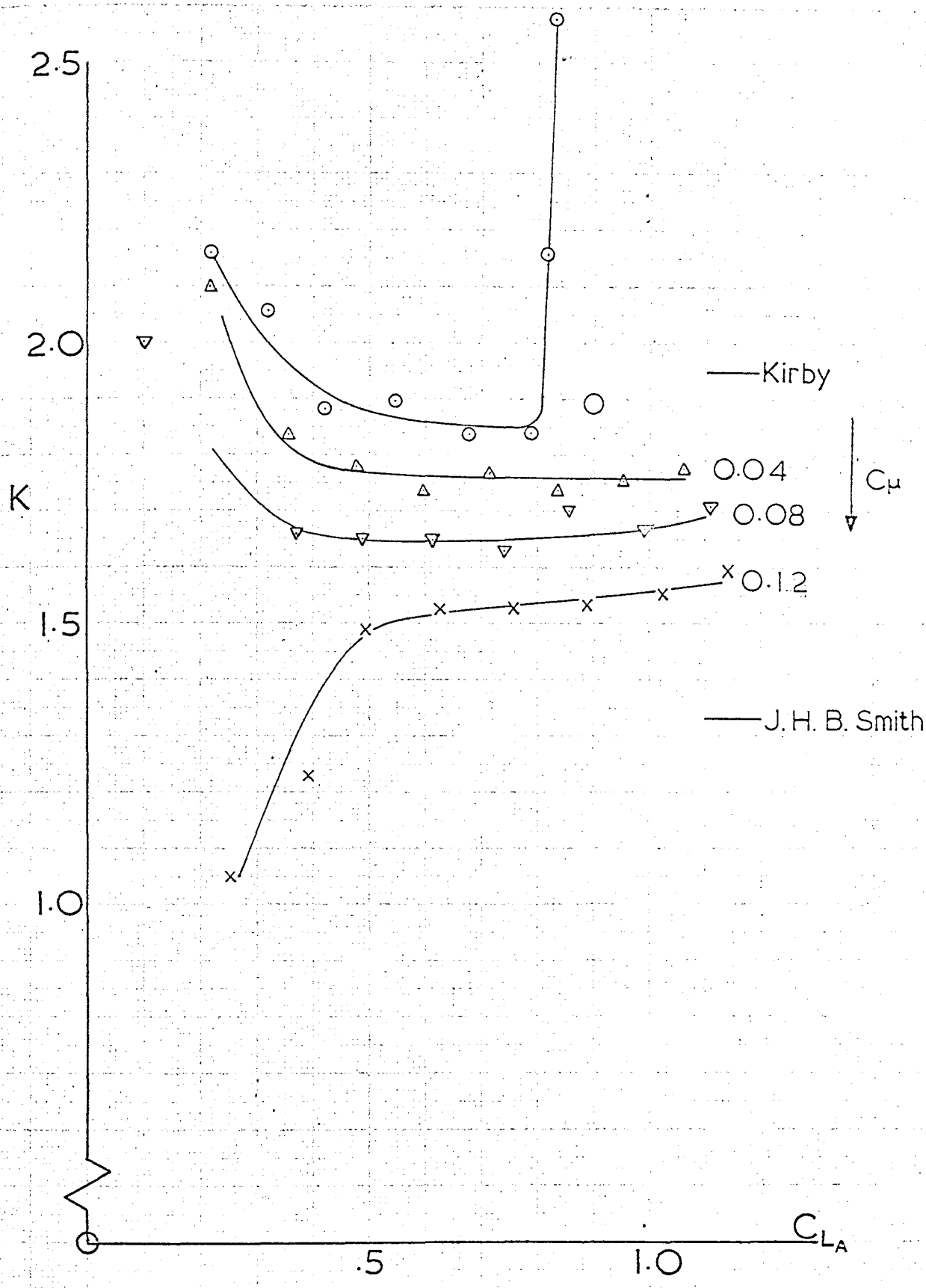

FIG. 5.15a. LIFT-DEPENDENT DRAG FACTOR, K, ON DDW.

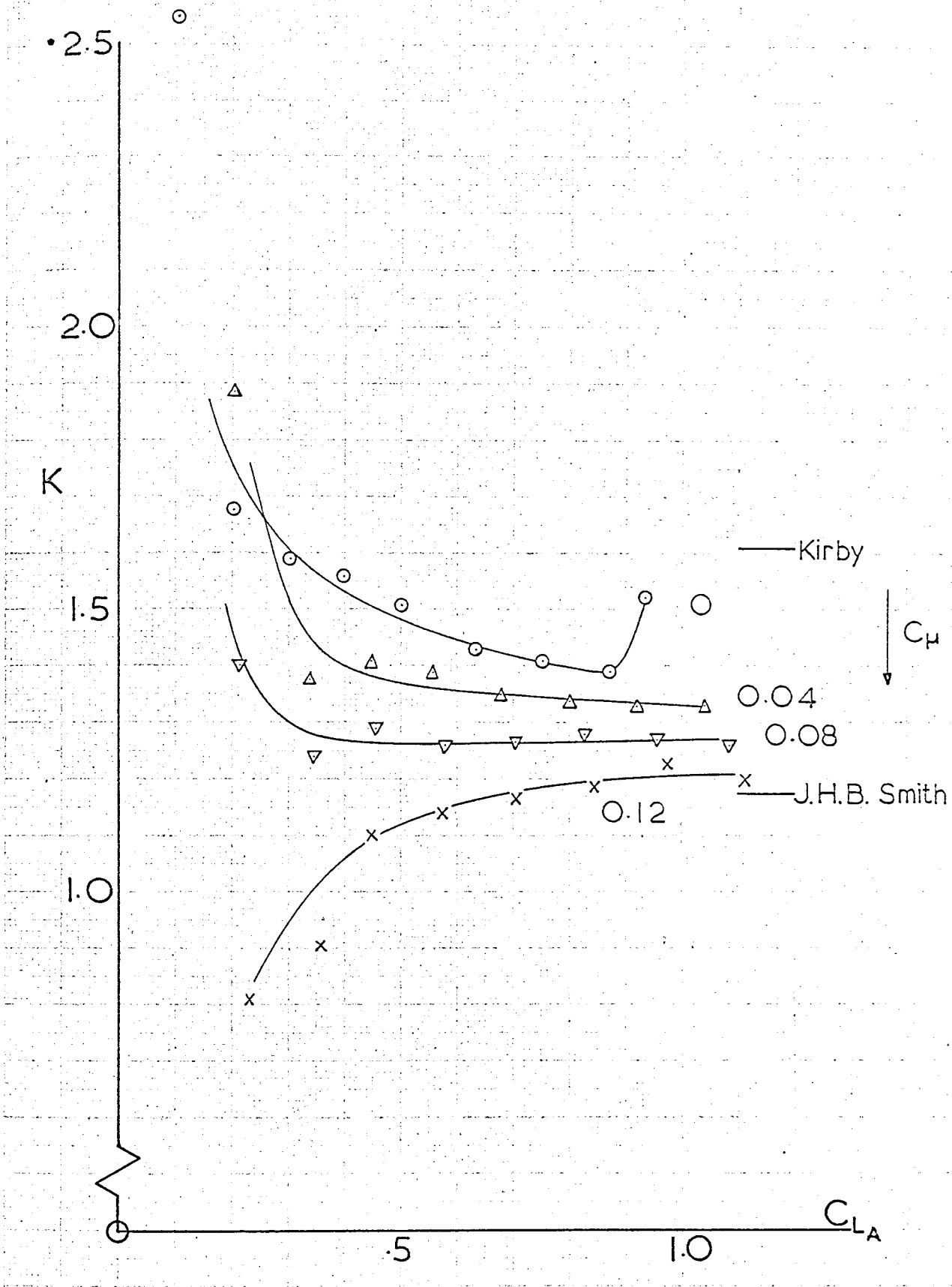

FIG. 5.15b. LIFT-DEPENDENT DRAG FACTOR, K, ON SGW.

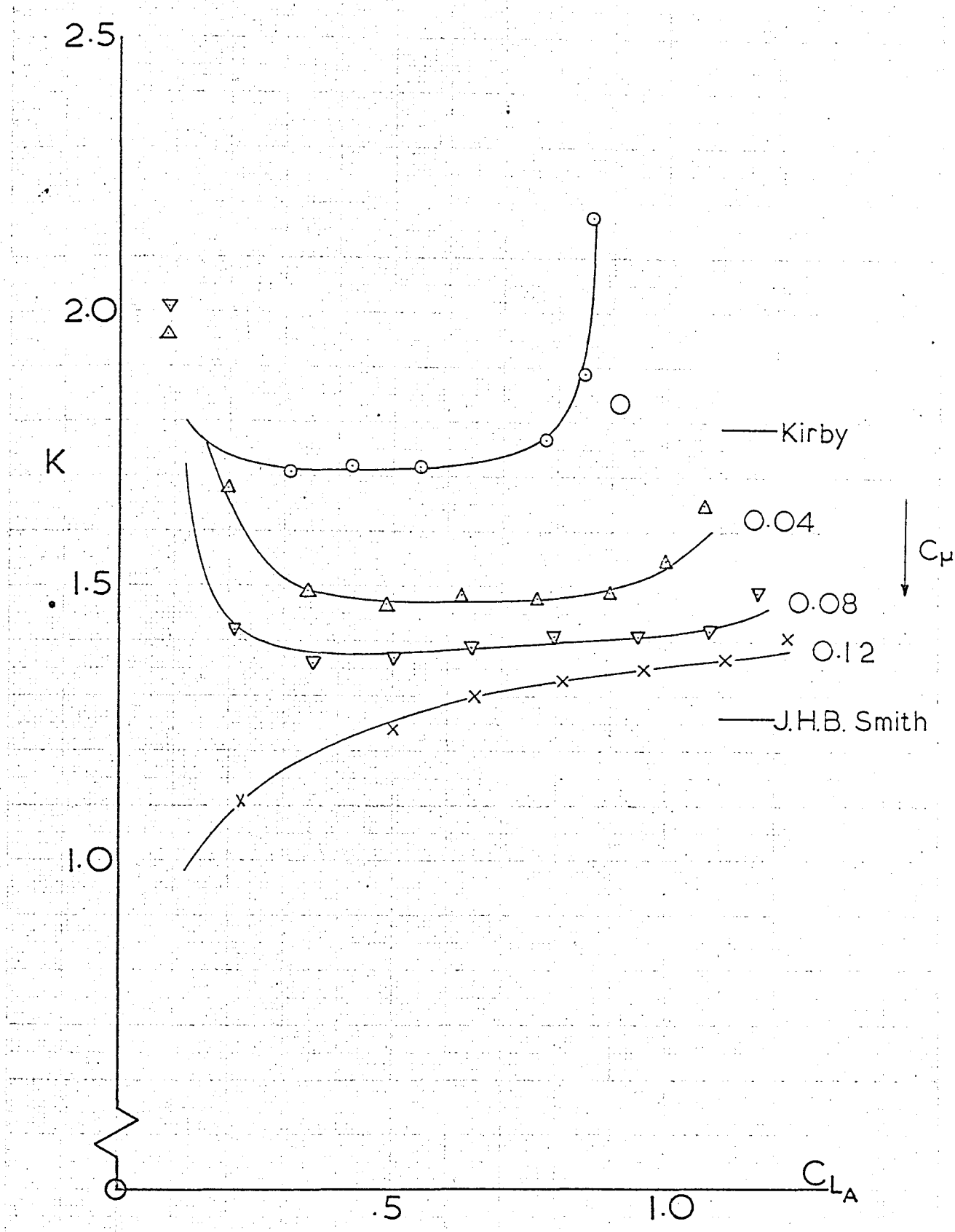

FIG. 5.15c. LIFT-DEPENDENT DRAG FACTOR, K, ON MGW.

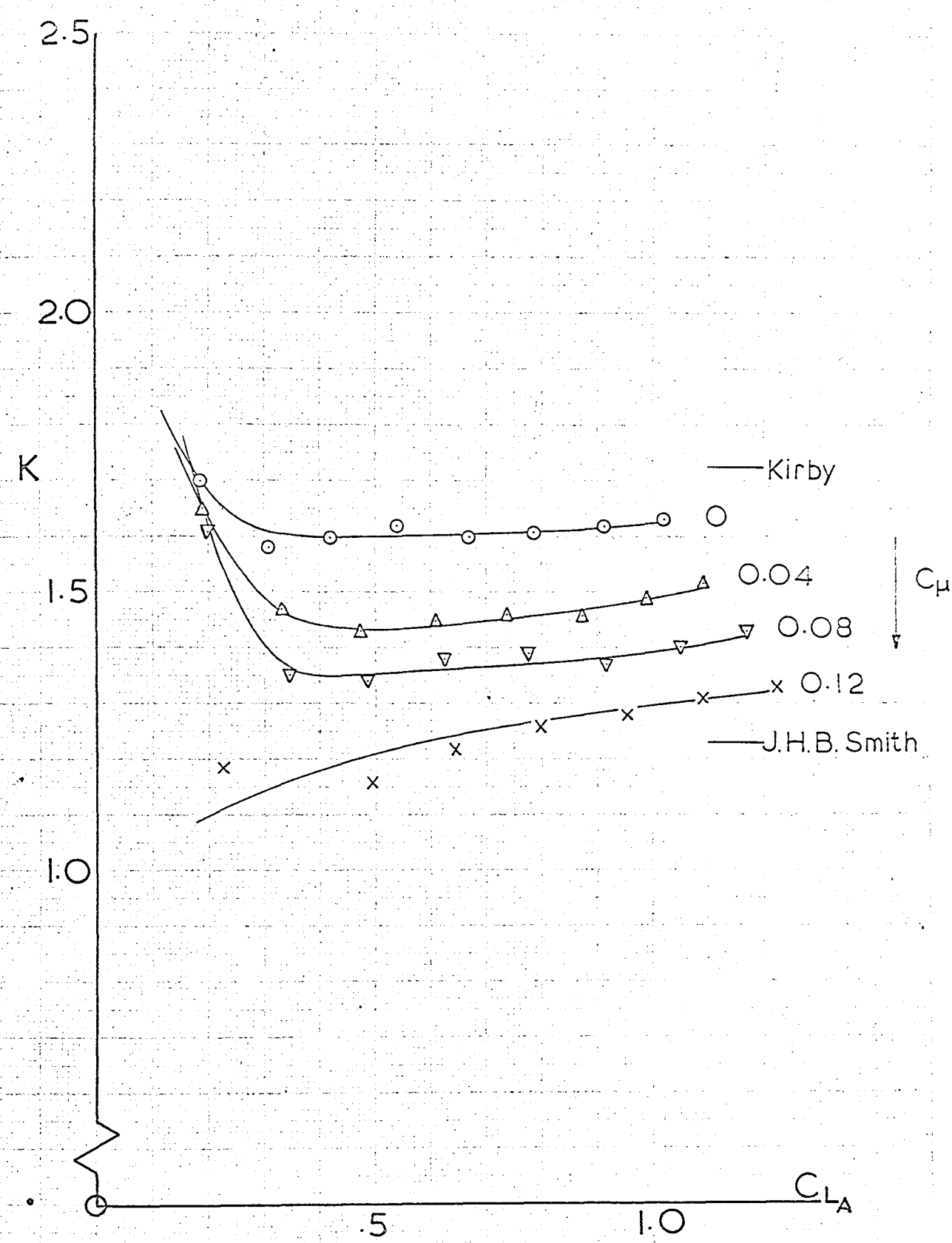

FIG. 5.15d. LIFT-DEPENDENT DRAG FACTOR, K, ON LGW.

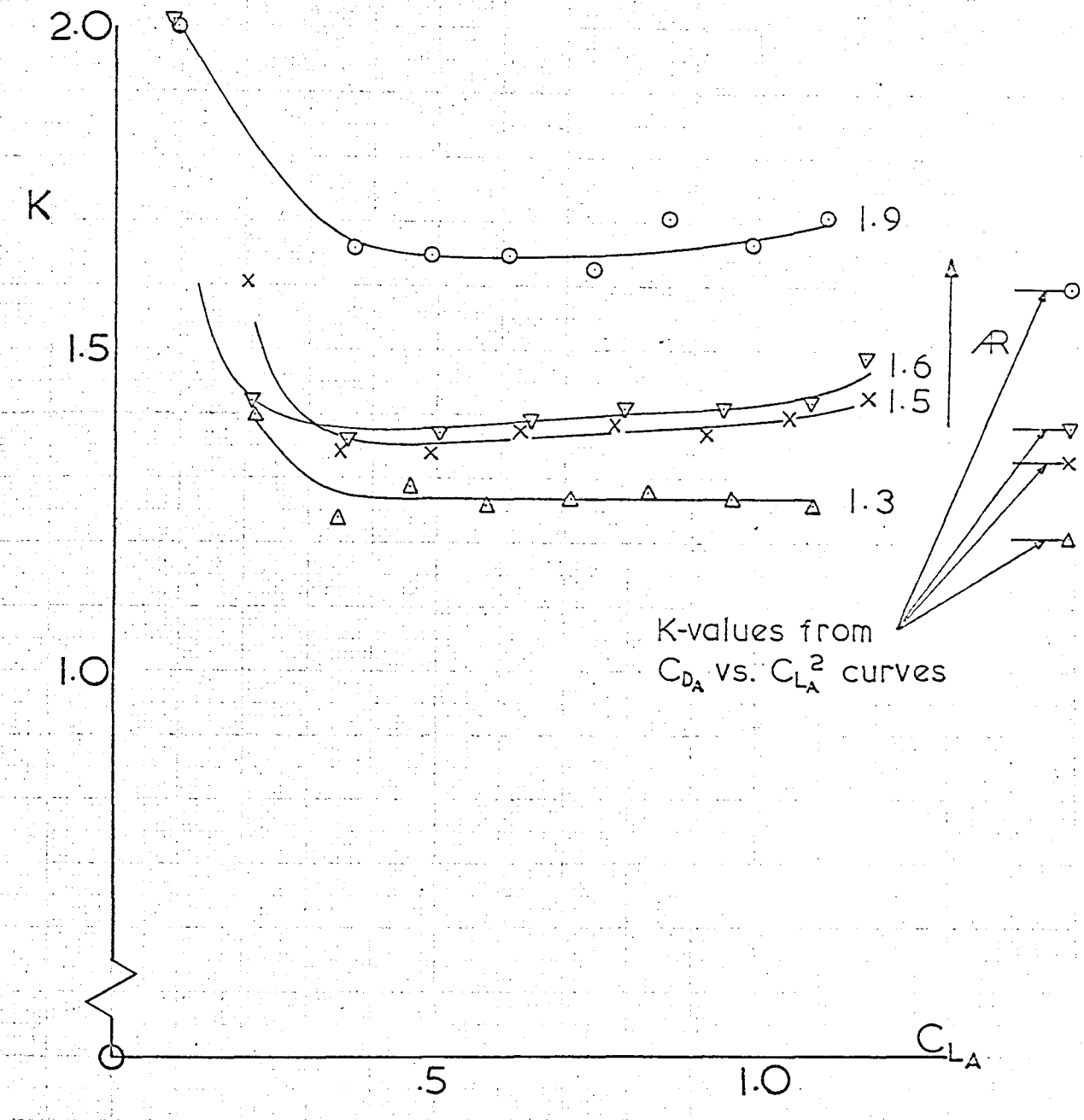

FIG. 5.16. VARIATION OF LIFT-DEPENDENT DRAG FACTOR, K, WITH ASPECT RATIO AT $C_\mu = 0.08$.

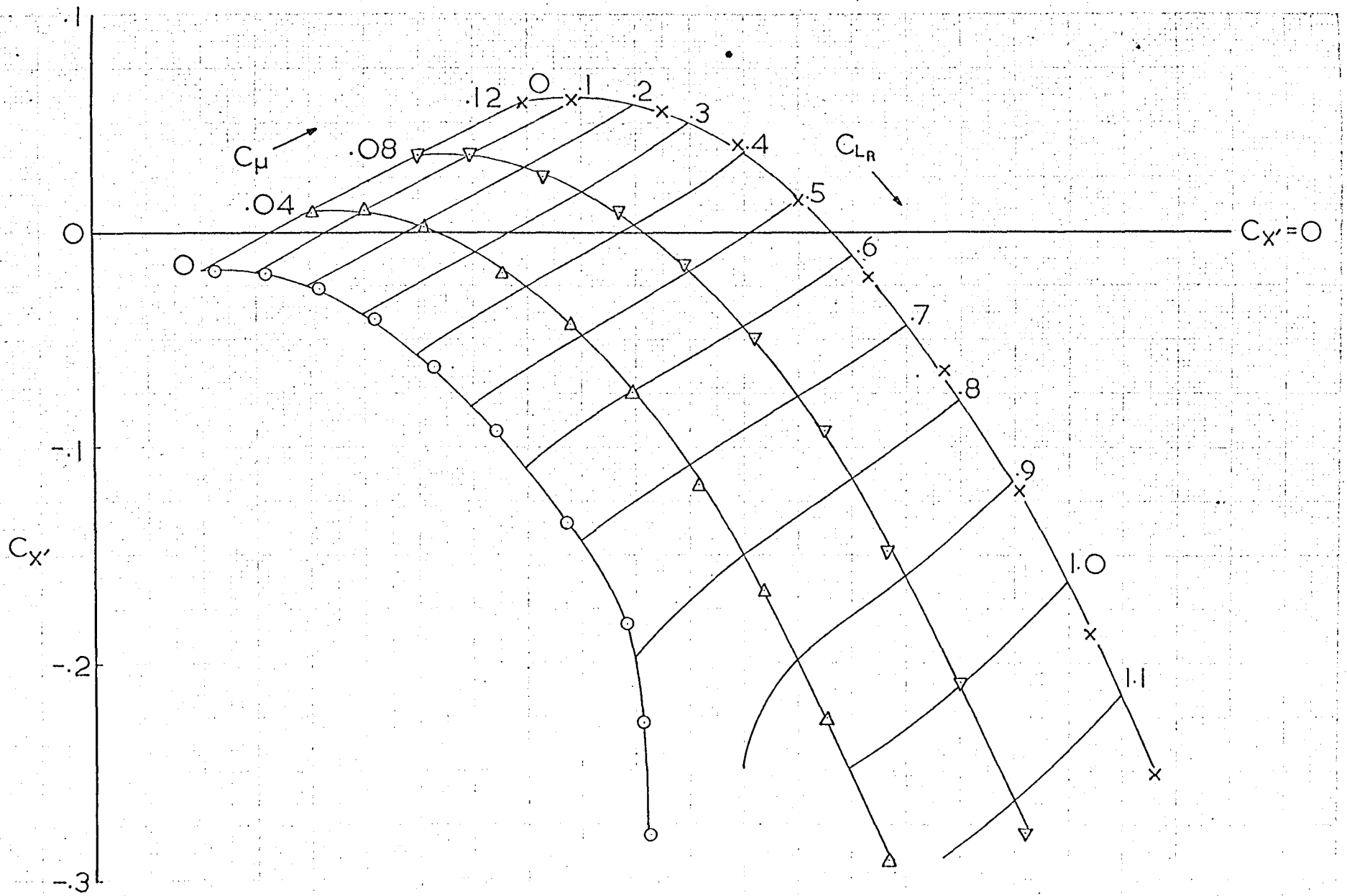

FIG. 5.17a. $C_{X'}$ CARPET FOR DDW.

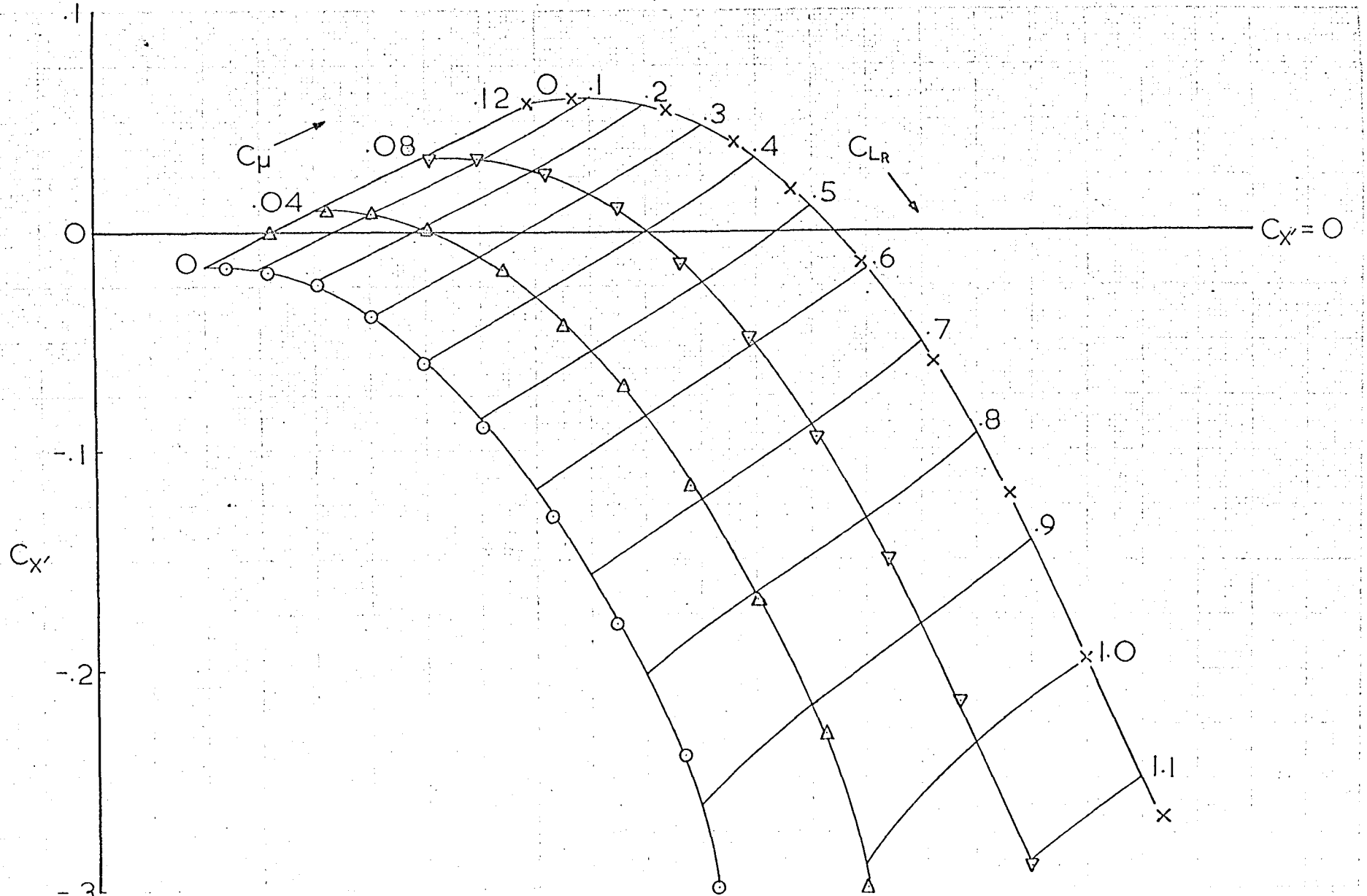

FIG. 5.17 b. $C_{X'}$ CARPET FOR SGW.

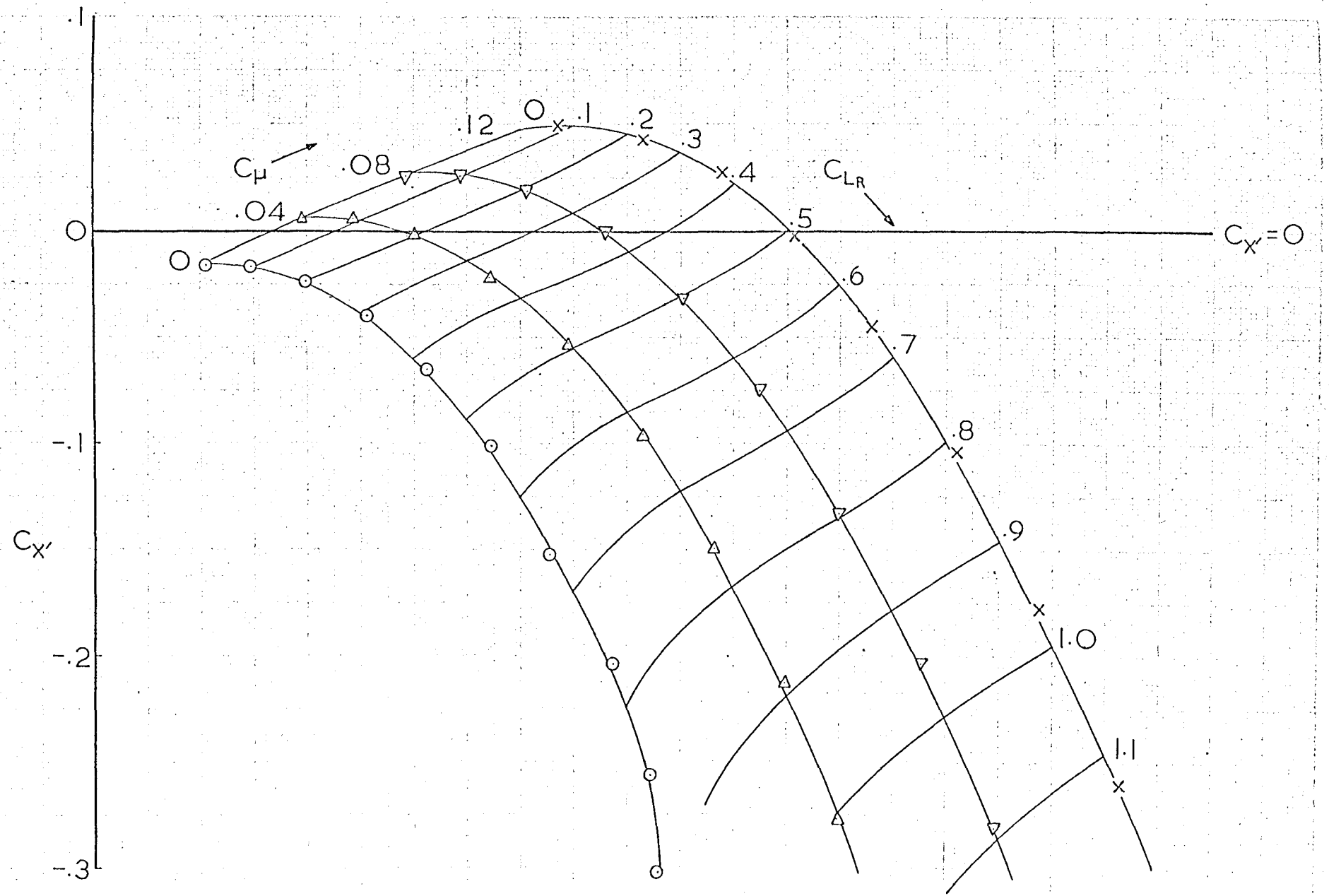

FIG. 5.17c. $C_{X'}$ CARPET FOR MGW.

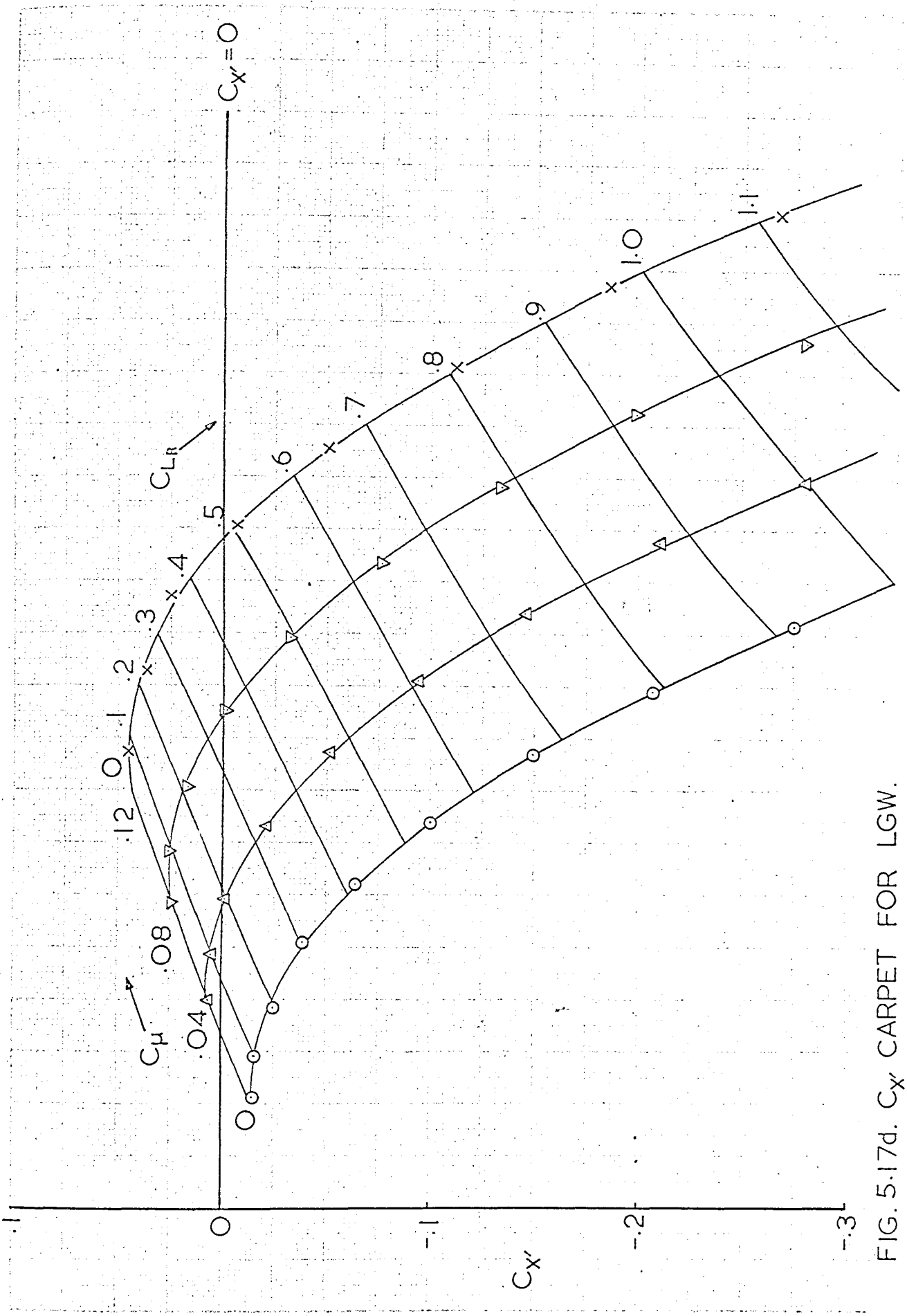

FIG. 5.17d. $C_{X'}$ CARPET FOR LGW.

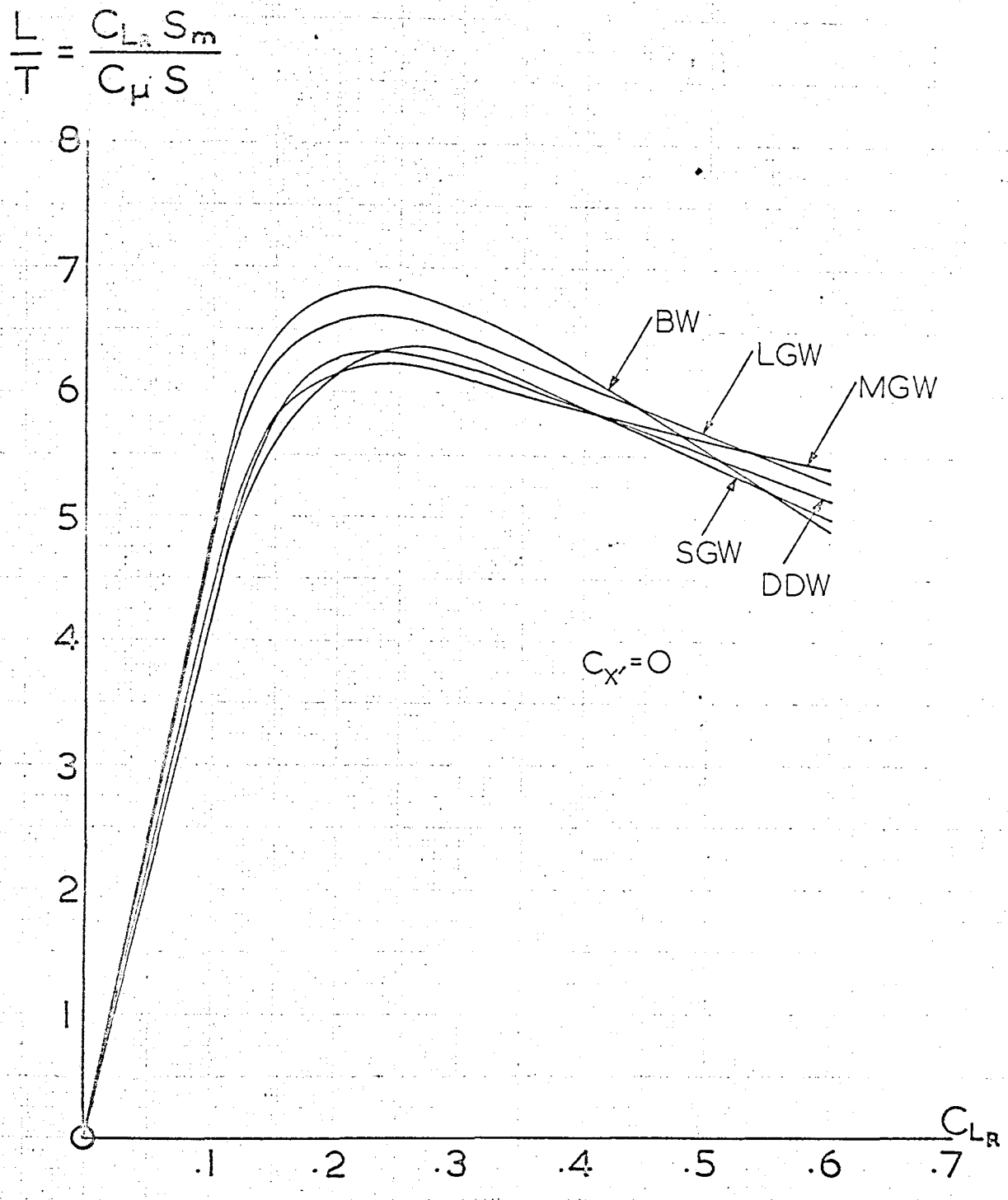

FIG. 5.18. LIFT-THRUST RATIOS.

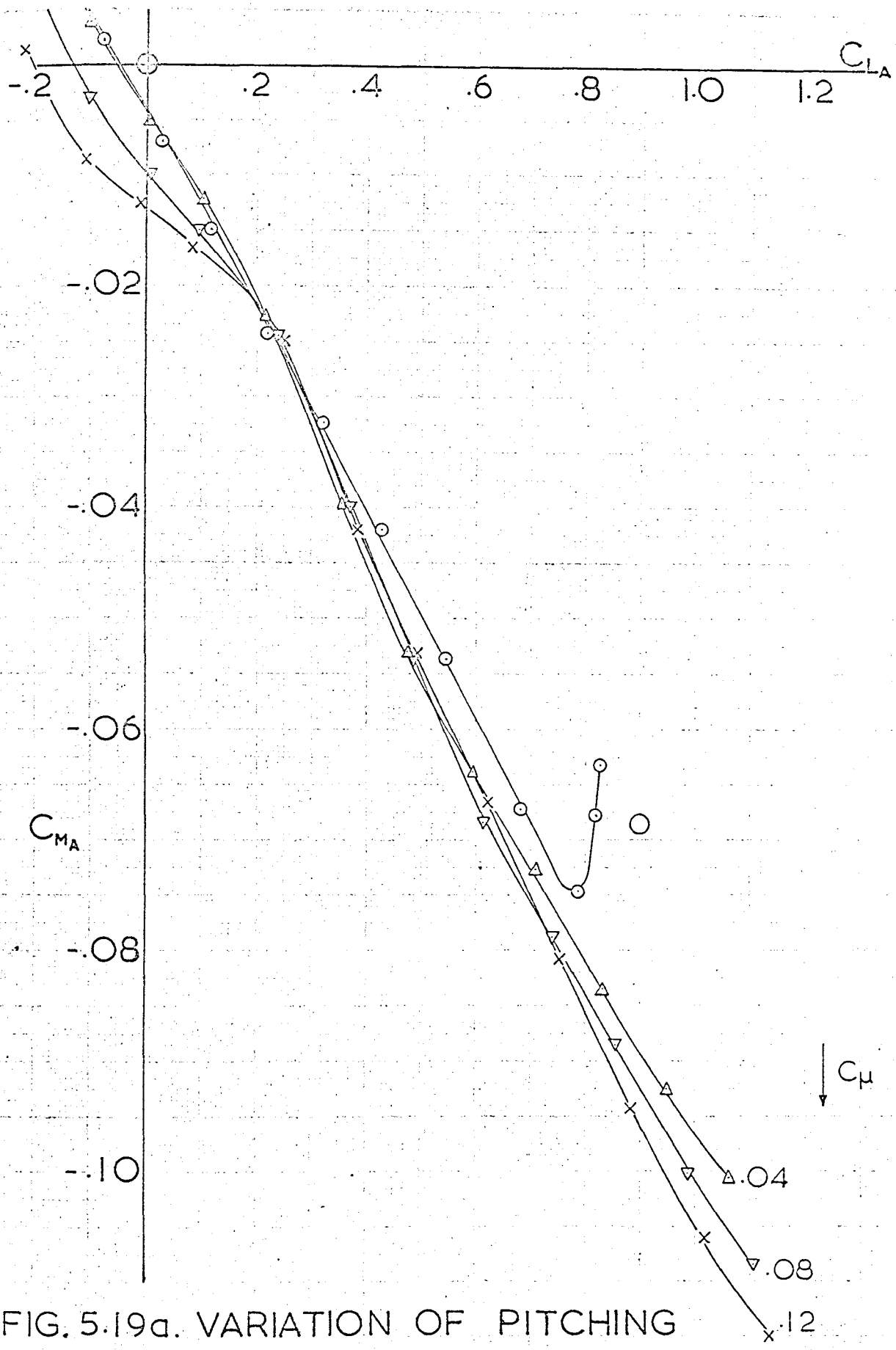

FIG. 5.19a. VARIATION OF PITCHING MOMENT WITH LIFT ON DDW.

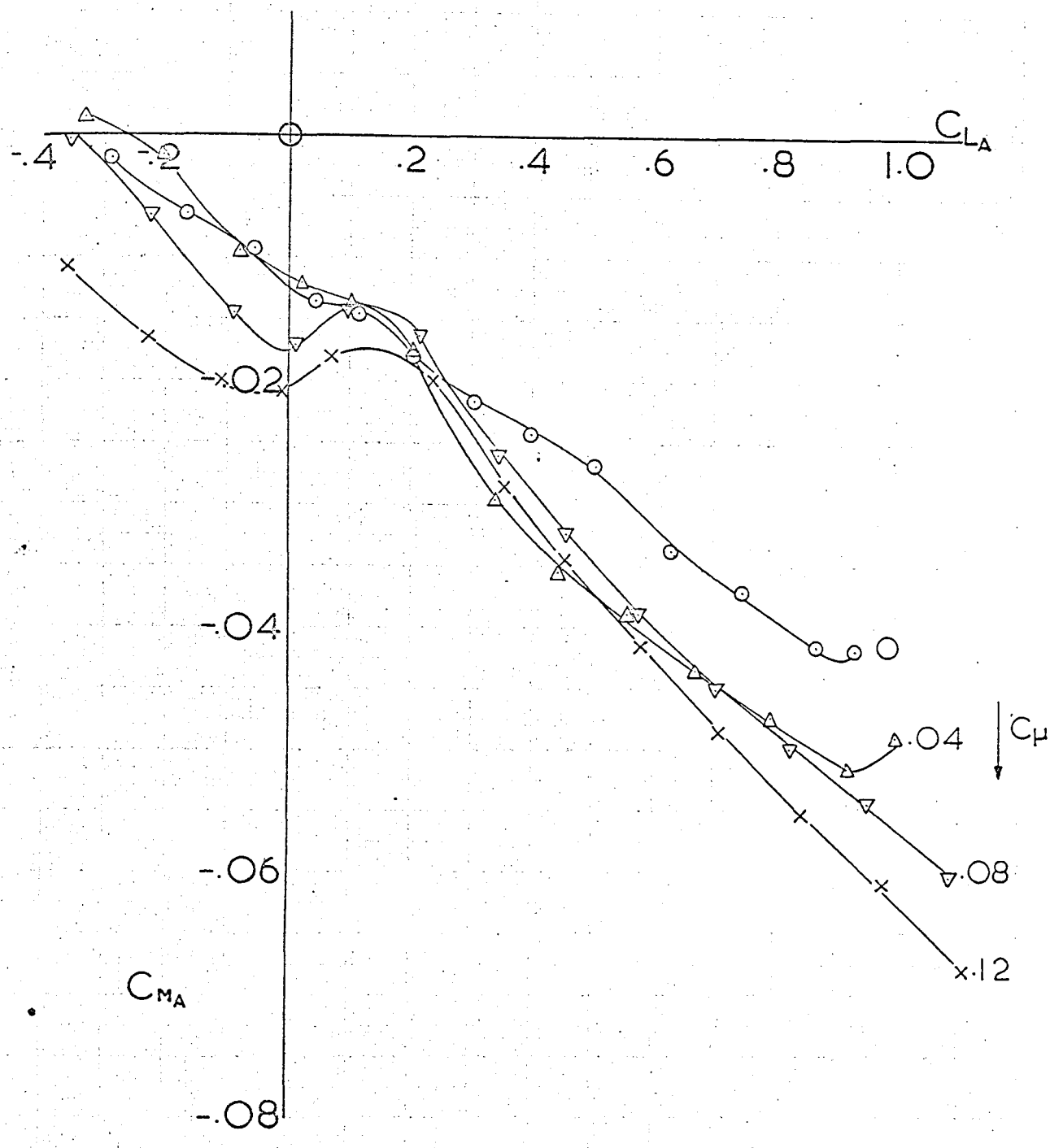

FIG. 5.19b. VARIATION OF PITCHING MOMENT WITH LIFT ON SGW.

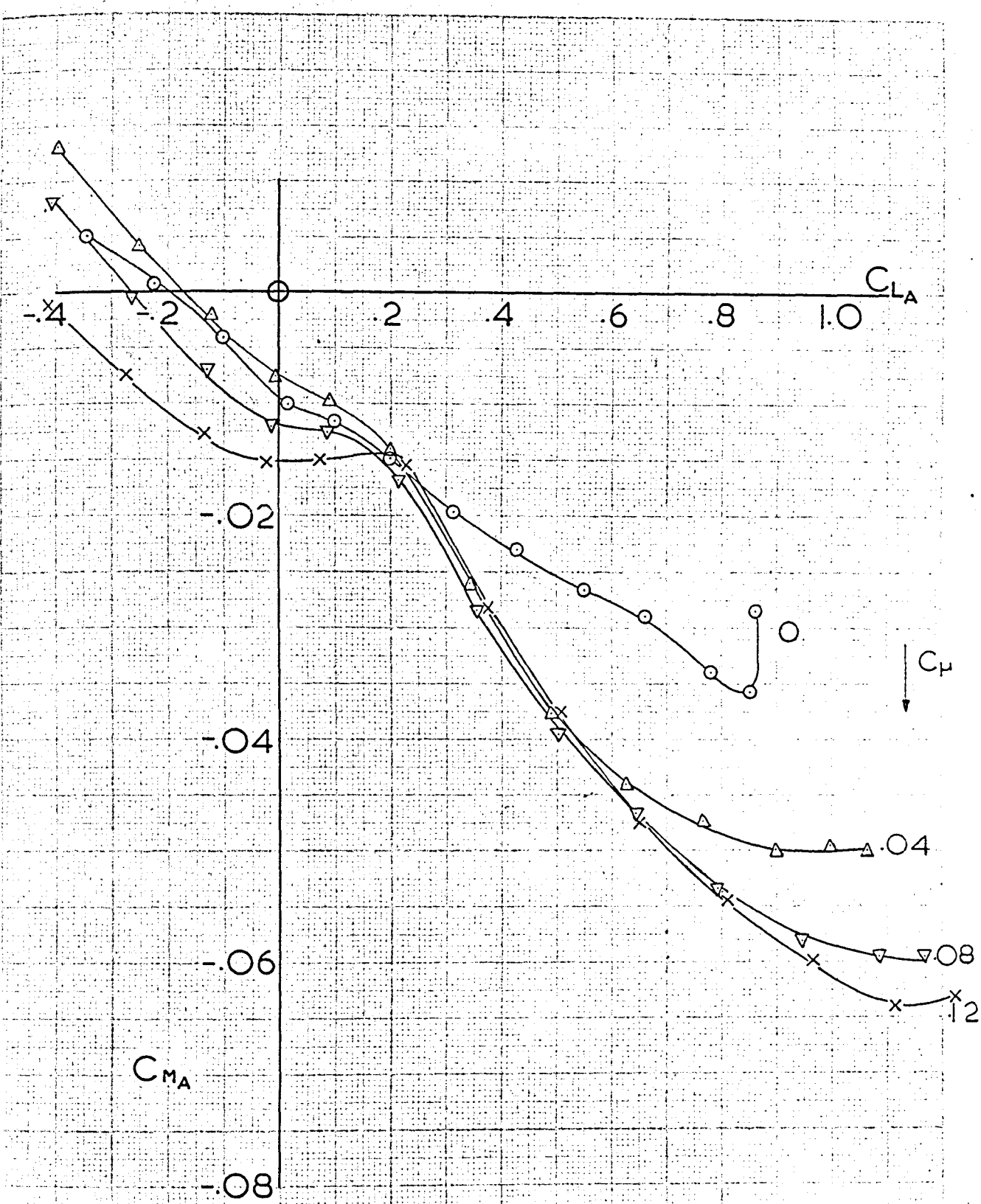

FIG. 5.19c. VARIATION OF PITCHING MOMENT WITH LIFT ON MGW.

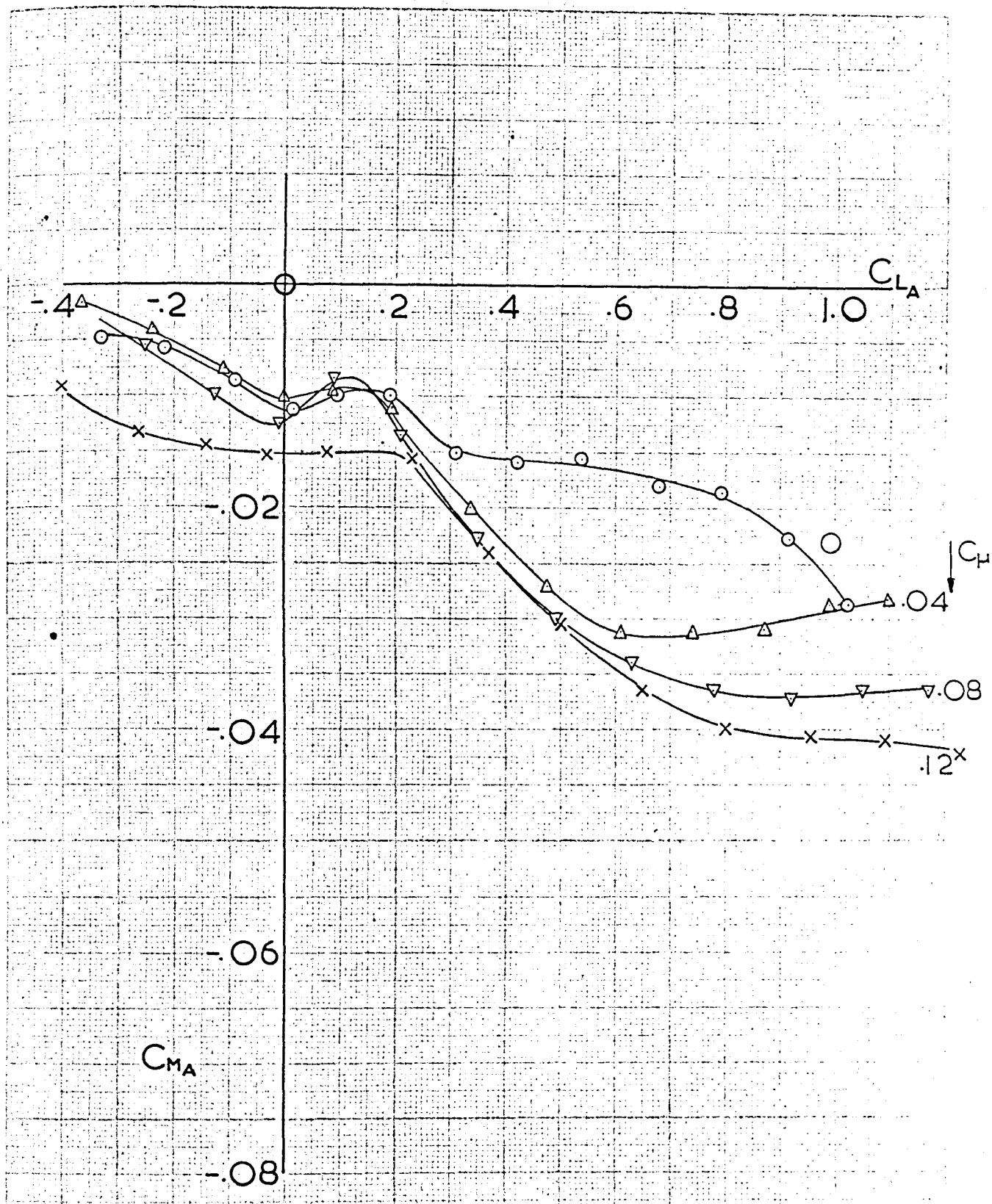

FIG. 5.19d. VARIATION OF PITCHING MOMENT WITH LIFT ON LGW.

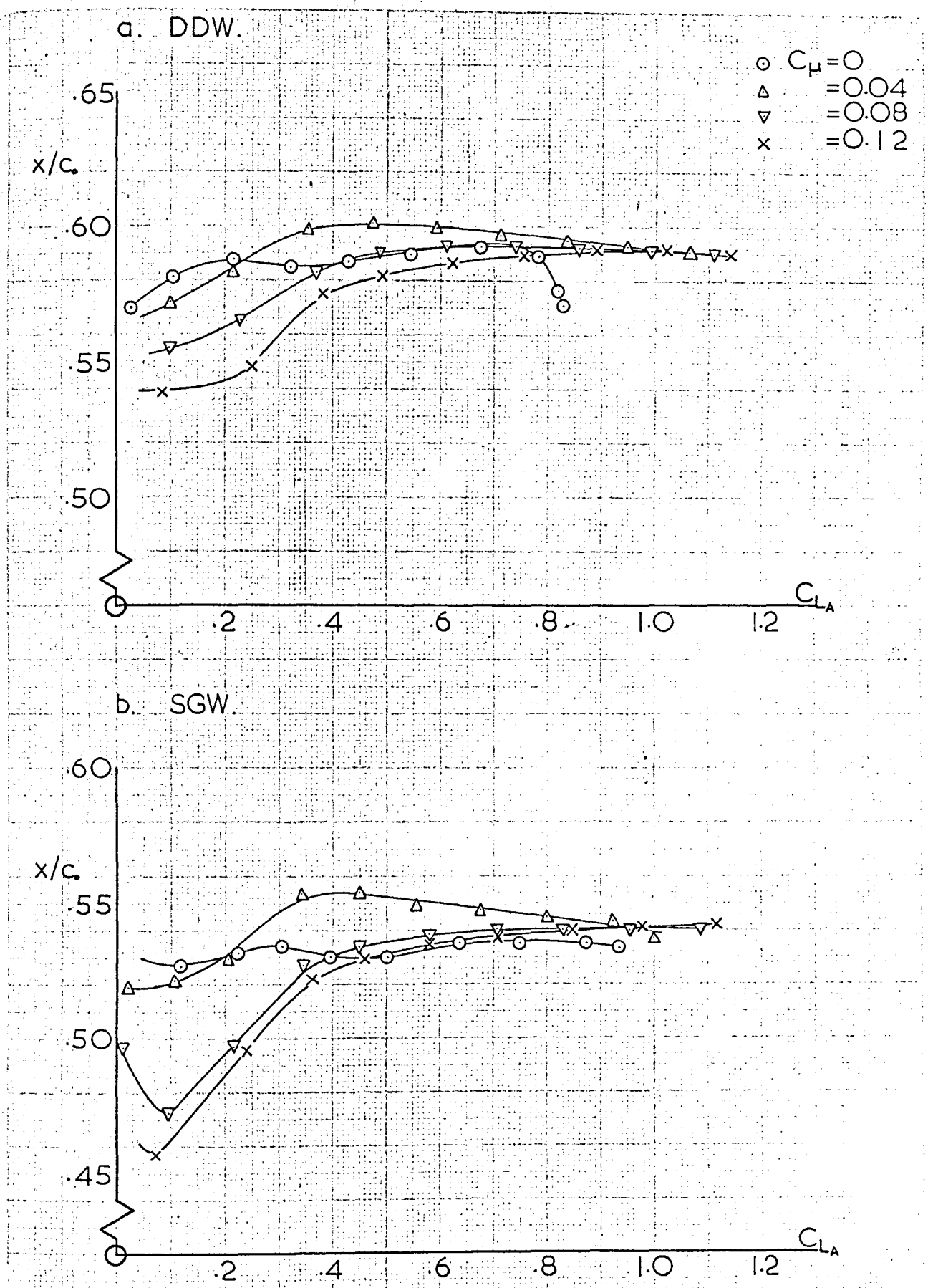

FIG. 5.20. AERODYNAMIC CENTER POSITIONS.

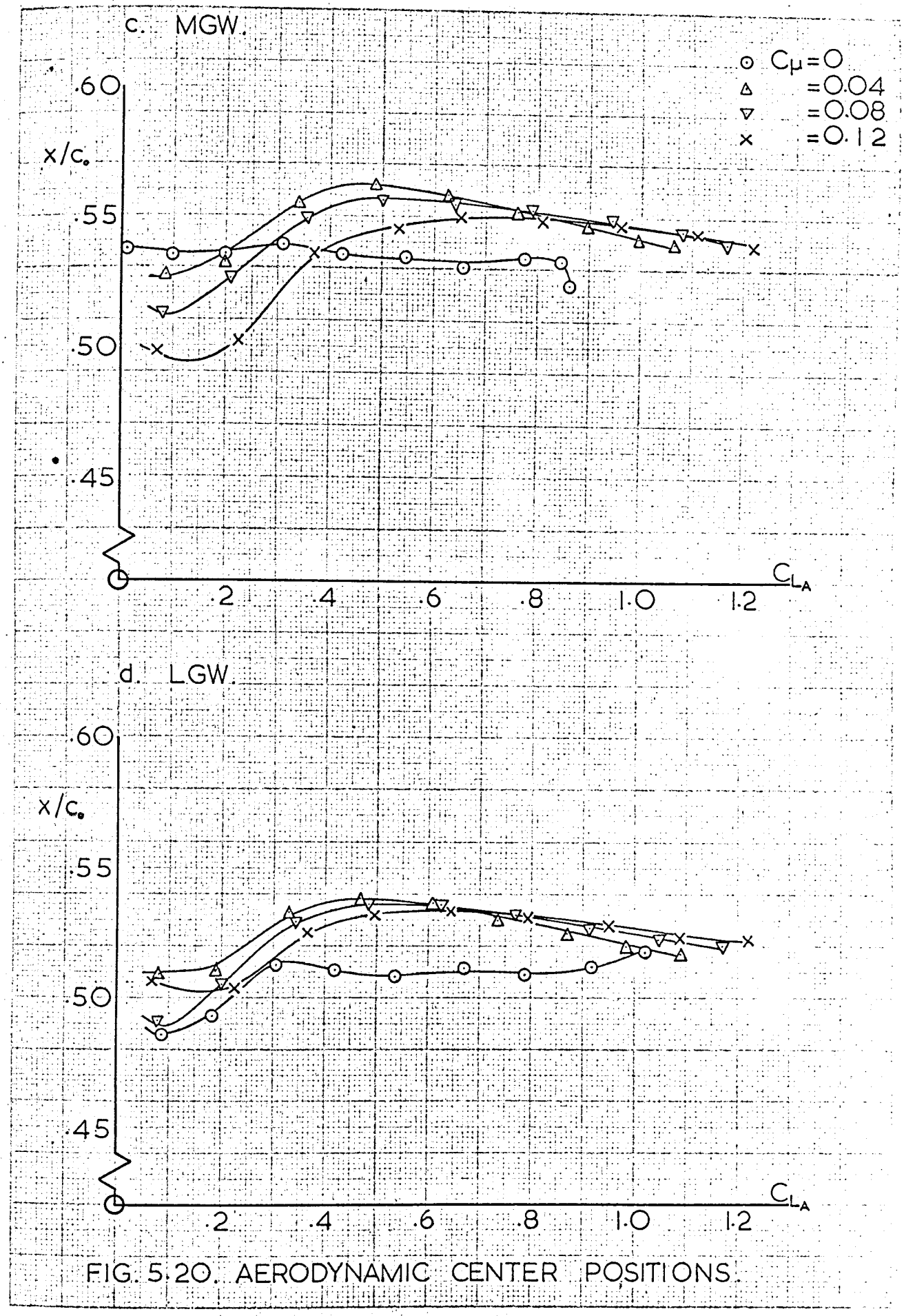

FIG. 5.20. AERODYNAMIC CENTER POSITIONS.

APPENDIX A
DIMENSIONAL ANALYSIS

The general equation for a force, F, on a body in a low-speed flow is dependent upon several variables. Such an equation can be written in terms of these variables, such as:

$$F \sim \rho^a \, l^b \, V_o^c \, \mu^d \tag{1}$$

where l is a characteristic length of the body
μ is the coefficient of viscosity
a, b, c, d, are unknown coefficients

When apex blowing is introduced into the problem an additional variable becomes significant, i.e. the jet thrust or momentum of the blowing air, $T_j = m_j v_j$. This new variable must be included in the general equation for a force, such as:

$$F \sim \rho^a \, l^b \, V_o^c \, T_j^d \, \mu^e \tag{2}$$

Substituting the dimensions of the variables on both sides of eq. (2) in terms of the three basic units of mass, length, and time, symbolized by M, L, and T, respectively, and equating gives:

$$\left[\frac{M\,L}{T^2}\right] = \left[\frac{M}{L^3}\right]^a \left[L\right]^b \left[\frac{L}{T}\right]^c \left[\frac{M\,L}{T^2}\right]^d \left[\frac{M}{L\,T}\right]^e \tag{3}$$

Equating the exponents of like units yields:

$$\begin{aligned} M:&\quad 1 = a + d + e \\ L:&\quad 1 = -3a + b + c + d - e \\ T:&\quad 2 = c + 2d + e \end{aligned} \tag{4}$$

The three most important variables in the problem are ρ, l, and V_o. Therefore, the exponents a, b, and c are expressed in terms of d and e by the simultaneous solution of eqs. (4), giving:

$$a = 1 - d - e$$

$$b = 2 - 2d - e$$

$$c = 2 - 2d - e$$

Substituting eqs. (5) into eq. (2) and separating known and unknown exponents produces the general force equation containing two nondimensional parameters, i.e.:

$$F \sim \rho\, l^2\, V_o^2 \left[\frac{T_j}{\rho\, V_o^2\, l^2}\right]^d \left[\frac{\rho\, V_o\, l}{\mu}\right]^{-e} \tag{6}$$

The second nondimensional group of variables in eq. (6) is recognized as the Reynolds number. The first is a parameter which is common to problems involving boundary layer control and edge blowing, known as the blowing momentum coefficient, C_μ. For convenience in this thesis the parameter, C_μ, is defined as:

$$C_\mu = \frac{T_j}{\frac{1}{2}\rho\, V_o^2\, S} = \frac{m_j\, v_j}{\frac{1}{2}\rho\, V_o^2\, S} \tag{7}$$

The Reynolds number is based upon the centerline chord of the model as the characteristic length and is therefore denoted as:

$$R_c = \frac{\rho\, V_o\, c_o}{\mu} \tag{8}$$

Substituting eqs. (7) and (8) into eq. (6) and introducing an arbitrary constant, A, on the right hand side yields the general fluid-force equation for a body with apex blowing:

$$F = A\, \rho\, V_o^2\, S\, (C_\mu)^d\, R_c^{-e} \tag{9}$$

APPENDIX B
WIND TUNNEL CORRECTIONS

B.1 Correction for Stiffness of Flexible Hoses:

Although flexible hoses were used to introduce the high pressure blowing air to the balance support system, there were still slight distortions in the balance system caused by the stiffness of the hoses. These distortions created forces and moments on the balance system and hence errors were induced in the measurements made on the models with apex blowing. To calculate appropriate corrections for these errors, measurements were made with a calibrator connected to the bottom of the support strut in place of the model. The calibrator consisted of a short pipe through which the blowing air was fed. The air then emerged radially between two circular end plates which formed an adjustable gap. Since the air emerged radially from the calibrator which was positioned at the virtual center of the balance, the only forces and moments measured with the calibrator in place were those due to the distortion of the balance by the flexible hoses. The balance readings at various values of orifice plate pressure difference were taken with the calibrator in a fixed position. The calibrator was then rotated 180° and the readings retaken to allow for inaccuracies in the manufacture. The mean of the two sets of readings was used to calculate the balance corrections for the stiffness of the flexible hoses. The calibrator gap was varied during the calibration in order to match the model static pressure-mass flow characteristic over the entire range of blowing coefficients to be used in the test program.

A typical set of corrections for $C_\mu = 0.08$ at a tunnel speed of 125 ft./sec. derived from such a calibration was:

	DDW	SGW	MGW	LGW
ΔC_L:	-0.0007	-0.0007	-0.0006	-0.0006
ΔC_D:	-0.0017	-0.0017	-0.0015	-0.0013
ΔC_M:	+0.0026	+0.0026	+0.0022	+0.0021

The calibration was carried out each time the flex-

ible hoses were removed and replaced on the balance support system because the corrections varied with the adjustment of the hoses.

B.2 Tare Correction for Strut:

Based on calibration tests on the support strut and nose wires performed by Hyde (Refs. 10 and 20) the following tare corrections were used at a tunnel speed of 125 ft./sec.:

	DDW	SGW	MGW	LGW
ΔC_L:	+0.0040	+0.0039	+0.0034	+0.0031
ΔC_D:	-0.0098	-0.0096	-0.0083	-0.0077
ΔC_M:	+0.0102	+0.0099	+0.0086	+0.0079

B.3 Wind Tunnel Lift Constraint Correction:

The conventional corrections for wind tunnel lift constraint as described in Ref. 27 were applied. These corrections were calculated to be:

	DDW	SGW	MGW	LGW
$\Delta\alpha$ (deg.):	$0.997C_{L_A}$	$1.018C_{L_A}$	$1.180C_{L_A}$	$1.270C_{L_A}$
ΔC_D:	$0.0174C_{L_A}^2$	$0.0177C_{L_A}^2$	$0.0206C_{L_A}^2$	$0.0222C_{L_A}^2$

B.4 Blockage Correction:

Although the increase in wind velocity in the working section caused by the presence of the model was less than 1% for all the model configurations tested, the corresponding increment in drag was found to be significant on the models with extensions at high incidences (i.e. the order of 3 - 4% of the measured drag on the MGW model at $\alpha=20^\circ$). The blockage correction was applied to the drag results of all the models for completeness. The drag correction due to blockage was found to be:

$$\Delta C_D = \mp \frac{2\epsilon}{1-2\epsilon}$$

where ϵ is a function of the model and wake blockage as described in Ref. 27.

B.5 Balance Cross Coupling Correction:

Corrections were made to allow for the small amount of cross coupling inherent in the balance system. The following corrections were calculated with regard to Ref. 28 and were applied to the balance measurements:

$$\Delta C_L = -0.0096\, C_{D\,meas.}$$

$$\Delta C_D = +0.0009\, C_{L\,meas.}$$

$$\Delta C_M = +0.0008\, C_{L\,meas.}$$

APPENDIX C
COLLAPSE OF THE LIFT DATA

C.1 Relationship between ΔC_L and C_μ :

By applying the square root of the slenderness ratio, $\sqrt{s/c_o}$, to the lift coefficients of the various models at different values of C_μ and plotting the results against $(\alpha - \alpha_o)$ the results of all the wings collapsed, as expected, onto four separate curves -- one for each value of C_μ tested. The correlation between the lift increment due to apex blowing, ΔC_L, and the value of C_μ was necessary in order to collapse these four curves into one. Consideration of the dimensional analysis in Appendix A indicated that this relationship possibly had the form:

$$\frac{\Delta C_L}{\sqrt{s/c_o}} = \frac{C_{L\mu}}{\sqrt{s/c_o}} - \frac{C_L}{\sqrt{s/c_o}} = \frac{C_{L\mu}}{\sqrt{s/c_o}} \left(A\, C_\mu^{\,B} \right) \qquad (1)$$

where, for convenience in this analysis only:

$C_{L\mu}$ is the value of the aerodynamic lift coefficient at a given value of C_μ.

C_L is the value of the aerodynamic lift coefficient at $C_\mu = 0$ (i.e. at $C_\mu = 0$, $C_{L\mu} = C_L$).

Dividing eq. (1) by $C_{L\mu}/\sqrt{s/c_o}$ and taking the logarithms of both sides of the resulting equation gives:

$$\log \left[\frac{\Delta C_L}{C_{L\mu}} \right] = \log A + B \log C_\mu \qquad (2)$$

Values for $\Delta C_L / C_{L\mu}$ in eq. (2) were calculated from the experimental results on the various wings. Plotting these values versus C_μ on a log-log plot resulted in a straight line, thus verifying the assumption concerning the form of the relationship given in eq. (1). The values of the constants were determined from the log-log plot to be:

$$A = 0.84$$
$$B = 0.621 \qquad (3)$$

Rearranging eq. (1) and substituting the values of the constants from eq. (3) gives:

$$\left[\frac{C_L}{\sqrt{s/c'_o}}\right] = \left[\frac{C_{L\mu}}{\sqrt{s/c'_o}}\right] (1 - 0.84 C_\mu^{0.621}) \qquad (4)$$

Equation (4) is the empirical relationship between the values of aerodynamic lift with apex blowing and without apex blowing for all the members of the family of wings tested.

C.2 Correlation of C_L and $(\alpha - \alpha_o)$:

After obtaining the empirical relationship given in eq. (4) above, it was applied to the data from all the wings at all the values of C_μ tested and the results were plotted against $(\alpha - \alpha_o)$ as shown in Fig. 5·12. The data appeared to collapse satisfactorily onto a single curve so it was of interest to discover the degree of correlation between the variables and, if the degree of correlation proved satisfactory, to find the regression formula for the relationship.

The statistical analysis which follows was conducted using methods described in Refs. 29 and 30. In order to carry out the analysis it was convenient to define:

$X = (\alpha - \alpha_o)$, the independent variable

$$Y = \left[\frac{C_{L\mu}}{\sqrt{s/c'_o}}\right] (1 - 0.84 C_\mu^{0.621}) \text{ , the dependent variable} \qquad (5)$$

Fig. 5·12 indicated that the relationship between the variables was linear. In order to test this, the Pearson-r linear correlation coefficient was computed from:

$$r = \frac{N\Sigma XY - (\Sigma X)(\Sigma Y)}{\sqrt{[N\Sigma X^2 - (\Sigma X)^2][N\Sigma Y^2 - (\Sigma Y)^2]}} \qquad (6)$$

where N = 139, in this case.
The value of r indicates the accuracy of the linear assumption. In general, the value of r varies between -1 and +1. A value of r = 0 would indicate no linear correlation between the variables while a value of r = ±1 indicates either perfect positive or perfect negative linear correlation, according to the sign. In this case

it was found that:

$$r = +0.998 \tag{6}$$

indicating a high positive linear correlation between X and Y as defined in eq. (5). Since the data used to calculate r covered a range:

$$2^{\circ} < (\alpha - \alpha_{o}) < 20^{\circ} \tag{7}$$

this linearity exists in this range and non-linearity outside this range is possible.

Knowing that the correlation between the variables, X and Y, is linear, the regression curve relating them is the "least-square" line through the X-Y data points. The normal equations for the "least-square" line of Y on X are:

$$\begin{aligned} \sum Y &= A_{1} N + B_{1} \sum X \\ \sum X Y &= A_{1} \sum X + B_{1} \sum X^{2} \end{aligned} \tag{8}$$

where A_{1} and B_{1} are the intercept and the slope of the "least-square" line, respectively.

A_{1} and B_{1} can be calculated using:

$$\begin{aligned} A_{1} &= \frac{(\sum Y)(\sum X^{2}) - (\sum X)(\sum XY)}{N \sum X^{2} - (\sum X)^{2}} \\ B_{1} &= \frac{N \sum XY - (\sum X)(\sum Y)}{N \sum X^{2} - (\sum X)^{2}} \end{aligned} \tag{9}$$

The constants A_{1} and B_{1} were thus determined and the "least-square" regression line was found to be represented by:

$$Y = -0.045 + 0.0578\ X \tag{10}$$

If the total variation is defined as:

$$\sum (Y - \bar{Y})^{2} \tag{11}$$

where $\bar{Y}$ is the mean of all the Y values, then the total variation can be written:

$$\sum (Y - \bar{Y})^{2} = \sum (Y - Y_{est.})^{2} + \sum (Y_{est.} - \bar{Y})^{2} \tag{12}$$

where $Y_{est.}$ is the estimated value of Y from the regression line formula.

The first term on the right hand side of eq. (12) is

called the "explained" variation, which is due to the normal distribution of the samples. The second term is called the "unexplained" variation, which is random and could be caused by a variable in the problem which has not been taken into account in the correlation analysis. In this problem, analysis showed that the "explained" variation accounted for 99.6% of the total variation while only 0.4% of the total variation was "unexplained".

The 95% confidence limits define the region within which at least 95% of the data from the total "population" should lie. These limits can be calculated from:

$$Y = Y_o \pm \frac{t_{.975}}{\sqrt{N-2}} s_{Y\cdot X} \sqrt{N+1+\frac{(X_o-\bar{X})^2}{\sigma_x^2}} \qquad (13)$$

where Y_o = the value of Y predicted from the regression equation (i.e. eq. 10) at a given value of $X = X_o$.

$t_{.975} = 1.97$

$s_{Y\cdot X} = 0.019$

$\sigma_x = 5.29$

Substituting these values into eq. (13) yields:

$$Y = Y_o \pm 0.038 \qquad (14)$$

Thus the 95% confidence region is defined by two lines parallel to the "least-square" regression line as shown in Fig. 5·12. Analysis showed that 96.5% of the data sample falls into the 95% confidence region in this case.

APPENDIX D
THE LANDING AND TAKE-OFF PERFORMANCE OF AN ALL-WING AIRBUS

D.1 General:

The models tested in the wind tunnel were based on the concept of an all-wing airbus of the future which would incorporate apex blowing. Such an aircraft would be utilized primarily over relatively short ranges and the capability of operating from small airfields would greatly enhance its usefulness. For this reason preliminary calculations were made to estimate the potential landing and take-off performance improvement afforded by the use of apex blowing on such an aircraft.

The following basic assumptions were made for this analysis:

total thrust (4 engines): 60,000 lbs.
take-off weight: 180,000 lbs.
landing weight: 150,000 lbs.
wing area: 5,000 sq. ft.
engines mounted in the nose and total efflux exhausted through blowing nozzles to produce apex blowing, $\Phi = 25^{\circ}$; total efflux exhausted aft without blowing, $\Phi = 0^{\circ}$.
BW wind tunnel data used (Ref. 10)

D.2 Landing Performance:

Without blowing the airbus approach speed is limited by vortex breakdown just as a conventional aircraft is limited by the stall. Hence the approach speed without blowing was taken as 1.3 x "vortex breakdown speed" or 142 kts. The airbus with apex blowing is not affected by vortex breakdown, therefore the approach speed has to be based on another criterion. Pinsker (Ref. 31) has suggested the "zero rate of climb speed" where the drag equals the available thrust as such a criterion for stall-free aircraft. This concept was used in this analysis to define the approach speed of the airbus with apex blowing. By taking 1.2 x "zero rate of climb speed" as proposed in Ref. 31 the approach speed with apex blowing was determined to be 110 kts. -- 32 kts. less than the unblown case.

The total landing distance required from an altitude of 50 ft. was found to be 2,190 ft. for the aircraft with apex blowing, $C_\mu = 0.15$, and 3,050 ft. without blowing. These landing distances are based on simple calculations but they do serve to indicate that a large improvement in the landing performance -- 28% reduction in the required distance -- is possible with apex blowing. This improvement is primarily due to the reduction in the approach speed with apex blowing because of the elimination of vortex breakdown.

D.3 Take-off Performance:

The take-off performance was not found to be altered by the use of apex blowing for the configurations analized. The reduction in the safe take-off speed due to apex blowing is of the order of 10 kts. but since there is reduced thrust available for acceleration in the blown case ($\phi = 25^\circ$) the take-off distances are approximately the same.

The take-off analysis pointed out that an aircraft with the assumed characteristics would require at least three, and in all probability, four engines for safe operation in the event of an engine failure during the take-off maneuver.